JOHANNES GUTENBERG UNIVERSITÄT MAINZ

MAX PLANCK INSTITUTE FOR POLYMER RESEARCH

Synthesis, topology, and photoexcited dynamics of amino acid-derived gold nanoparticles

DISSERTATION

zur Erlangung des Grades
„Doktor rerum naturalium“
am Fachbereich Chemie, Pharmazie und Geowissenschaften
der Johannes Gutenberg-Universität und in Kooperation mit dem
Max-Planck-Institut für Polymerforschung in Mainz

Ricardo Baez

geboren in Bogota-Kolumbien

November, 2021

SYNTHESIS, TOPOLOGY, AND PHOTOEXCITED DYNAMICS OF AMINO ACID-DERIVED GOLD NANOPARTICLES

Tag der mündlichen Prüfung: February 3, 2022 ,

As a result of this research, the author declares that the dissertation was submitted without unauthorized external assistance and used only sources acknowledged in work. In carrying out this research, the rules of standard scientific practice formulated in Johannes Gutenberg-University Mainz's statutes to ensure standard scientific practice have complied. All textual passages, which are appropriated verbatim or paraphrased from published and unpublished texts and all information obtained from oral sources, are duly indicated and listed following bibliographical rules.

Contents

List of Figures

ABSTRACT

The use of biomolecules as capping and reducing agents in the synthesis of metallic nanoparticles constitutes a promising framework to achieve desired functional properties with minimal toxicity. The system's complexity and the large number of variables involved represent a challenge for theoretical and experimental investigations to devise precise synthesis protocols. In the center of this dissertation, we use L-asparagine (Asn), an amino acid building block of large biomolecular systems, to synthesize gold nanoparticles (AuNPs) in an aqueous solution at controlled pH. The use of Asn offers a primary system that allows us to understand the role of biomolecules in synthesizing metallic nanoparticles. Our results indicate that AuNPs synthesized in acidic (pH 6) and basic (pH 9) environments present somewhat different morphologies. We examine these AuNPs via Raman scattering experiments and classical molecular dynamics simulations of zwitterionic and anionic Asn states adsorbing on (111)-, (100)-, (110)-, and (311)-oriented gold surfaces. A combined analysis infers that the underlying mechanism controlling AuNPs geometry correlates with amine's preferential adsorption over ammonium groups, enhanced upon increasing pH. Water molecules strongly interact with the gold face-centered-cubic lattice and create traps that prevent the Asn from diffusing on the more open surfaces. Our simulations expose that Asn (both zwitterionic and anionic) adsorption on gold (111) is essentially different from adsorption on more open surfaces. These results indicate that pH is a relevant parameter in green-synthesis protocols that can control the nanoparticle's geometry and pave the way to computational studies exploring the effect of water monolayers on the adsorption of small molecules on wet gold surfaces. Additionally, The use of amino acids as capping and reducing agents in the synthesis of metallic nanoparticles constitutes a promising framework to achieve desired functional

properties with minimal toxicity. In the second part of this dissertation, we use L-Asparagine (Asn) to synthesize gold nanoparticles (AuNPs) in an aqueous solution at controlled pH. Our results indicate that size, shape, and localized surface plasmon resonance (LSPR) characteristics strongly depend on the Asn pH values of pH 6 and 8. The particle size obtained for pH 6 is 18±9 nm, while the particle size for pH 8 is 86±25 nm. The electron cooling dynamics of the LSPR were examined by transient absorption spectroscopy (fs-TA), and the results show that the pH 8 sample exhibits slightly slower electron cooling. We discuss these results in the context of our earlier findings regarding the pH-dependent amino acid-binding at the Au surface. The LSPR stability and the high reproducibility of the AuNPs-Asn complex suggest that AuNPs synthesized can be a potential candidate for biocompatible applications with plasmonic structures, such as bioimaging.

Chapter 1

Introduction

Nanoscale noble metals, especially gold nanoparticles (AuNPs), have been extensively studied over the past few decades. Faraday, in 1857, studied the agents used to reduce gold to attain AuNPs and their optical properties [10]. Since then, AuNPs and other metal nanoparticles have been investigated in detail for their excellent optical properties [11]. An outstanding example is the attractive and mysterious Lycurgus cup. In the 4th-century, the cup was designed using gold and silver powders [12]. The cup emits different colors depending on the side and angle of illumination [13]. It appeared red when lit from behind and green when lit from in front (Figure1.1). This mystery could only be understood in 1991 with the use of atomic force microscopy [13, 14]. The dichroism effect was due to the presence of silver and gold nanoparticles dispersed in the glass matrix. The green color was attributed to light scattered by the silver NPs ((66.2%)) of size $> 40nm$, and the red color was due to gold (31.2%) and copper (2.6%) NPs [13, 15].

Figure 1.1: The Lycurgus cup cage cup was made during the Roman Empire in the 4th-century CE by the dichroic glass. The glass appears green when illuminated from the outside (left side) and purple-red when illuminated from the inside (right side). Figure extracted from https://en.wikipedia.org/wiki/Lycurgus_Cup

The optical properties of AuNPs depends strongly on their size and morphological properties [16]. Varying these parameters has paved the way for their applications in diverse areas [17]. Gold nanoparticles have found applications in surface enhanced Raman spectroscopy [18, 19], biological labeling [20], and catalysis [21–23].

Properties of gold bulk substances with particle sizes bigger than micrometer size have been studied for years by solid-state physicists and material scientists [24]. Additionally, clusters of gold materials relative to just a few atoms of size in the sub-nanometric scale have been studied for the past decades as they possess extraordinary

properties relative to their bulk equivalents [25]. These "nanomaterials" are defined as "a collection of atoms that forms a defined structure with dimensions between 1-100 nm (see Figure1.2) [26]. This thesis focuses on AuNPs which have gained a unique position due to their extraordinary optical properties and very high chemical stability as compared to other materials such as silver or magnesium [27–30].

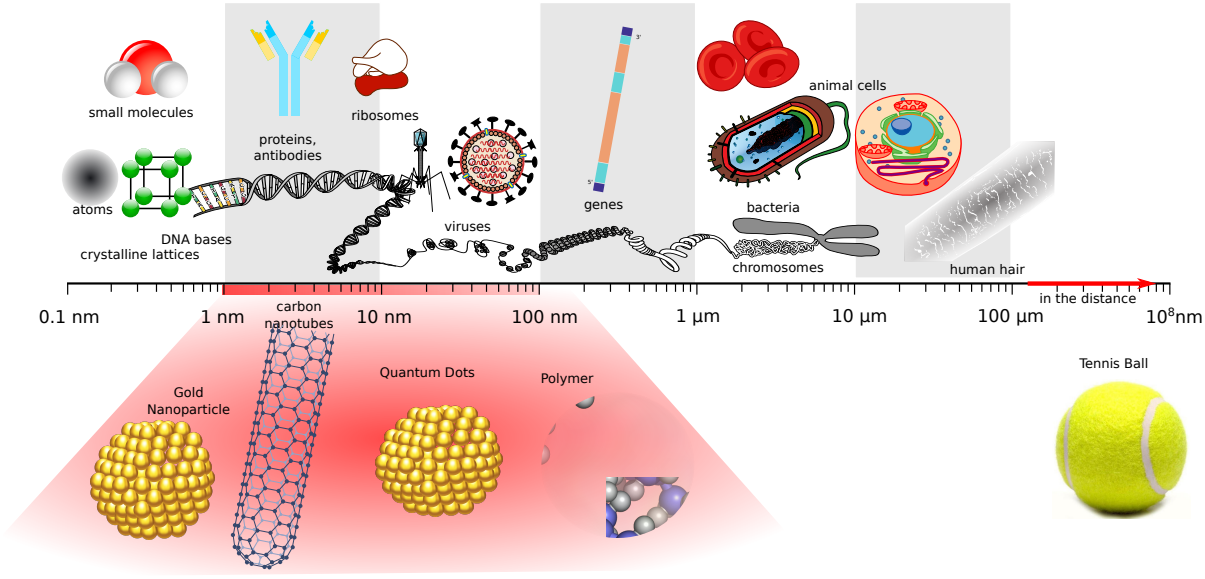

Figure 1.2: schematic representation of nanometer scale in comparison with other objects. svg Wikipedia diagram, modification–nanotechnology https://commons.wikimedia.org/wiki/File:Biological_and_technological_scales_compared-en.svg

In colloidal metal NPs dispersed in solvent, the color of the liquid is influenced by the particle shape and size [31, 32]. Figure 1.3 shows a clear example of this relationship: a change in the shape or size of the particles gives rise to a change in the color of the colloidal solution. [1].

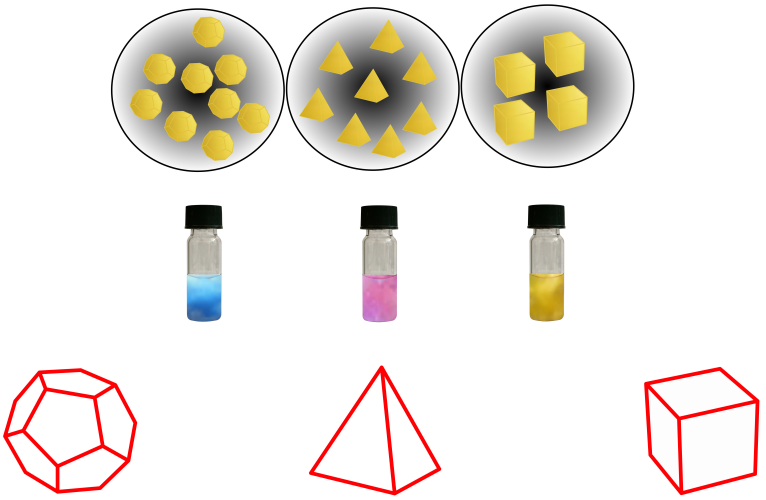

Figure 1.3: Example of shape variation in a collection of colloidal AuNPs as a function of color. The lower part shows the topological condition. Figure inspired by *Edgar González et. al.-2011* [1] and [2]

The question arises: where does the color of a colloidal solution of AuNPs come from? The answer lies in the *plasmonic effect*. When the AuNPs interact with external photons, which can be considered an external electromagnetic field, the electrons of the AuNPs localized in the d-orbitals undergo an interesting effect [33]. They all oscillate coherently according to the electromagnetic field oscillation, which is known as the plasmonic effect. Figure1.4 shows a schematic description of the electron oscillation (plasmonic effect) as a AuNP interacts with an external electromagnetic field.

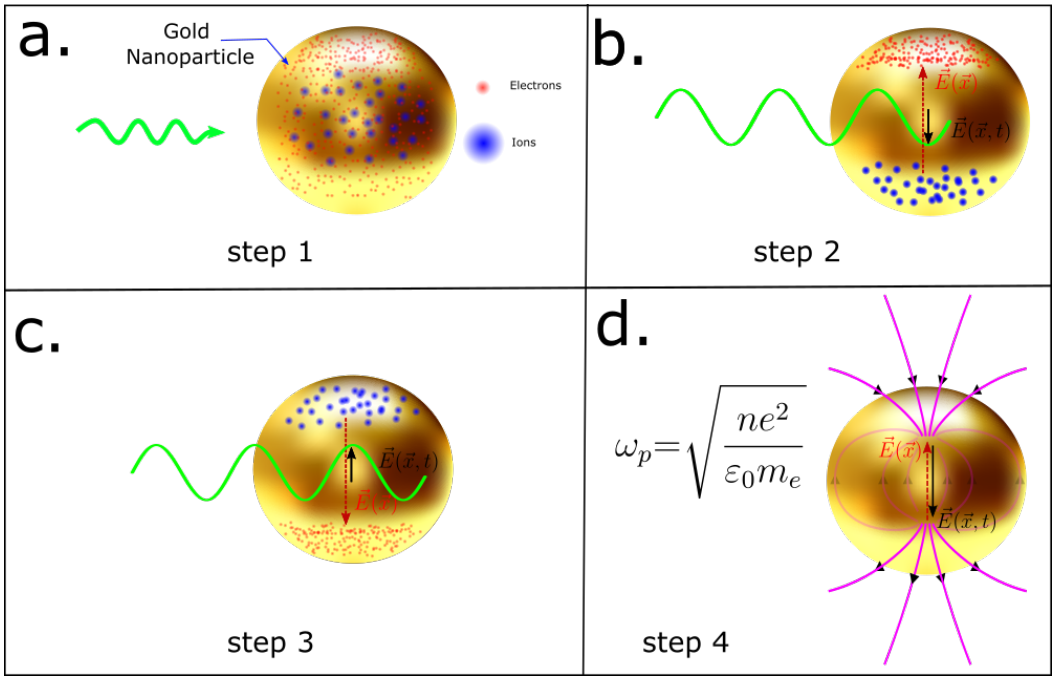

Figure 1.4: Schematic describing the LSPR concept in AuNPs. **a.)** In step 1, the electrons are in the steady-state before interacting with an external electromagnetic field $\vec{E}(\vec{x},t)$. **b.)** In step 2, the first interaction of the electromagnetic field with the AuNP appears. A polarization effect creates in AuNP where electrons on the d-orbitals move opposite to the incited electric field, and the ions move along with the direction of the electric field.**c.)** In step 3, the electrons moved in the opposite direction of step 2, and a stationary electric field $\vec{E}(\vec{x})$ appeared in the particle. **d.)** In step 4, during the interaction between the external field $\vec{E}(\vec{x},t) \sim \hbar\omega$ and the stationary internal field $\vec{E}(\vec{x})$, the LSPR effect adopts a dipole distribution with a frequency ω_p (purple lines).

In addition to colloidal AuNPs, plasmonic effects are also observed in Au thin films and even in bulk Au. In bulk Au (r > 100 nm), interaction with an electromagnetic field leads to stationary oscillation modes in the Au. In Au thin films, the plasmon effect emerges as a propagating oscillation at the interface between metal and dielectric material. [11]. Figure1.5 illustrates the different cases of plasmonic effects depending on the material size.

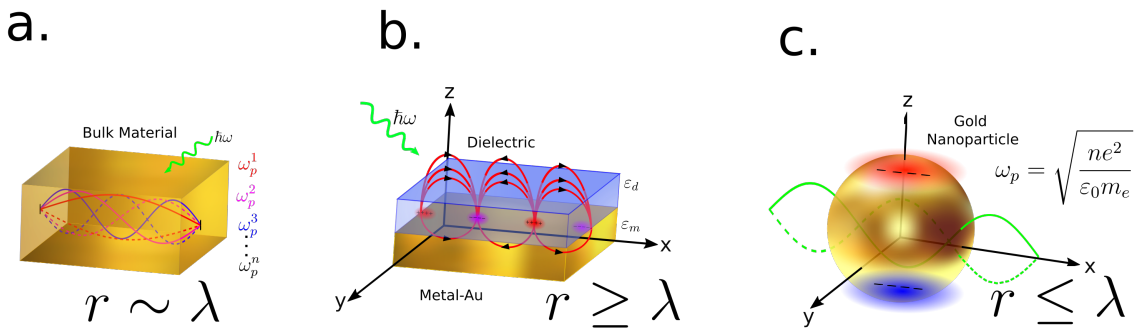

Figure 1.5: Schematic representation of the plasmon effect in bulk Au (r > 100 nm), Au thin film, and AuNPs. **a**. Bulk plasmons emerge when the wavelength of radiation is similar to the size of the material ($r\ \lambda$); in this case, excitation leads to stationary oscillations with different modes ω_p^i. **b**. In thin films, the plasmonic effect emerges as a propagating oscillation at the interface between metal and dielectric material ($r \geq \lambda$). **c**. In AuNPs, the plasmon describes a resonance process between electrons localized in the d-orbitals and the frequency of the external radiation.($r \leq \lambda$)

For the plasmon effect in colloidal gold nanoparticles, the resonance process described by the electrons is named Localized Surface Plasmon Resonance (LSPR) [34]. Using Maxwell's equations, it is possible to find the LSPR field distribution around and inside an AuNP when the particle interacts with an external electromagnetic field $\vec{E}(\vec{x}, t)$, which creates a polarization effect in AuNPs where electrons move opposite to the direction of the incident electric field. The ions move along with the direction of the electric field, which means

$$\mathbf{E}_1 = E_0 \frac{3\varepsilon_2}{\varepsilon_1 + 2\varepsilon_2} \left(cos(\theta)\mathbf{n}_r - sin(\theta)\mathbf{n}_\theta\right) = E_0 \frac{3\varepsilon_2}{\varepsilon_1 + 2\varepsilon_2}\mathbf{n}_x \tag{1.1}$$

$$\mathbf{E}_2 = E_0 \left(cos(\theta)\mathbf{n}_r - sin(\theta)\mathbf{n}_\theta\right) + \frac{\varepsilon_1 - \varepsilon_2}{\varepsilon_1 + 2\varepsilon_2}\frac{a^3}{r^3} E_0 \left(cos(\theta)\mathbf{n}_r + sin(\theta)\mathbf{n}_\theta\right) \tag{1.2}$$

Equation 1.1 describes the LSPR field distribution inside the particles. It is possible to observe (E_1) since it is a constant field and only depends on the dielectric function

of the AuNP. ϵ_1 and ϵ_2 are the real and imaginary parts of this dielectric function, respectively. $\mathbf{n}_x$ is the direction of the field. However, the field outside of the AuNP (Equation 1.2) shows a different distribution. It consists of a superposition of the applied field and a dipole located at the AuNP center. It is possible to rewrite equation1.2 using the dipole moment $\mathbf{p}$:

$$\mathbf{E}_2 = \mathbf{E}_0 + \frac{3\mathbf{n}(\mathbf{n}\cdot\mathbf{p}) - \mathbf{p}}{4\pi\varepsilon_0\varepsilon_m}\frac{1}{r^3} \tag{1.3}$$

.

where the dipole moment $\mathbf{p}$ is defined as

$$\mathbf{p} = 4\pi\varepsilon_0\varepsilon_m a^3 \frac{\varepsilon - \varepsilon_m}{\varepsilon + 2\varepsilon_m}\mathbf{E}_0 \tag{1.4}$$

Equations 1.3 and 1.4 shows that the external field induces a dipole moment inside the AuNP with a magnitude proportional to $|\mathbf{E}_0|$. A graphical description of the LSPR field distribution inside and outside of AuNP is shown in figure 1.6.

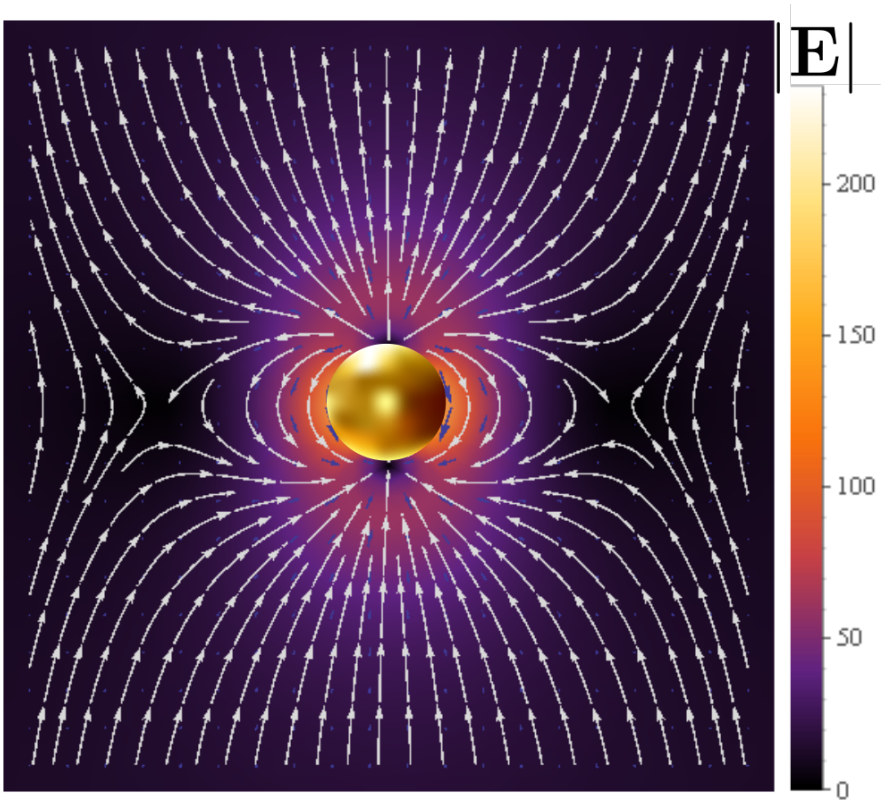

Figure 1.6: Graphic of the dipole distribution acquired by the LSPR field outside and inside of AuNP. Equations1.1 and 1.2 were used to plot the field distribution, and the *Wolfram Mathematica* interface was used to plot the results.

In terms of AuNPs' optical properties, the polarizability α is another crucial variable in the plasmonic effect, which is defined as

$$\mathbf{p} = \varepsilon_0 \varepsilon_m \alpha \mathbf{E}_0 \tag{1.5}$$

,

and as a consequence α is equal to

$$\alpha = 4\pi a^3 \frac{\varepsilon - \varepsilon_m}{\varepsilon + 2\varepsilon_m} \tag{1.6}$$

This result shows that the LSPR distribution depends on both the dielectric properties of the AuNP as well as the dielectric parameters of the medium surrounding the AuNP. These variables must be considered when developing gold nanoparticle synthetic procedures, as the final environment (solvent, ligands) will impact the optical properties of the resulting AuNPs.

The chemical synthesis of AuNPs combines a gold source, typically $HAuCl_4 \cdot 3H_2O$ (Tetrachloroauric(III)-acid trihydrate 99%), a reducing agent, and a stabilizing agent. There are many possible ways to vary and tune the synthetic procedure in order to achieve, for example, particular particle size or shape.

This thesis describes the synthesis and characterization of colloidal AuNPs derived by a novel route, based on utilizing the amino acid Asparagine as both a reducing and stabilizing agent. This approach offers the possibility to simplify AuNP synthesis by using a single reducing and stabilizing agent as well as to create nanoparticles with biologically friendly ligands [35]. Computational, spectroscopic, and structural characterization methods are used to show how the synthetic conditions influence the resulting shape and LSPR effects in the AuNPs.

This document is organized as follows: Chapter 2 discusses the materials used to carry out the synthesis and describes the method established to synthesize the particles. Chapter 3 describes the characterization techniques used to study the shape of particles obtained, the optical properties in the steady-state, and the LSPR dynamics, along with the interaction between the amino acid Asparagine and the AuNPs. Chapter 4 explains the simulation techniques used to study the influence of the Asparagine (Asn) over the AuNPs shape. Chapter 5, shows the synthesis of

Asn-AuNPs at varying pH. Raman spectroscopy and molecular dynamics simulations are used to reveal the origin of pH dependent AuNP geometry. Finally, in Chapter 6, we characterize the photophysical dynamics of the Asn-AuNPs using transient absorption spectroscopy.

Chapter 2

Materials and Methods used to synthesize gold nanoparticles

2.1 Synthesis of gold nanoparticles

The synthesis of AuNPs has been carried out through both top-down and bottom-up approaches to create diverse species in terms of shape, size, and embendding [36].The top down-approach reduces a bulk material to a nanometer scale using physical and chemical processses, while the bottom-up approach utilizes precursors such as metallic salts, which nucleate and grow to form nanostructures [37].

Chemical routes are the most commonly adopted route to synthesize colloid gold nanoparticles. The reducing agents initiate the nucleation process for the growth of nanoparticles by reducing the gold precursor to gold zero (Au^0). In some cases, a heat treatment is added to those routes. Four variables are essential to synthesize colloid gold nanoparticles: the material of particles, in this case, gold, the particle size, the embedding, and the particle shape. Figure 2.1 shows a schematic representation of those variables.

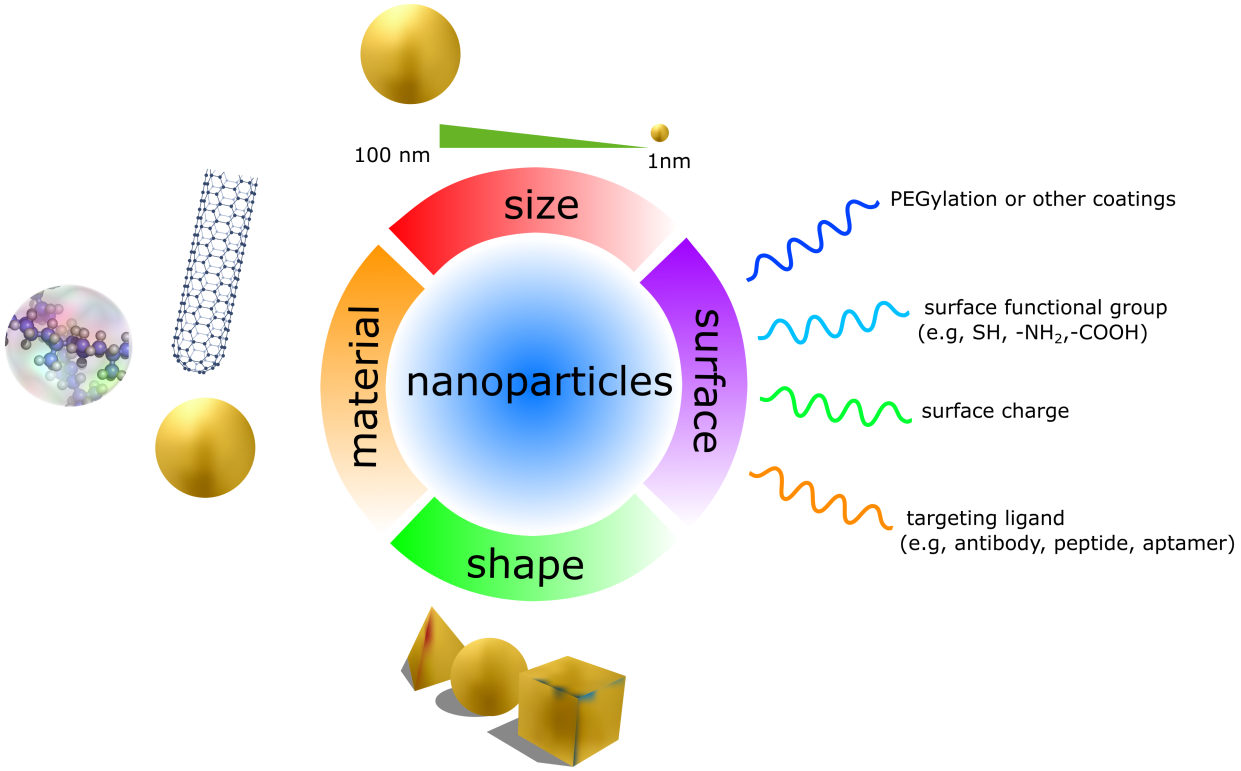

Figure 2.1: Schematic representation of four variables that control the synthesis of colloidal gold nanoparticles. In this thesis, the selected material was gold. Graphic inspired by the lecture - clinical trials, drug delivery, DNA nanostructures by Prof. Dr. D Lipomi. https://www.youtube.com/watch?v=79jL7dIJG7Q&ab_channel=DarrenLipomi

2.2 Synthesis of gold nanoparticles in solution by heat treatment

As mentioned before, the synthesis of AuNPs is based on the reduction of gold salt to gold zero (Au^0). The Turkevich method is one of the most widely used procedures for this approach [38].

In this method, the gold(III) chloride trihydrate ($HAuCl_4 \cdot 3H_2O$) solution is brought to a boil, and the trisodium citrate dihydrate ($Na_3C_6H5O_7$) is then added

while the mixture is vigorously stirred. After a few minutes the solution turns from yellow to red in color. This red color indicates the successful formation of AuNPs [39].

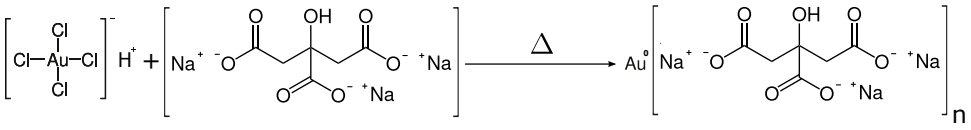

The synthesis of colloidal gold nanoparticles undergoes three steps;

(1) **reduction**, using a reducing agent like borohydrides, aminoboranes, formaldehyde, hydrazine, hydroxylamine, polyols, citric and oxalic acids, sugars, hydrogen peroxide, carbon monoxide, sulfites, hydrogen or acetylene.

(2) **stabilization**, using a specific agents like trisodium citrate dihydrate, sulfur ligands, phosphorus ligands, oxygen-based ligands, nitrogen-based ligands, dendrimers, polymers or surfactants for instance cetyltrimethylammonium bromide (CTAB).

(3) **aggregation control**, a stabilizing agent is added to the solution. Figure 2.2 shows a schematic representation of a typical gold reduction process, $Au^3 \rightarrow Au^0$.

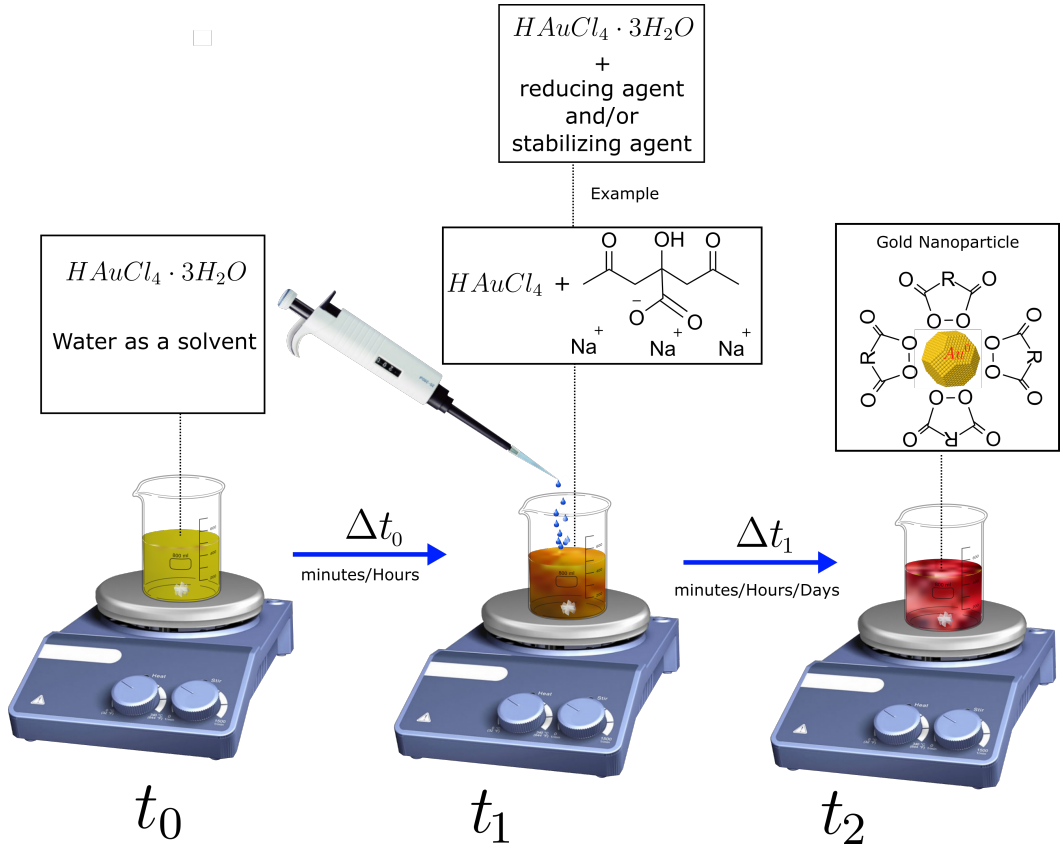

Figure 2.2: shows a schematic representation of colloid gold nanoparticles' typical synthesis. The schematic is based on the Turkevich method. [3]

This thesis builds upon the same basic scheme. We synthesized colloidal AuNPs using gold(III) chloride trihydrate as a precursor and we employed the amino acid Asparagine (Asn) as both reducing and stabilizing agent.

2.3 Can amino acids be used to synthesize gold nanoparticles?

Amino acids are present in all of human activity. They are part of the basic structure of the DNA. If these elements are so crucial, the fundamental question is, what are amino acids? The amino acids are organic compounds that are constituted by the

union of a unit of an amine functional group and a unit of a carboxyl functional group, as shown in the figure2.3.

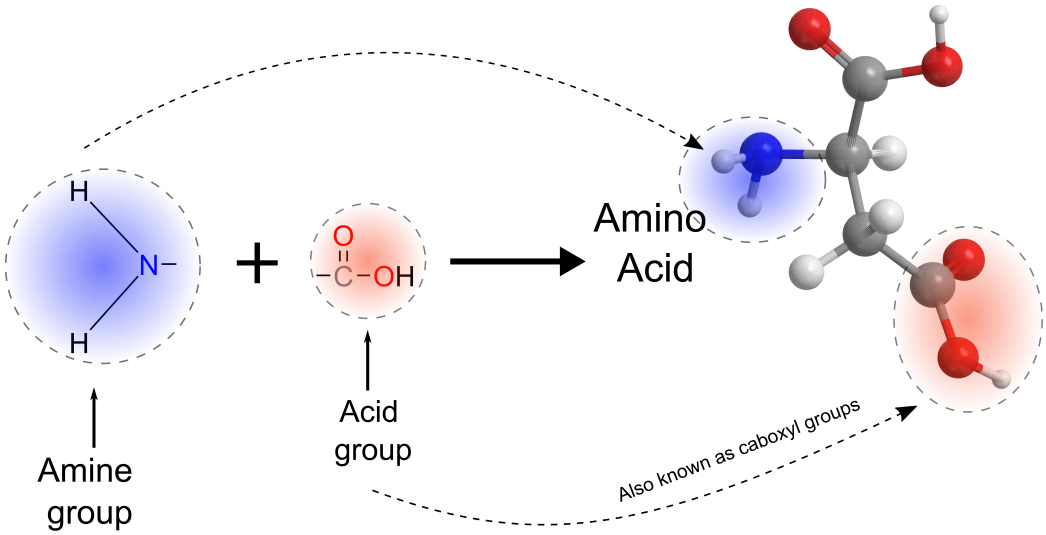

Figure 2.3: The fundamental components amino acids, shown here for Asaparagine

Figure 2.4 shows the 20 naturally occurring amino acids which make up proteins (in eurkaryotes), grouped according to their side chains and with their associated pKa values.

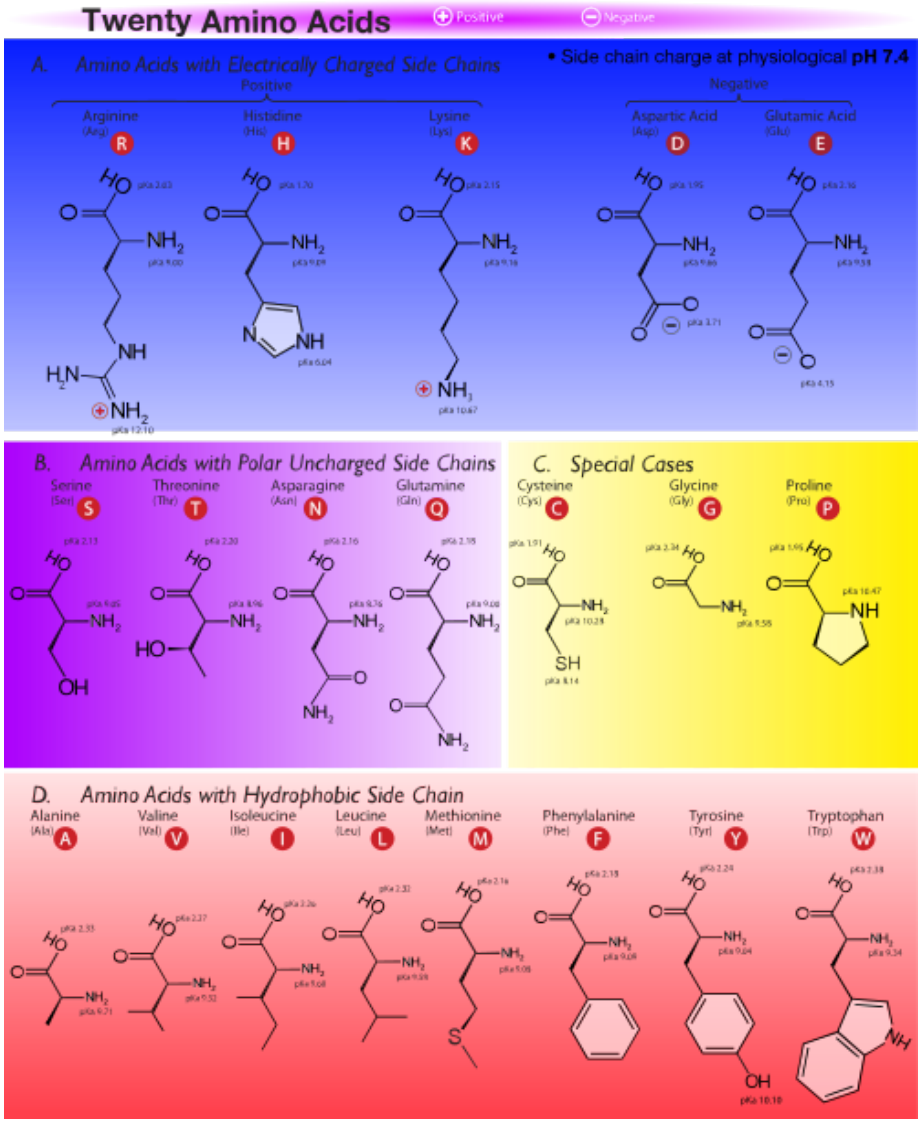

Figure 2.4: Schematic representation regarding to standard 20 amino acids. A. Amino acids with electrically charged side chains. B. Amino acids with polar uncharged side chains. C. Special case . and D. Amino acids with hydrophobic side chain.Image modified from https://commons.wikimedia.org/wiki/File:Amino_Acids.svg

Amino acids have been used to synthesize gold nanoparticles, acting as both reducing and capping agents [40, 41]. These results indicate that the type of amino acid and experimental conditions determine the AuNPs quality. For example, changes

in histidine concentration and pH facilitate adequate control of the size and particle shape [40]. By contrast, synthesis with L-Asparagine (Asn) produces monodisperse AuNPs, and Asn concentration variation does not induce changes in the AuNPs' color, size, or shape [42]. Alternatively, the pH of the amino acid solution is essential to control the reducing capabilities of the AuNPs [43, 44]. This fact prompts the question as to whether pH can be used as an adjustable parameter to control AuNPs geometry. We explored this question and find that the pH can be used to tune AuNP geometry due to the change in binding functionality of the amino acid (Chapter 5).

Chapter 3

Characterisation techniques

3.1 Transmission electron microscopy/morphological properties of AuNPs

Transmission Electron Microscopy (TEM) is an experimental technique commonly used in physics, chemistry, and material science. TEM allows magnified images of samples at or below atomic resolution. This is achieved by hitting the sample with a beam of electrons, applying the wave-particle duality of electrons base on de Broglie's relation [45].

$$\lambda = \frac{h}{p}. \tag{3.1}$$

It indicates that when the beams are used to impact the sample, the electrons acquire momentum p. λ represents wavelength, and h is Plack's constant [46]. TEM characterization yields sample information related to size, distribution, morphology, and crystal structure [47]. Figure 3.1 shows a typical result of a micrograph image of colloidal gold nanoparticles obtained by a TEM. These results belong to a batch of colloidal gold nanoparticles synthesized in current research.

Figure 3.1 shows the same sample imaged with four different size resolutions. Figures 3.1a and b yield information about the average size and distribution of the particles. The average size is obtained using a count of approximately 600 particles over a minimum of of two separate TEM micrographs (see Chapter 5). Figure 3.1c shows a 10 nm resolution, which allows us to calculate the size of the particle as well as the angles between the particle edges. Figure 3.1d is a high-resolution TEM (HR-TEM), which can be used to resolve the crystallographic plane orientation of the particle.

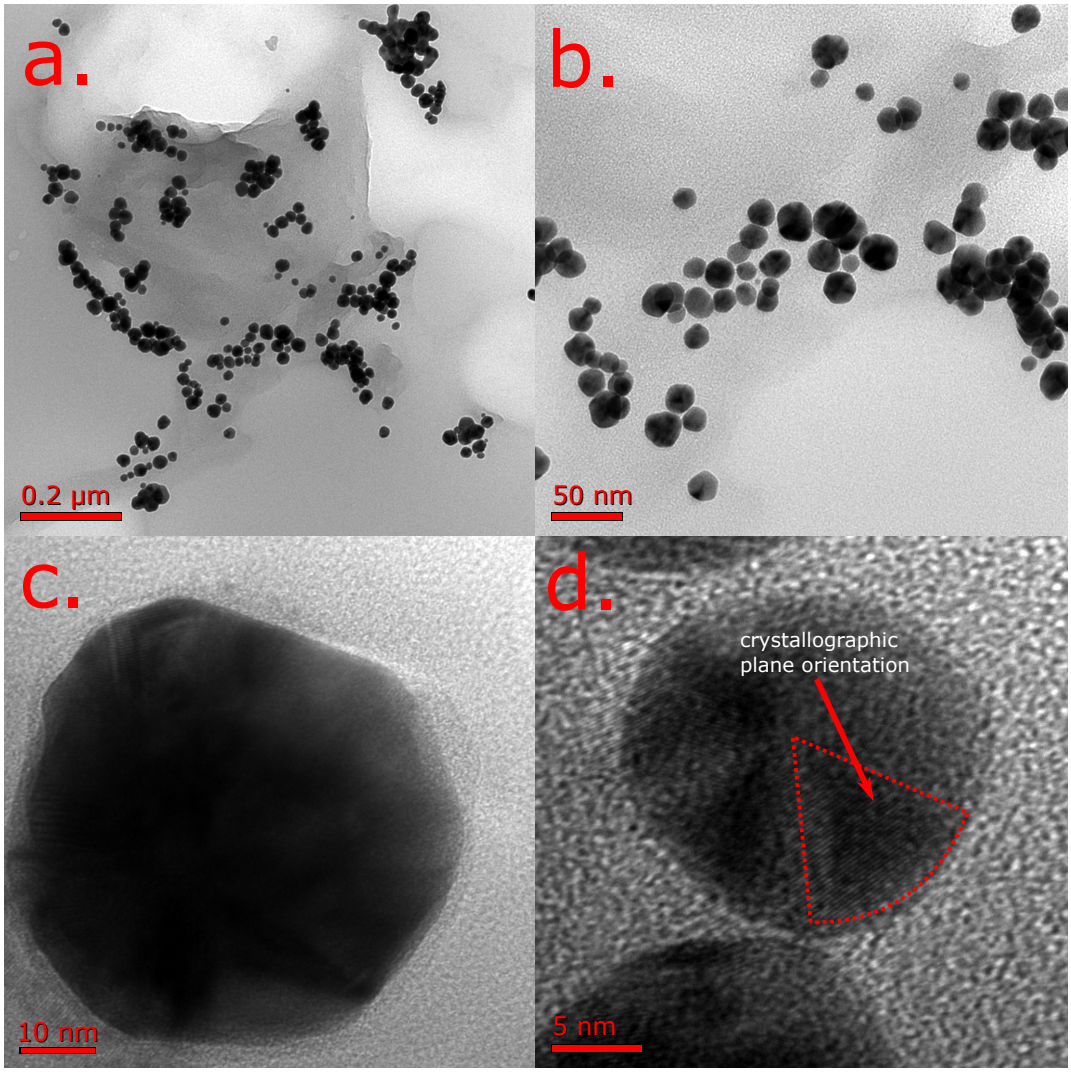

Figure 3.1: Typical result of a micrograph image of colloidal gold nanoparticles obtained by a TEM

3.2 UV-Vis Absorption Spectroscopy and Transient Absorption Spectroscopy (TA)/ Optical properties of nanoparticles

3.2.1 UV-Vis absorption spectroscopy

Ultraviolet and visible (UV/Vis) absorption spectroscopy measures the attenuation of electromagnetic radiation by an absorbing substance [1] [48], where the photon impacts the target sample with energy defined as $h\nu$ [49]. The energy of a molecule is given by a sum of the translational, rotational, vibrational, and electronic energies. In the UV-VIS spectral region, the energy levels correspond to electron density distributions (orbitals). [49]. In this UV-Vis range, the photon-matter interaction cause a change in polarization in the electron density of the sample, and this interaction is based on the Bohr-Einstein relationship,

$$\triangle(E) = E_2 - E_1 = h\nu \tag{3.2}$$

This relationship links the discrete energy states E_j with the electromagnetic radiation frequency ν. The relationship between the absorption at particular energies can be depicted in various units. Table 3.1 shows the value at 550nm, which is the reported position of the plasmonic absorption band for a 20 nm AuNP [50].

[1] Spectrometry refers to making quantitative measurements and spectroscopy is used when recording spectra over a range of wavelengths. In practice, the two terms are used interchangeably.

Table 3.1: Energy, frequency and wavelength units for the position of the plasmonic absorption band for a 20 nm AuNP [50]

		units	**value at 550nm**
wavelength	λ	nm	550
frequency	$\nu = c/\lambda$	Hz	$5.45X10^{14}$
photon energy	$E_i = h\nu$	J	$3.61X10^{-19}$
wave number	$k = \lambda^{-1}$	cm^{-1}	18181
electron energy	$U = h\nu/e$	eV	2.25

Figure 3.2 shows an example of the UV-vis absorption spectrum of 18 nm diameter AuNPs dispersed in water, from which a few important features can be distinguished. First, the fingerprint of Rayleigh scattering, composed of a region of high scattering at a low wavelength and a region of low scattering at a high wavelength. Also, it is possible to recognize a high absorption peak around 520nm, which corresponds to the Localized Surface Plasmon Resonance (LSPR). The LSPR exclusively occurs in colloidal metal nanoparticles. The absorption is in the region of 520 nm (green region). This is the reason for the red color of these gold nanoparticles, as Figure 3.2 shows.

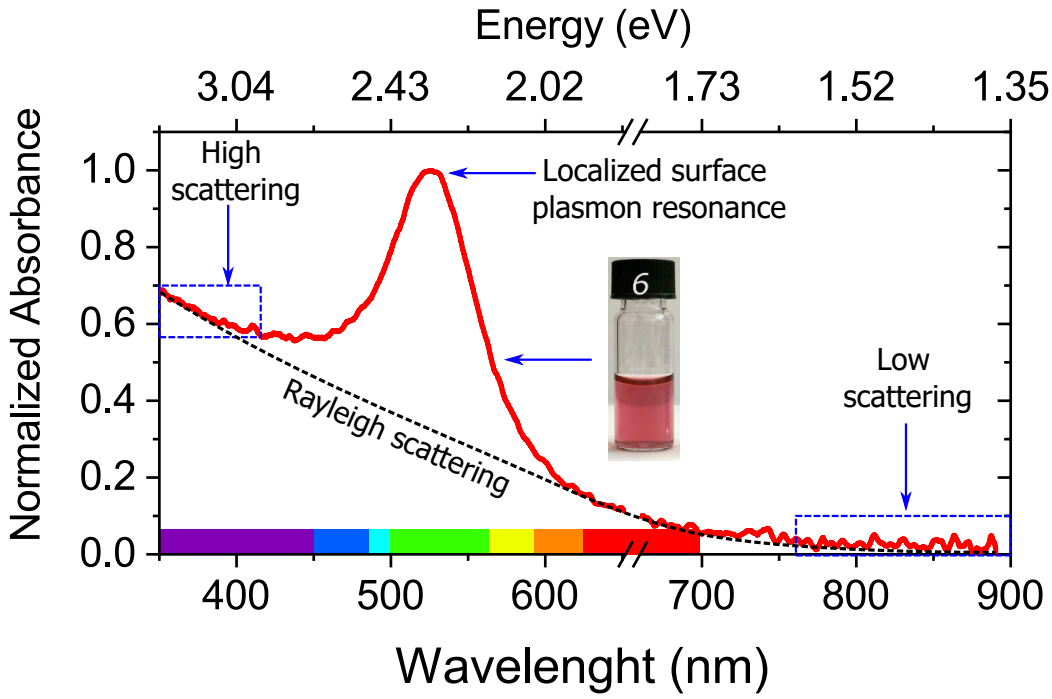

Figure 3.2: UV-Vis Absorption spectrum of colloid gold nanoparticles dissolved in water with a size of about 18nm.

Additionally, by the absorption spectrum it is possible to extract information about the chemical media around the particles, the particle size, and the particle shape. Those variables influence the AuNP absorption spectrum profile. Figure 3.3 shows three examples. In the first case, Figure 3.3a shows the same colloidal gold nanoparticles sample in five different media with different refractive indexes (ε). The extinction cross section C_{ext}, which is related to the absorption by

$$C_{ext} = C_{Abs} + C_{sct} \tag{3.3}$$

,

where C_{sct} is the scattering cross section, shows a redshift as the value of refractive indexes ε changes. This indicates that chemical media around the particles influences

the LSPR [4]. The inset graphic in Figure 3.3a tracks the change in C_{ext} as the value of the refractive index changes.

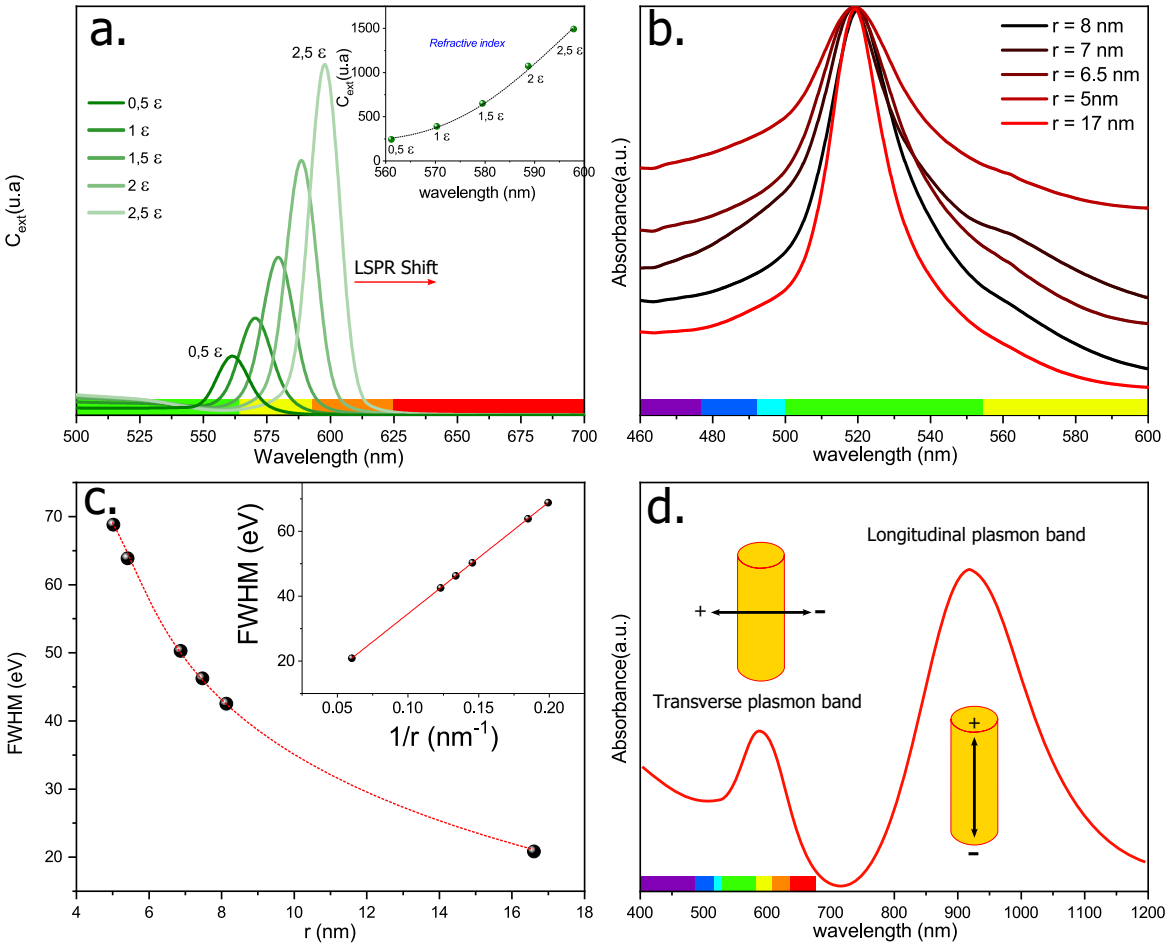

Figure 3.3: Schematic representation of (a.) LSPR shift of colloidal gold nanoparticles in different refractive indexes ε. (b.) Change in the Full Width at Half Maximum (FWHM) of the absorption band due to the change of particle size. (c.) inverse relation of FWHM and particle size r. (d.) Creation of two absorption bands in optical spectra of gold nanorods due to the influence of shape over the LSPR. Figure inspired by [4].

However, if the particle is fixed to a single refractive index but the particle size changes, the full width at half maximum (FWHM) of the absorption band changes

(Figure 3.3b) . In this case, the FWHM change is inversely proportional to the particle size (Figure3.3c). This change is given by

$$\Gamma = a + \frac{b}{r}, \tag{3.4}$$

where $\Gamma = FWHM$, and a and b are related to the refractive index of bulk gold [4].

In a third case, we see how the change in particle shape leads to a change in the absorption profile (Figure 3.3d).In this case, the particle is a rod where the electron localized in the d-band can oscillate with the external field by transverse mode or longitudinal mode [4], as Figure 3.3d shows. These modes are represented in two absorption bands corresponding to the LSPR [51].

The variables of shape, size, and chemical media can therefore influence the optical properties of colloidal gold nanoparticles. This behavior is shown and further examined in Chapters 5 and 6.

3.2.2 Transient Absorption Spectroscopy (TA)

This section presents the basic concept and experimental setup of transient absorption spectroscopy, which is used to measured the electron dynamics of LSPR in colloidal gold nanoparticles over the picoseconds time range.

What does Transient Absorption Spectroscopy measure?

Femtosecond transient absorption spectroscopy (fs-TA) measures ultrafast photoinduced processes that occur in the sample's excited electronic states. Pulsed photons with a specific energy are used to excite a group of electrons from the ground state to the excited state. These photons are called the pump pulse. The probe pulse sets the spectral sweep range (UV, VIS, or IR), and should be sent through the sample with

a delay time τ relative to the pump pulse. Therefore, the difference between the excited state absorption spectrum and the fundamental state absorption spectrum will be obtained. This generates the spectrum denoted by the function ΔA.

$$\Delta A(\lambda) = -\log(I(\lambda)_{pumped}/I(\lambda)_{unpumped}) \tag{3.5}$$

Information contained in the ΔA function

Once the pump and probe are aligned on the sample, the delay time τ between the pump and probe is varied so that the ΔA spectrum adopts the configuration of a two-variable function, where time τ and wavelength λ are the variables ($\Delta A(\tau, \lambda)$). The function $\Delta A(\tau, \lambda)$ contains information related to the photoexcited dynamics on the sample.

For example, this experiment can yield information regarding dynamics of solvated chemical species [52], excited-state energy migration [53], scattering of photoexcited charge carriers [54], electron transfer [55], isomerization [56],inter-system crossing [57], and many more [58]. This type of photoexcited dynamics is extracted from the spectra of the function $\Delta A(\tau, \lambda)$. The contributions that are extracted from the $\Delta A(\tau, \lambda)$ spectrum are listed as follows:

1. ground-state bleach.
2. stimulated emission.
3. excited-state absorption.
4. product absorption.

Each of the contributions in a TA excitation process listed above can be identified in a typical TA spectrum; Figure 3.4 shows a schematic representation of these dynamic contributions.

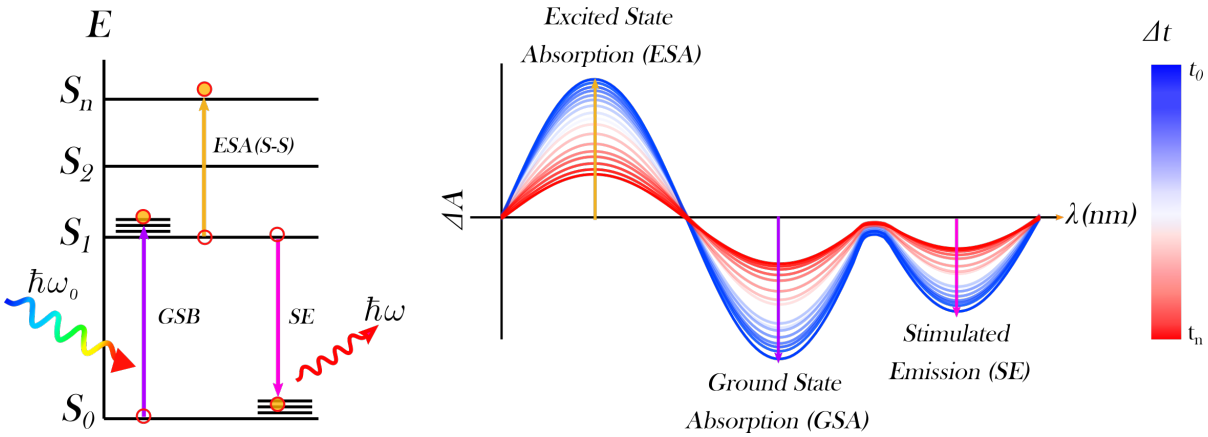

Figure 3.4: Schematic representation of photoexcited dynamics in TA. Left, molecular energy diagram and possible electron stated in a TA process; Excited-State Absorption (ESA), Ground State Absorption (GSB), and Stimulate Emission (SE). Right, schematic representation of a typical TA spectrum in different intervals delay time.

Ground-state bleach

The ground-state bleach is the contribution where the electrons in the ground state energy are promoted to the excited states. In this case, the number of occupied states are reduced in the ground state energy levels by the external incident of the pump pulse. Consequently, when the system is excited, the population of the occupied ground states is smaller than the population of the occupied ground states when the system is not excited. The difference is illustrated in Figure 3.4 by the emergence of a negative contribution on the $\Delta A(\tau, \lambda)$ spectrum.

Stimulated emission

In a two-level system, the Einstein coefficients (A_{12}, A_{21}) are defined as equal; which leads to an energy release by the emission of a second photon when the system decay from the excited state to the ground state due to probe pulse action (see Figure 3.5). This is known as stimulated emission, which increases the light intensity; consequently, a negative signal in the spectrum is observed (see spectrum Figure 3.4).

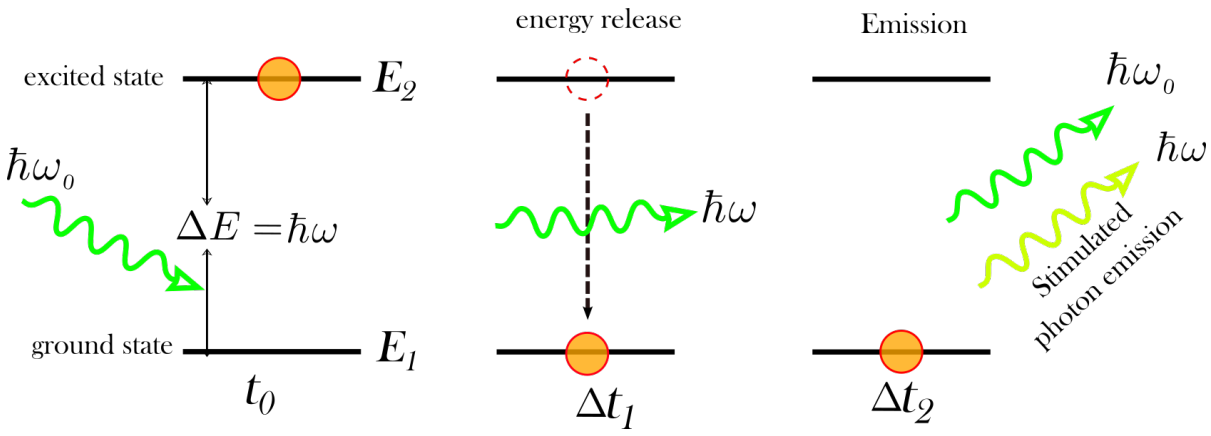

Figure 3.5: schematic representation of stimulated emission in a system of two levels.Graphic inspired by Wikimedia Commons, file: Stimulated Emission.svg.https://commons.wikimedia.org/wiki/File:Stimulated_Emission.svg

3.2.3 Excited-State Absorption

Once the system is excited by the pump, it is possible to promote the occupied excited states to higher excited states. This occurs when the system absorbs the specific wavelengths of the probe pulse that allow for these optical transitions. These transitions are positive in the $\Delta A(\tau, \lambda)$ spectrum, and when it does not overlap with the GSB/SE, can be a useful signature to study the dynamics of the excited state (see Figure 3.4).

Transient Absorption Spectroscopy and LSPR dynamics in colloidal gold nanoparticles

The previous sections discussed the plasmon effect on gold nanoparticles and its strong dependence on shape, size, and chemical media around the particle. The plasmon effect has two essential properties:

1. Capture far-field radiation and concentrate it below the diffraction limit[2].
2. produce strong near-fields that result in extreme field enhancements [59].

However, the plasmon effect has a finite lifetime, which is in the range of 10 ps [60]. Even though the plasmon lifetime seems minuscule, it is sufficient time to generate different processes in the dynamic states of the electrons The plasmon lifetime can be fragmented in the subsequent consecutive processes: *plasmon resonance, non-thermal electron distribution, hot electron distribution, and finally vibrational resonance* [61]. Figure 6.6 shows the sequence of plasmon lifetime and approximate time scales.

[2]diffraction limit $d = \frac{\lambda}{2n\sin\theta} = \frac{\lambda}{2NA}$, NA as numerical aperture

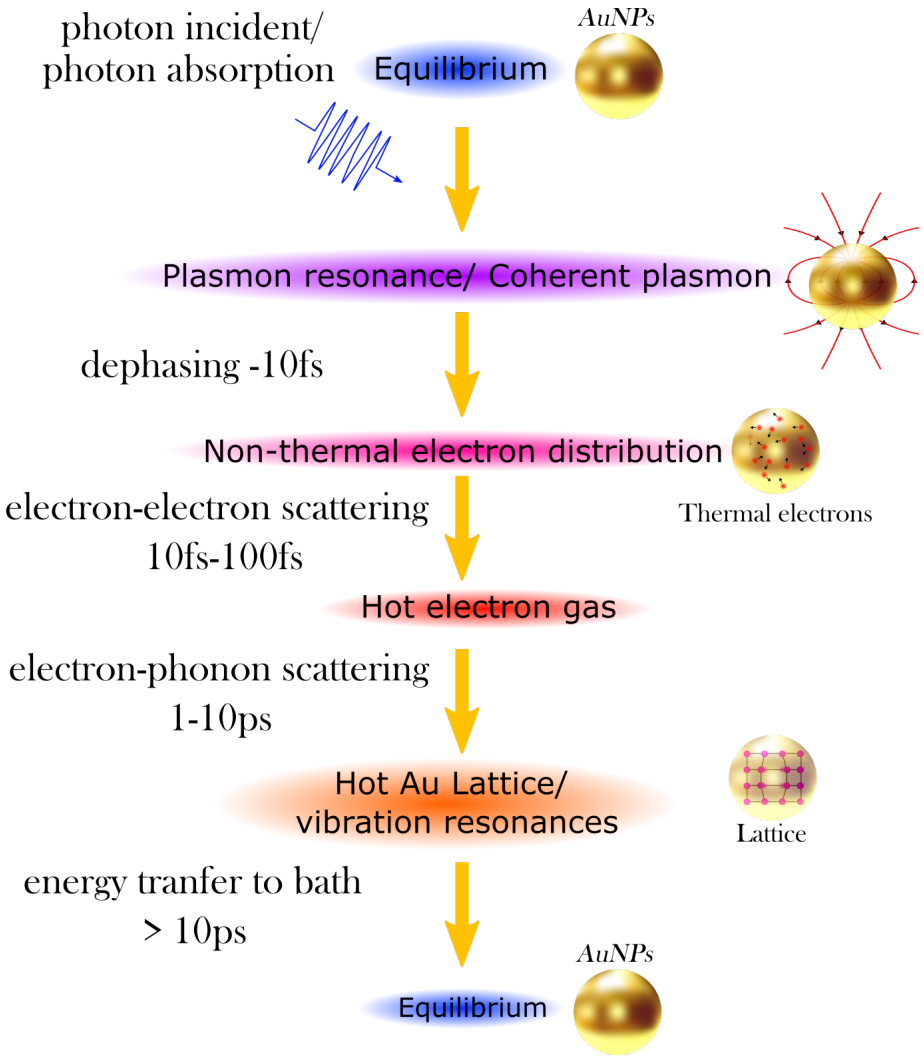

Figure 3.6: Diagram of the lifetime of a plasmon, denoting the sequence decay mechanisms with approximate time scales. Graphic inspired by [5]

It is essential to emphasize that the time scales noted in Figure 3.6. should not be assumed as exact. For example, in some small particles it was found that the heat is transferred to the bath before the electron-phonon coupling process is complete [61–63].

Before photo excitation (equilibrium), the electrons satisfy the Fermi-Dirac distribution [6]. However, after the electrons absorb a energy value of $\hbar\omega_0$ (eV), only the electrons with energy less/or equal to $\hbar\omega_0$ (eV), are excited from below the Fermi level to electronic levels up to $\hbar\omega_0$ (eV) above the Fermi level [6, 64]. Consequently, the electron distribution in this state does not satisfy a Fermi-Dirac distribution, and they will adopt a non-thermal distribution [6], as Figure 3.7 shows.

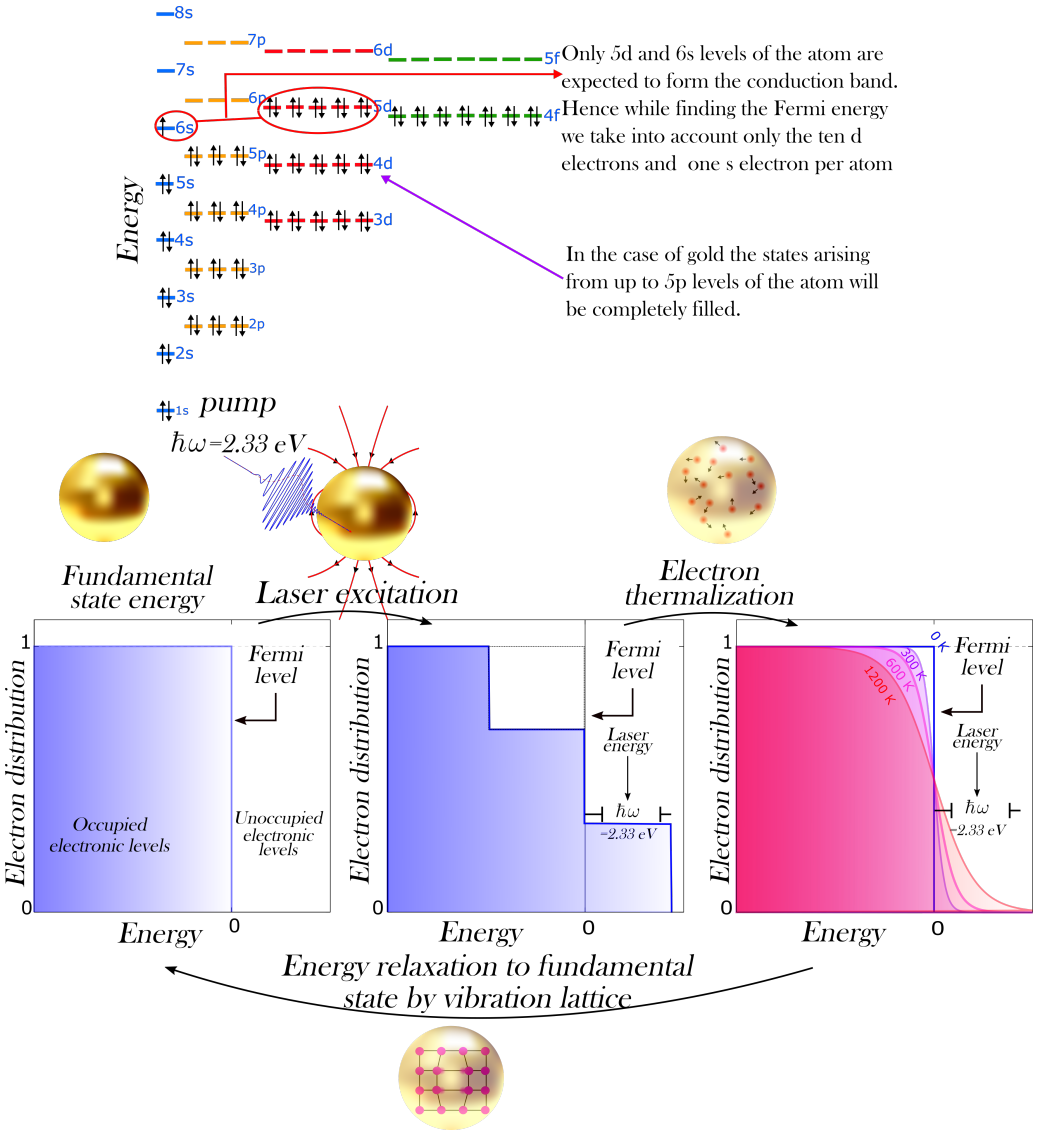

Figure 3.7: The upper panel represents a gold electronic configuration. This representation was adapted from https://www.webelements.com/gold/atoms.html.The lower panel shows a schematic representation of electron distribution, in a gold nanoparticle, after photoexcitation. All electron states below the Fermi energy are occupied in the time zero. After the particle interacts with the external photon, the plasmon effect appears. As a result, some electrons are promoted to a higher energy level above the Fermi level, and the initial electron distribution changes. The maximal energy is equal to the excitation energy (for example, in this case, it is 2.33eV). The electron distribution adopted for the electron gas is designated non-thermal electron distribution, which relaxes (or thermalizes) by electron-electron interaction. In the next moment, the cooling of the electron gas is reached by electron-phonon coupling and phonon-phonon interactions. Conclusively, the electronic distribution returns to the starting configuration. All details can be found in *Stephan Link and Mostafa A. El-Sayed* [6], from which the information and illustration were adopted and inspired.

Additionally, the plasmon can decay via two pathways: radiatively by emitting a photon, or non-radiatively by generating electron-hole pairs [65], as Figure 3.8 shows.

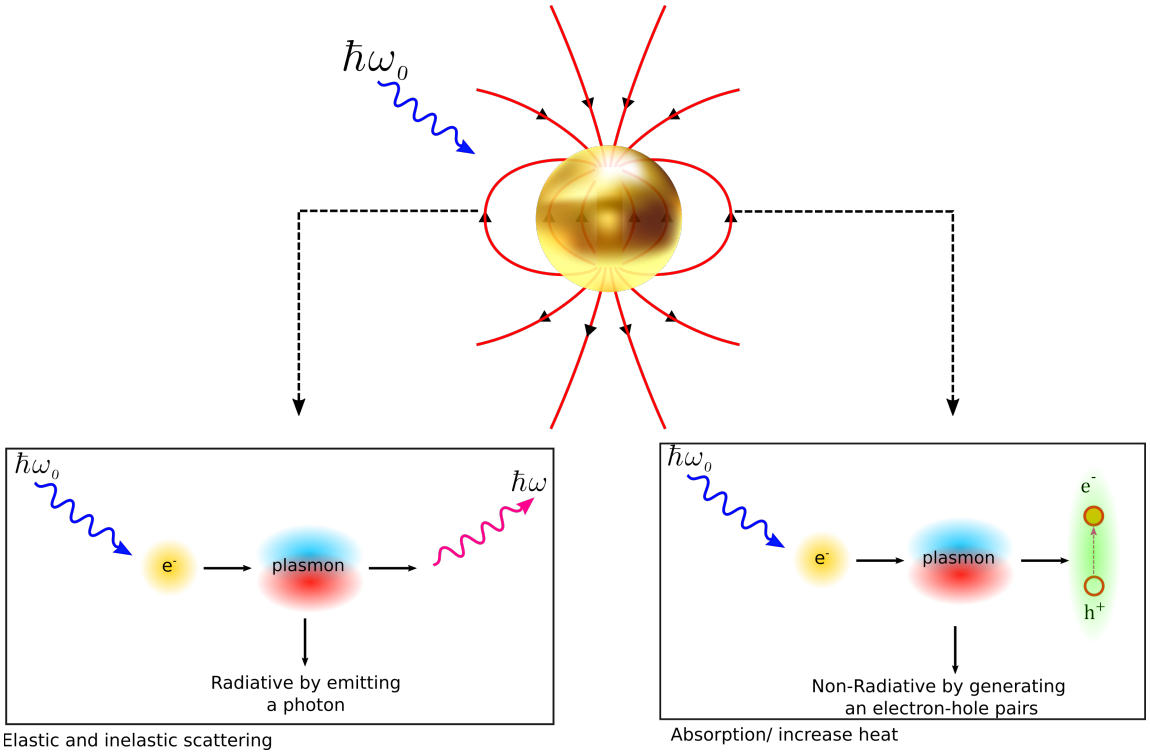

Figure 3.8: schematic representation of the decay plasmon process. Radiative by emitting a photon or Non-radiative by generating electron-hole pairs

The non-radiative plasmon decay causes a temperature increase in the nanoparticle environment and excitations of the hot electrons. The electrons are promoted to higher energy levels from the d-band to energy levels above the Fermi level, by intraband transitions [7]. This requires photons with an energy equal or greater than 2.4eV [66]. The electron transition by non-radiative decay is shown in Figure 3.9. TA spectroscopy allows us to monitor these various plasmon decay processes. The details regarding the experimental setup are shown in the next section.

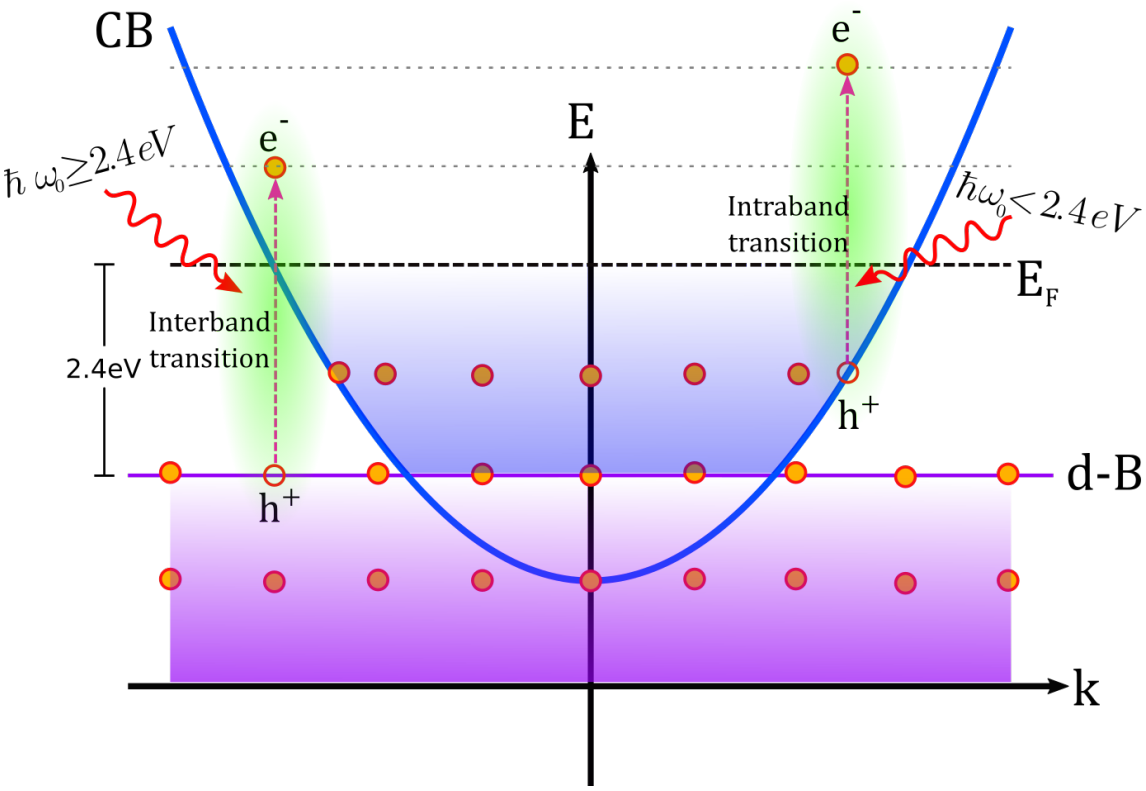

Figure 3.9: Schematic representation of plasmon decay process. Radiative by emitting a photon or Non-radiative by generating electron-hole pairs. Graphic inspired by [7]

Basic principles of TA setup

TA spectroscopy bases its operation on synchronizing two photon groups in order to monitor the induced absorption in the test sample; the photons are named pump pulses and broadband probe pulses. In a general case, light is the fundamental element in the induced absorption process [67]. The photons (light) have three parameters, namely, energy, polarization, and intensity; these parameters will be tuned precisely to induce various nonequilibrium phenomena in the sample by an

electron-photon interaction. Examples are resonant excitation of quasiparticles as plasmons or light-matter interaction [67].

Figure 3.10 shows the schematic overview of the transient absorption setup used in this research. For our experiment, the laser amplifier (PHAROS) pulse duration is 200 fs and the effective repetition rate is 1 kHz (1030 nm output wavelength). The output of the PHAROS was split into two arms. 80% of the PHAROS output is sent to an optical parametric amplifier (ORPHEUS) for to generate tunable photon energies that are utilized as the pump pulses to photoexcite the sample. The remaining 20% of the PHAROS output are sent through an optical delay stage and a white light continuum generator section to create the probe pulses. The pump and probe are focused at the sample in the same face of the 2 mm quartz cuvette (front path), and the probe beam is further directed into the detector. A half-wave plate is used to set the polarization of the pump beam at magic angle relative to the probe beam. The synchronisation of the pump on and pump off conditions is modulated by an optical chopper in the pump path.

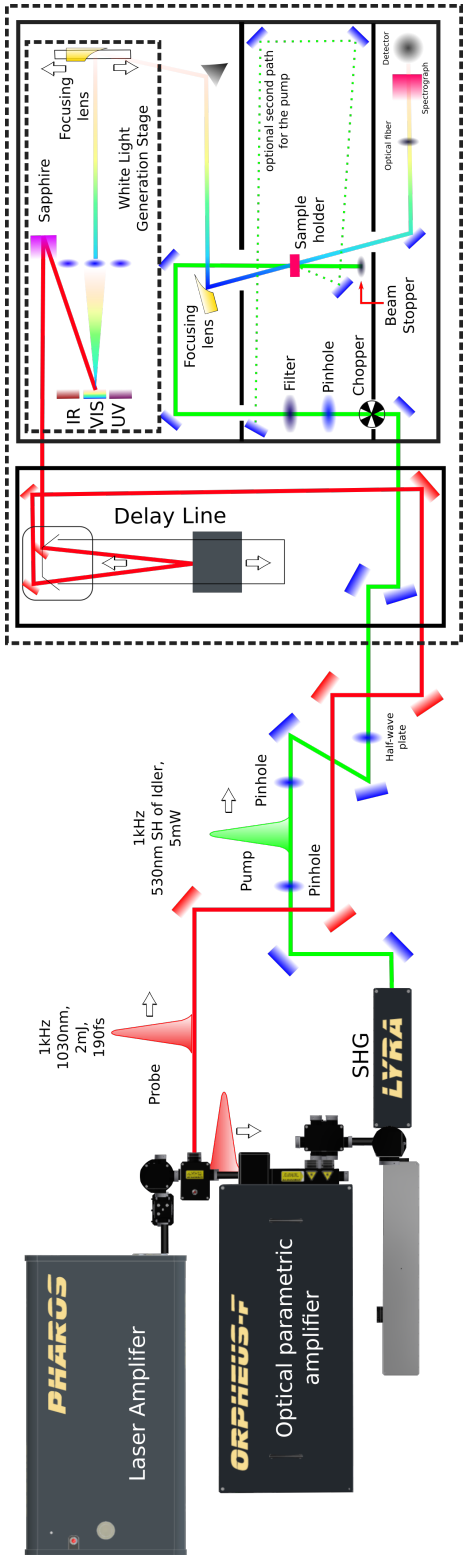

Figure 3.10: Schematic representation of the optical layout of transient absorption spectroscopy setup used in this research.

Optical Parametric Amplifier

The optical parametric amplifier (OPA) is an optical setup that converts the fundamental laser wavelength (from PHAROS) into variable wavelengths through a standard parametric amplification process. The OPA system used in this research is named ORPHEUS. The ORPHEUS operation is based on the OPA process, where a photon with a fundamental frequency (ω_0) is converted into two photons with lower frequency. The first one is named signal (ω_s), and the second one is idler(ω_i). Therefore, it is possible to define the OPA process as $\omega_0 = \omega_s + \omega_i$.

ORPHEUS bases its operation on a two-stage of the white-light continuum. In this case, the wavelength tuning is set by automated translation and rotation stages on several critical optical components. The basic configuration of the two-stage OPA system is fragmented in 4 regions inside of ORPHEUS (Figure 3.11):

1. White light continuum generator
2. Second harmonic of the pump beam generator
3. First amplification stage (a non-collinear two pass pre-amplifier)
4. Second amplification stage (a collinear power amplifier)

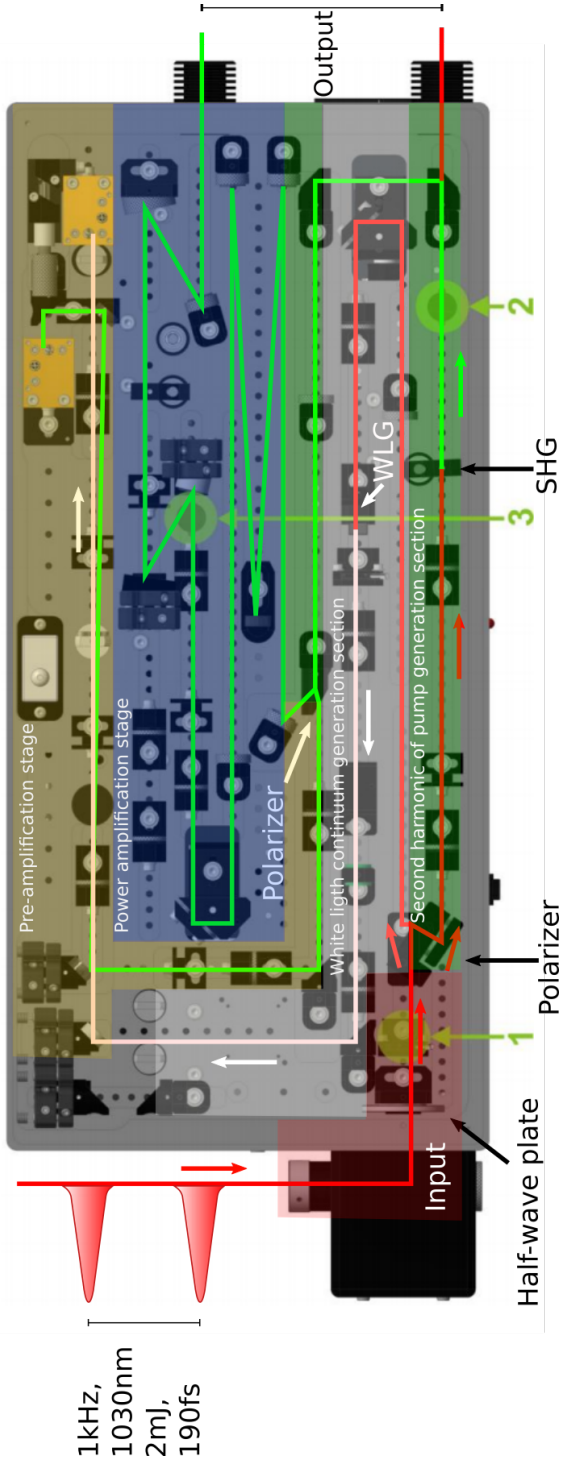

Figure 3.11: Schematic representation of optical layout of OPA-ORPHEUS.The points marked with the numbers 1 , 2, and 3 represent the irises used to align the input beam.

Therefore, it gives the possibility to tune the wavelength of the signal between 650–1010 nm and the idler between 1050–2500 nm. By the use of second harmonics (SH), frequency hopping (FH), and difference-frequency generation (DFG) with the signal and idler beams, it is possible to obtain a broad range of output wavelengths from the OPA. A summary of output wavelengths and the interactions used to make them is shown Table 3.2:

Table 3.2: Output wavelength interactions from the OPA

Wavelength	Interactions
325–450 nm	SH of Signal
325–505 nm	SH of Signal
525–650 nm	SH of Idler
600–700 nm	SH of Idler
210–252 nm	FH of Signal
263–325 nm	FH of Idler

3.3 Raman Spectroscopy/ Vibrational properties of nanoparticles

In addition, to the optical absorption processes explained above, there are also vibrational processes that can be activated by the incidence of monochromatic light on materials (in this case, gold nanoparticles). These vibrational modes can be detected using Raman spectroscopy [68]. This experimental technique has a theoretical basis, which will be explained in this section.

Classical theory of Raman scattering

While light interacts with a molecule, the electromagnetic field $E(r,t)$ of the molecule can be considered a constant [8,69]. Because the wavelength is much larger than the system size, the field is defined as:

$$E = E_0 Cos(2\pi\nu_0 t) \tag{3.6}$$

The interaction of the electric field with the molecule induces a dipole moment in the molecule due to the charge distribution by the presence of $E(r,t)$ [8, 70]. The dipole moment is written as follows,

$$\vec{P} = \alpha\vec{E} \tag{3.7}$$

Where α is the polarisability of the system [8, 70]. Combining equations 3.6 and 3.7 we find $\vec{P}$ be written as:

$$\vec{P} = \alpha E_0 Cos(2\pi\nu_0 t) \tag{3.8}$$

.

Where ν_0 is the initial frequency [8, 71]. Because the molecule does not prossess symmetry, the dipole moment and the electric field will not have the same direction; thus, the electronic cloud will be asymmetric, leading to defining the polarization as a tensor; in cartesian coordinates, the polarization tensor is defined as:

$$\begin{pmatrix} P_x \\ P_y \\ P_z \end{pmatrix} = \begin{pmatrix} \alpha_{1,1} & \alpha_{1,2} & \alpha_{1,3} \\ \alpha_{2,1} & \alpha_{2,2} & \alpha_{2,3} \\ \alpha_{3,1} & \alpha_{3,2} & \alpha_{3,3} \end{pmatrix} \begin{pmatrix} E_x \\ E_y \\ E_z \end{pmatrix} \tag{3.9}$$

The displacements r, concerning their equilibrium position, are considered harmonic and are written in terms of

$$r = r_0 Cos(2\pi\nu_0^{'}t) \tag{3.10}$$

Considering the low-frequency oscillations, the polarization can be expressed as a Taylor series, that is:

$$\alpha(q) = \alpha_0 + \left.\frac{\partial\alpha}{\alpha r}\right|_{r_0} \cdot r + \cdots \tag{3.11}$$

Rewriting equation 3.8 in terms of the equation 3.11, results in:

$$P = \alpha_0 E_0 Cos(2\pi\nu_0 t) + \left.\frac{\partial\alpha}{\alpha r}\right|_{r_0} \cdot r E_0 Cos(2\pi\nu_0^{'}t) Cos(2\pi\nu_0 t) \tag{3.12}$$

By combining the two terms of the second member of the above equation, we obtain;

$$P = \alpha_0 E_0 Cos(2\pi\nu_0 t) + \frac{1}{2}\left.\frac{\partial\alpha}{\alpha r}\right|_{r_0} \cdot r E_0 \left(Cos(2\pi\nu_0^{'}t + 2\pi\nu_0 t) + Cos(2\pi\nu_0^{'}t - 2\pi\nu_0 t) \right) \tag{3.13}$$

Finally, the following relationship is obtained:

$$P = \alpha_0 E_0 Cos(2\pi\nu_0 t) + \frac{1}{2}\left.\frac{\partial\alpha}{\alpha r}\right|_{r_0} \cdot r E_0 \left(Cos(2\pi(\nu_0^{'}+\nu_0)t) + Cos(2\pi(\nu_0^{'}-\nu_0)t) \right) \tag{3.14}$$

The first term of this equation represents the Rayleigh scattering, the second term is considered as the Anti-Stokes Raman scattering, and finally, the third term represents the Stokes Raman scattering [8,72]. In addition, it is known that the dipole radiation

intensity in the molecule is proportional to the second dipolar variation moment in time, i.e.:

$$I \sim \left(\frac{\partial^2 P}{\partial t^2}\right) \tag{3.15}$$

Conjugating the equations 3.14 and 3.15, the following relationship is obtained.

$$I_r \propto \alpha \nu_0^4 \alpha_0^4 I_0 \tag{3.16}$$

This term is the intensity of Rayleigh scattering.

$$I_s \propto (\nu_0 - \nu')^4 \left(\frac{\partial \alpha}{\partial r}\bigg|_{r_0}\right) I_0 \tag{3.17}$$

The equation 3.17 is the intensity of the Stokes-Raman scattering, and finally, it is obtained:

$$I_{A-S} \propto (\nu_0 + \nu')^4 \left(\frac{\partial \alpha}{\partial r}\bigg|_{r_0}\right) I_0 \tag{3.18}$$

The term of the equation 3.18 represents the intensity of the Anti-Stokes Raman scattering. In theoretical terms, as shown, it was found that the intensity of the Stokes-Raman and Anti-Stokes Raman scattering has the same intensity, which is not following the experimental measures. However, Quantum Mechanics predicts that the Anti-Stokes Raman scattering has a lower intensity than the Stokes Raman scattering intensity, in accordance with the experiment [8, 73].

Cross section-Raman Scattering

It has been found, so far, that there is a strong dependence of the Stokes-Raman signal on the wavelength radiation and polarizability [8, 74]. However, the factor

known as the cross-section σ_j has a significant influence on the Stokes-Raman scattering [8, 68]. The cross-section is proportional to the probability of a photon interacting with a molecule scattered with a Stokes-Raman scattering. By this term, it is possible to relate the scattering intensity to the corresponding cross-section, i.e.

$$I_{SR} = I_0 \sigma_j D dz \tag{3.19}$$

In this relationship, D represents the number of molecules per cubic centimeter, known as the numerical scattering density. While dz is the optical path length of the radiation within the sample, in most cases referring to these types of scattering, this radiation is a laser [8, 75]. In addition to this, a functional form of the cross-section, which does not depend on the scattering intensity, is defined as follows:

$$\sigma_j^0 = \frac{\sigma_j}{(\bar{\nu}_0 - \bar{\nu}_j)^4} \tag{3.20}$$

Where $(\bar{\nu}_0 - \bar{\nu}_j)^4$ is known as the wave numbers measured in cm^{-1}. With this definition, it is possible to write a relationship in terms of the phonons number per time unit, that is:

$$P_r = P_0 \sigma_j^{'} D dz \tag{3.21}$$

Where P_r and P_0 are measured in photons per second [8, 74].This relationship allows finding the number of photons per second through:

$$P_r = P_0 \sigma_j^0 \bar{\nu}_0 (\bar{\nu}_0 - \bar{\nu}_j)^4 D dz \tag{3.22}$$

Quantum mechanics and Stokes-Raman scattering

The incidence of a photon on a molecule causes a transition to an excited or virtual state of energy [8, 76]. However, a virtual state is not a real energy state; thus, it does not correspond to any possible state of rotation, vibration, or electronics in the molecule [77]. It is considered a forbidden state in the quantum mechanics context [78]. If the molecule were to acquire a virtual state, it would recombine to one of the fundamental states by emitting a photon in the process [8,79]. Furthermore, in this recombination process, there are three possibilities of recombination. It depends on the relationship between the initial state energy and the final state energy. If the initial state energy equals the final state energy, the dispersed photon will have the same initial energy, known as Rayleigh scattering [8,80].

On the other hand, if the molecule recombines to a state of higher energy than the initial one, the molecule acquires energy, and it will emit a photon. This process is known as Anti-Stokes-Raman scattering, and finally, if the molecule acquires a state of energy lower than the initial one, the molecule loses energy. This process is known as Stokes Raman scattering [77]. See figure 3.12

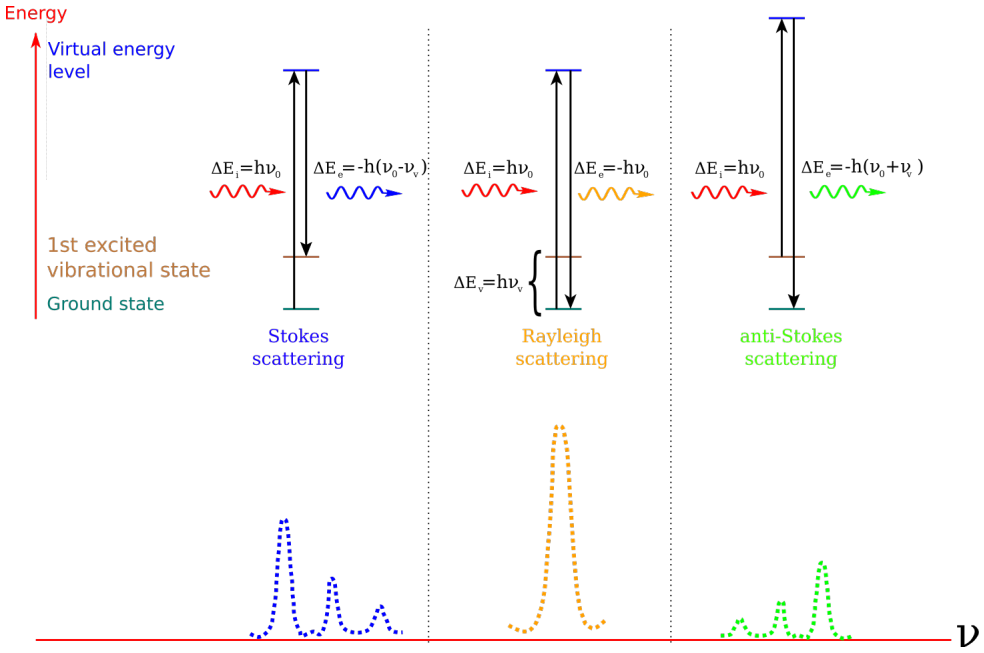

Figure 3.12: Diagram regarding recombination process by a molecule from a virtual state. Graphic inspired by [8]

These processes can be explained using perturbation theory [76, 81], that is:

$$\sum C_p(t) e^{\frac{i(E_{pn})t}{\hbar}} V_{pn} = -\frac{\hbar}{i}\frac{dC_p(t)}{dt} \tag{3.23}$$

At this point, the matrix is a disturbance process by which the transition from the state p to n occurs. When the coefficients C_p are known, it is possible to find the second-order transition coefficients, written as;

$$\sum C_p^1(t) e^{\frac{i(E_{pn})t}{\hbar}} V_{pn} = -\frac{\hbar}{i}\frac{dC_p^2(t)}{dt} \tag{3.24}$$

Thus, the main coefficients will be written as follows:

$$C_p(t) = \frac{V_{0if}}{2i\hbar}\left(\frac{1-e^{i(\omega_{pi}+\omega)t}}{\omega_{pi}+\omega} - \frac{1-e^{i(\omega_{pi}-\omega)t}}{\omega_{pi}-\omega}\right) \tag{3.25}$$

Thus, it is found that the probability of the Stokes Raman dispersion will be:

$$P_{i\longrightarrow f} \propto \sum \frac{V_{ji}V_{ft}}{(\omega_{ji}+\omega)-(\omega_{ji}+\omega^{\otimes})} (3.26)$$

Considering that $\omega^{\otimes} = \omega - \omega_{if}$, the probability of generating a Stokes-Raman spread is

$$P_{i\longrightarrow f} \propto \sum \frac{V_{ji}V_{ft}}{(\omega_{ji}^{2}+\omega^{2})} (3.27)$$

Therefore, it is possible to reproduce polarizability as it was classically reproduced and consistent with experimental effects obtained in Stokes-Raman intensities [77]. The consolidation of the Raman theory, whether classical or quantum mechanics, allowed the consolidation of experimental processes and measurements that were difficult to explain at the time [82]. This allows defining Raman spectroscopy, in a first approach, as a technique that allows measuring molecules' vibrations. Using the Raman spectrum of these vibrations, it is possible to identify which of the chemical bonds are present in a sample [77]. As secondary results of Raman scattering is the existence of fluorescence in the measured spectrum is added as a difficulty; see figure 3.13.

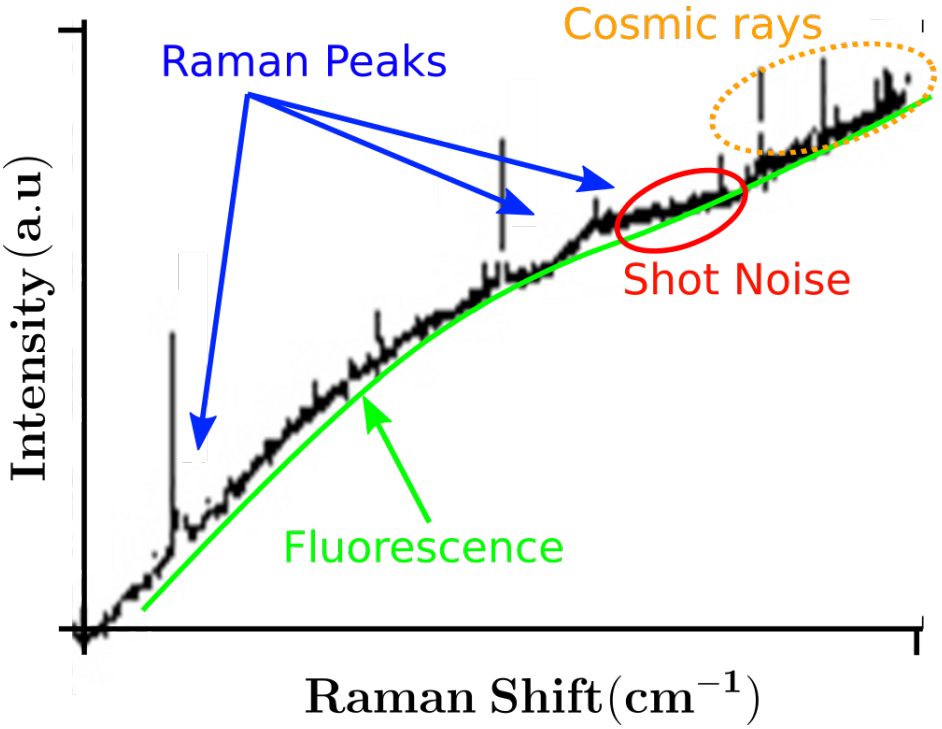

Figure 3.13: Elements that make the Raman spectrum difficult to read and decrease signal intensity. Graphic inspired and extracted from [9]

Chapter 4

Simulation techniques

A complementary computational study was carried out to investigate the role of the microscopic structure of the metal/aqueous environment interface in the final shape of the synthesized gold nanoparticles. This chapter summarises the simulation techniques used throughout this work, including molecular dynamics and density functional theory, to motivate such a discussion.

4.1 Molecular Dynamics

Molecular dynamic (MD) simulations enable us to investigate the macroscopic behavior of a physical system using the information obtained from its microscopic interactions. Indeed, results from MD simulations can be used to understand and interpret experiments and reproduce conditions that are difficult to access in the laboratory. In this work, MD simulations were used to investigate the microscopic details of metal/solvent environments to understand the origin of the asymmetric growth mechanism observed in the synthesized gold nanoparticles. In particular, our simulations provide a microscopic understanding of the role of L-asparagine in controlling the growth of gold nanoparticles at different pH conditions.

Classical MD simulations integrate Newton's equations of motions for a system of N point-like atoms. Quantum mechanical effects are implicitly incorporated into empirical or semi-empirical potential energies that account for bonded and non-bonded interactions. The classical trajectories obtained with this procedure allow one to compute thermodynamic properties via statistical mechanics principles [83, 84]. In this section, a brief introduction to MD simulations is presented.

4.1.1 Equations of motion

The macroscopic state of a system of N particles is defined by the complete set of positions $\{\mathbf{r}_i\}$ and momenta $\{\mathbf{p}_i = m_i\mathbf{v}_i\}$ with $\mathbf{v}_i$ the instantaneous velocity of the i-particle with mass m_i. The Hamiltonian H of the system can be written as

$$H(\{\mathbf{p}_i\},\{\mathbf{r}_i\}) = \sum_{i=1}^{N} \frac{\mathbf{p}_i^2}{2m_i} + U(\{\mathbf{r}_i\}), \tag{4.1}$$

with $U(\{\mathbf{r}_i\})$ the potential energy of the system [85] [86]. The force acting on the k-particle due to the other particles present in the simulation is obtained from the negative gradient of the potential energy, namely

$$\mathbf{F}_k = -\nabla_k U(\{\mathbf{r}_i\}). \tag{4.2}$$

In this respect, the problem reduces to integrate numerically Hamilton's equations:

$$\dot{\mathbf{r}}_i = \frac{\partial H}{\partial \mathbf{p}_i} = \frac{\mathbf{p}_i}{m_i}, \tag{4.3}$$

and

$$\dot{\mathbf{p}}_i = -\frac{\partial H}{\partial \mathbf{r}_i} = -\frac{\partial U}{\partial \mathbf{r}_i} = \mathbf{F}_i, \tag{4.4}$$

where $\dot{A}$ means the derivative of A with respect to time. In this work, equations of motion have been integrated using the Verlet algorithm [83, 86, 87]. The Verlet algorithm is derived by using a Taylor expansion on the position $\mathbf{r}_i$ of a particle at the time $t + \Delta t$. This is

$$\mathbf{r}_i(t+\Delta t) = 2\mathbf{r}_i(t) - \mathbf{r}_i(t-\Delta t) + \frac{F_i(t)}{m_i}\Delta t^2 + 2\mathcal{O}(\Delta t^4). \tag{4.5}$$

In this case, the estimated error in the new position is of order Δt^4, with Δt the time step for molecular dynamics simulation [83, 85]. The Verlet algorithm does not employ the velocity to compute the new position. However, the velocity of the particle can be obtained from its position at the times t and $t + \Delta t$ [83, 85].

$$\mathbf{v}_i(t) = \frac{\mathbf{r}_i(t + \Delta t) - \mathbf{r}_i(t - \Delta t)}{2\Delta t} + \mathcal{O}(\Delta t^2)\,. \tag{4.6}$$

Hence, the estimated error in the velocity is of order Δt^2. At each time step, the temperature, potential energy, and the total energy of the system are calculated. The total energy should be conserved during the MD simulation [83, 85]. Once all calculations are completed, the old positions and velocities at time $t - \Delta t$ are discarded. Thus, the new positions and velocities define the next starting point. This process is repeated a given number of times until the desired simulation time is reached [83, 85].

4.1.2 Statistical ensembles

In some cases, the experiments use temperature and pressure as variables. That means all pre-equilibration and final production in a simulation or experiment sample the isothermal-isobaric (NPT) ensemble [83,85]. An NPT ensemble was used to carry out the molecular dynamics simulations. The resulting behavior is shown and further examined in the results of this thesis, Chapter 5. The volume V, in an NPT ensemble, is a dynamic variable entering the equations of motion [83, 85, 86].

4.1.3 Interaction potentials

Typically, the total interaction potential is described by the sum of non-bonded and bonded interactions. The non-bonded interactions are pair-additive[1] and centrosymmetric [88]. They include the electrostatic interactions and the Lennard-Jones potential [83, 85]. The set of bonded and non-bonded interactions defines the force field [83]. There are numerous force fields, defined according to the system and the interaction potentials parameters. The choice of the force field is based on reproducing target properties of the system, namely density, structure factor, etc. A force field is built up from two distinct components: (i) the equations used to generate the potential energies and their derivatives, and (ii) the parameters included in this set of equations.

In this work, the forcefield CGenFF[2] [89], implemented in GROMACS-96[3], was used to carry out the simulations.

4.1.4 Cut-off scheme and treatment of long range interactions

As one increases the system size, computing pairwise interactions for all particles present in the simulation becomes very expensive. For that reason, the evaluation of pairwise interactions, $U(r_{ij})$ is normally restricted to a local environment within a cutoff radius[4] [83, 85]. To avoid numerical problems associated with a discontinuous potential, the Lennard-Jones potential is usually modified by a switch/shift function

[1] The pair-additive approximation means that no polarization and charge transfer effects are included, such as the solute polarization by solvent, variation of charge distributions with conformational changes, etc.

[2] More details of the forcefield: http://mackerell.umaryland.edu/~kenno/cgenff/

[3] Details regards to GROMACS: http://manual.gromacs.org/current/index.html

[4] In theoretical physics, cutoff is an arbitrary maximal or minimal value of energy, momentum, or length, used in order that objects with larger or smaller values than these physical quantities are ignored in some calculation.

that ensures that the energy smoothly goes to zero when approaching the cutoff distance [83, 85].

In computer simulations, one artificially considers infinite systems by introducing periodic boundary conditions. Its use guarantees translational invariance that implies, in the absence of external forces, the conservation of linear momentum [83, 90]. In the case of crystal systems, a translation operation is implemented in order to occupy an infinity space by the unit cell, see figure 4.1.

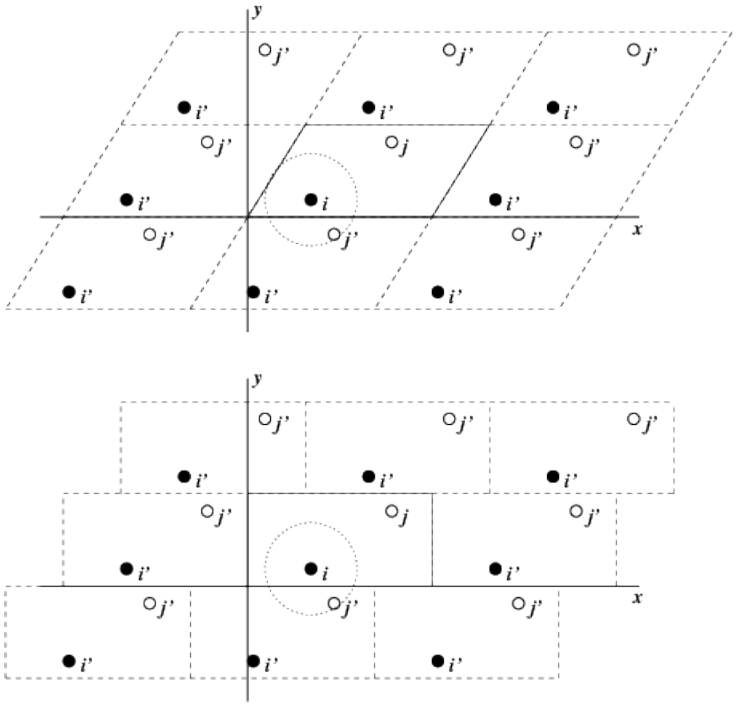

Figure 4.1: Periodic boundary conditions in two dimensions. Image extracted from http://manual.gromacs.org/documentation/2019/reference-manual/algorithms/periodic-boundary-conditions.html#equation-eqngridrc

This process naturally forms a convenient axis system for measuring the coordinates of the N atoms. The number density in the central box, i.e. the entire system, is conserved [83,85]. The periodic boundary conditions are combined with the minimum

image convention, the nearest image of each particle is considered for short-range non-bonded interaction terms [83, 85].

Finally, the long-range electrostatic interactions are calculated by lattice sum methods that exploit the periodicity of the simulation box [83, 85, 86]. Electrostatic interactions are commonly evaluated using a summation technique named the Particle Mesh Ewald (PME). In practice, one divides the electrostatic interactions into two contributions. The first one is short-range and is evaluated in real space. The second one is long-range and is computed in Fourier space, and includes the interactions of the respective charge with all its periodic images [83, 85].

4.1.5 Weighted Histogram Analysis Method

An essential result of this work is related to the computation of the affinity of the amino acid to gold surfaces of different orientations in an aqueous environment. It is paramount to compute the potentials of mean force as the amino acid is pulled out from the surface. This pull is performed by applying a harmonic force to the amino acid. The Weighted Histogram Analysis Method (WHAM) is a standard technique used to compute the potential of mean force (PMF) from a set of umbrella sampling simulations [91]. Kumar and coworkers developed the WHAM method for PMF calculation in the 1990s [92].

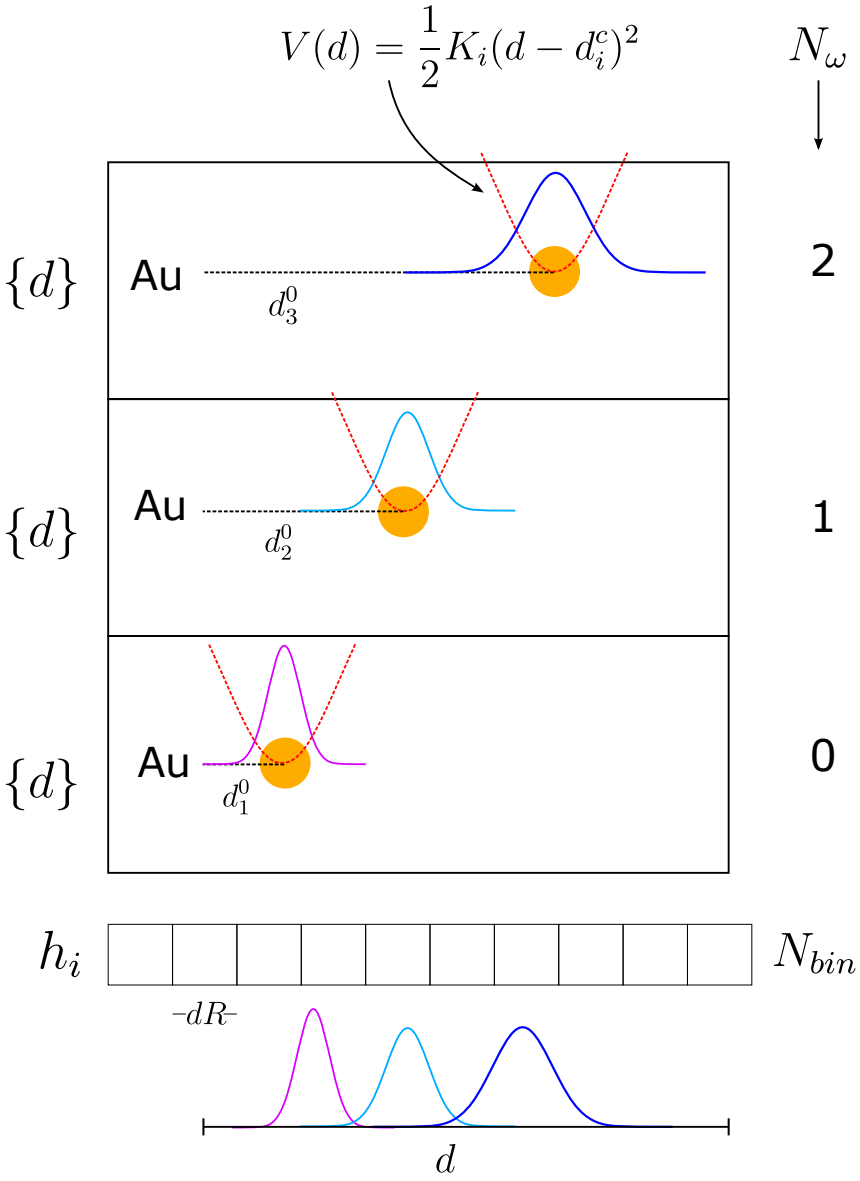

Figure 4.2: Schematic representation of Weighted Histogram Analysis Method.

Figure 4.2 shows a schematic representation of Weighted Histogram Analysis Method, where N_ω represent the number of simulations. In each simulation N_ω the particle (in this case the amino acid) is constrained at d_i^c distance from gold surface by a harmonic potential with a constant K_i. h_i represent the histogram, divided in N_{bin} bins, of distances d_i^c from all N_ω simulations.(Figure 4.2). The PMF is recovered

after the acquisition of the histogram h_i by the iterative solution of the following equations:

$$P^u(d) = \frac{\sum_{i=1}^{N_{bin}} g_i^{-1} h_i(d)}{\sum_{j=1}^{N_{bin}} N_\omega g_j^{-1} \exp[-\beta(V(d) - f_j)]} \tag{4.7}$$

$$\exp(-\beta f_j) = \int d(d) \exp[-\beta(V(d)] P^u(d) \tag{4.8}$$

Where $P^u(d)$ is the probability to find the system at a distance $d(d)$, g_i is a normalization factor, and $\beta = 1/k_B T$. After the convergence of $P^u(d)$, the PMF is calculated by

$$A(d) = -\beta^{-1} \ln \left[\frac{P^u(d)}{P^u(d_0)} \right] \tag{4.9}$$

4.2 Density Functional Theory (DFT)

Classical molecular dynamics cannot provide direct information related to the electronic structure of the system. For this work, we require this information to compare with Raman spectroscopy measurements performed on our samples. In this context, we use density functional theory (DFT).

The Hamiltonian of a many-body system composed of M atoms and N electrons can be reduced to (Born-Oppenheimer or adiabatic approximation)

$$\mathcal{H} = \mathcal{T} + \mathcal{V} + \mathcal{U}\,, \tag{4.10}$$

with $\mathcal{T}$ the kinetic energy of the electrons, $\mathcal{U}$ their potential energy and $\mathcal{V} = \sum_i^N v(\mathbf{r}_i)$ an external potential, usually determined by the interaction of the electrons with the static nuclei.

The energy of the system is a functional of the external potential $v(\mathbf{r})$, namely $E \equiv E[v(\mathbf{r})]$. The electronic density, $\rho(\mathbf{r})$, is given by the functional derivative of the energy with respect to the external potential, i.e.

$$\rho(\mathbf{r}) = \frac{\delta E}{\delta v(\mathbf{r})} \tag{4.11}$$

The Hohenberg-Kohn energy F_{HK} is defined as a functional of the density by using a functional Legendre transform [93] with respect to $E[v(\mathbf{r})]$

$$F_{\mathrm{HK}}[\rho(\mathbf{r})] = E[v(\mathbf{r})] - \int d\mathbf{r}\, \rho(\mathbf{r})\, v(\mathbf{r})\,. \tag{4.12}$$

In general, we are interested in finding the ground state density and energy of the system that correspond to the external potential $v(\mathbf{r})$. We write the energy as a functional of the density, $E_v[\rho(\mathbf{r})]$, which is interpreted as the energy cost necessary to fix the system's density under the influence of an external potential $v(\mathbf{r})$. By using the inverse transform, we obtain

$$E_v[\rho(\mathbf{r})] = F_{\mathrm{HK}}[\rho(\mathbf{r})] + \int d\mathbf{r}\, \rho(\mathbf{r})\, v(\mathbf{r})\,. \tag{4.13}$$

The idea now is to minimize this cost with respect to the density, namely, $\delta E_v/\delta\rho(\mathbf{r}) = 0$, thus

$$\frac{\delta F_{\mathrm{HK}}}{\delta \rho(\mathbf{r})} = -v(\mathbf{r})\,. \tag{4.14}$$

Therefore, the problem reduces to find F_{HK} and $\rho(\mathbf{r})$ satisfying Eq. (4.14) that automatically give the ground state energy of the system.

To find F_{HK}, it is convenient to investigate the non-interacting system $\mathcal{U} = 0$ such that the internal energy reduces to the kinetic energy. In this case, $F_{\mathrm{HK}}[\rho(\mathbf{r})]|_{\mathcal{U}=0} =$

$F_{\rm ni}[\rho(\mathbf{r})]$. Hence, $F_{\rm HK}$ can be separated into noninteracting and interacting terms, i. e.

$$F_{\rm HK}[\rho(\mathbf{r})] = F_{\rm ni}[\rho(\mathbf{r})] + E_{\rm H}[\rho(\mathbf{r})] + E_{\rm xc}[\rho(\mathbf{r})]\,, \tag{4.15}$$

with the Hartree energy $E_{\rm H}$ given by

$$E_{\rm H}[\rho(\mathbf{r})] = \frac{1}{2}\int d\mathbf{r}\int d\mathbf{r}'\,\frac{\rho(\mathbf{r})\rho(\mathbf{r}')}{|\mathbf{r}-\mathbf{r}'|}\,. \tag{4.16}$$

The exchange-correlation energy $E_{\rm xc}$ accounts for energy contributions resulting from the Pauli exclusion principle and electron-electron correlations due to long-range electrostatic interactions. In practice, the functional form of the $E_{\rm xc}$ term is approximated using semi-analytical expressions [94].

Kohn-Sham equations allow us to compute $F_{\rm ni}$ exactly [95]. For a system of N non-interacting electrons, there is an effective potential $v_{\rm eff}$ such that the solution of the equation

$$\left(-\frac{1}{2}\nabla^2 + v_{\rm eff}(\mathbf{r})\right)\psi_i(\mathbf{r}) = \epsilon_i\psi_i(\mathbf{r}) \tag{4.17}$$

satisfies $\rho(\mathbf{r}) = \sum_{i=1}^{N}\psi_i(\mathbf{r})$. The kinetic energy is thus calculated as $F_{\rm ni}[\rho(\mathbf{r})] = \sum_{i=1}^{N}\epsilon_i - \int d\mathbf{r}\,\rho(\mathbf{r})\,v_{\rm eff}(\mathbf{r})$. This expression allows one to compute the effective potential. By taking the functional derivative of Eq. (4.15) with respect to the density, and by using that $\delta F/\delta\rho = -v$, we obtain

$$v_{\rm eff}(\mathbf{r}) = v(\mathbf{r}) + \frac{1}{2}\int d\mathbf{r}'\frac{\rho(\mathbf{r}')}{|\mathbf{r}-\mathbf{r}'|} + \frac{\delta E_{\rm xc}[\rho(\mathbf{r})]}{\delta\rho(\mathbf{r})}\,. \tag{4.18}$$

Equations (4.17) and (4.18) can be solved self-consistently. One starts by guessing the electronic density $\rho(\mathbf{r})$. Since we know the external potential $v(\mathbf{r})$ and the

approximation to E_{xc}, Eq. (4.18) gives $v_{\text{eff}}(\mathbf{r})$. This potential enters Kohn-Sham equations (4.17) and a new density $\rho(\mathbf{r})$ is obtained and used in Eq. (4.18) to compute a new v_{eff}. Upon convergence, this procedure gives the ground state density and energy of the interacting system.

4.2.1 DFT and Raman scattering

DFT is used to calculate Raman spectrum by computing force constants, the resulting vibrational frequencies, and the intensities of the Raman profile. In this case, the computed Raman spectrum was obtained from the simulation of an isolated L-Asparagine molecule using the $B3LYP/6-311++G(d,p)$ functional and the iefpcm water solvent model. All calculations were performed using the Gaussian 09W program package, with the default convergence criteria, and without any constraint on the geometry. The obtained spectra has been labelled as *DFT-L-Asparagine*, pH 6 and *DFT-Lasparagine*, pH 9 (see chapter 5)

Chapter 5

Role of pH in the synthesis and growth of gold nanoparticles using L-asparagine: a combined experimental and simulation study

Title manuscript:

Role of pH in the synthesis and growth of gold nanoparticles using L-asparagine: a combined experimental and simulation study

Ricardo Báez-Cruz, Luis A Baptista1, Samuel Ntim, Shirly Espinoza, Charusheela Ramanan, Robinson Cortes-Huerto and Marialore Sulpizi.

Journal of Physics: Condensed Matter 33 (25), 254005

Author Contribution.

Ricardo Báez-Cruz and **Charusheela Ramanan** designed the research. **Ricardo Báez-Cruz** synthesized the complex AuNP-Asn, performed all experiments, and analyzed the data under the direction of Charusheela Ramanan. **Shirly Espinoza** conducted the Raman scattering measurements. **Robinson Cortes** and **Marialore Sulpizi** designed the modeling. **Luis Baptista** and **Samuel Ntim** carried out the modeling. **Ricardo Báez-Cruz** wrote the manuscript.

5.1 Abstract

The use of biomolecules as capping and reducing agents in the synthesis of metallic nanoparticles constitutes a promising framework to achieve desired functional properties with minimal toxicity. The system's complexity and the large number of variables involved represent a challenge for theoretical and experimental investigations aiming at devising precise synthesis protocols. In this work, we use L-asparagine (Asn), an amino acid building block of large biomolecular systems, to synthesise gold nanoparticles (AuNPs) in aqueous solution at controlled pH. The use of Asn offers a primary system that allows us to understand the role of biomolecules in synthesising metallic nanoparticles. Our results indicate that AuNPs synthesised in acidic (pH 6) and basic (pH 9) environments exhibit somewhat different morphologies. We investigate these AuNPs via Raman scattering experiments and classical molecular dynamics simulations of zwitterionic and anionic Asn states adsorbing on (111)-, (100)-, (110)-, and (311)-oriented gold surfaces. A combined analysis suggests that the underlying mechanism controlling AuNPs geometry correlates with amine's preferential adsorption over ammonium groups, enhanced upon increasing pH. Our simulations reveal that Asn (both zwitterionic and anionic) adsorption on gold (111) is essentially different from adsorption on more open surfaces. Water molecules strongly interact with the gold face-centred-cubic lattice and create traps, on the more open surfaces, that prevent the Asn from diffusing. These results indicate that pH is a relevant parameter in green-synthesis protocols with the capability to control the nanoparticle's geometry, and pave the way to computational studies exploring the effect of water monolayers on the adsorption of small molecules on wet gold surfaces.

5.2 Introduction

Gold nanoparticle (AuNP) systems exhibit high biocompatibility and unique optical and catalytic properties, making them attractive for next-generation medical and imaging applications [96, 97]. Incorporating AuNPs into technology depends on successful size- and shape-engineering [98]. Previously, shape-control and synthesis of anisotropic particles has been achieved by the addition of surfactant agents such as hexadecyl(trimethyl)ammonium bromide (CTAB) [99]. However, these materials result in AuNPs with higher toxicity due to CTAB and contaminant by-products, limiting the widespread use of these AuNPs [100]. There is therefore significant interest in developing alternative, less toxic synthetic routes to shape-controlled AuNPs [101].

Protein- [102] and amino acid-based [103] synthesis protocols have been implemented to control the shape and size of the resulting nanoparticles. The group of 20 proteinogenic $\alpha-$amino acids found in eukaryotes have been used to synthesise AuNPs, acting as both reducing and capping agents [40, 41]. These results indicate that the type of amino acid and experimental conditions determine the AuNPs quality. For example, changes in histidine concentration and pH enables adequate control of the size and particle shape [40]. By contrast, synthesis with L-Asparagine (Asn) produces monodisperse AuNPs, and Asn concentration variation do not induce changes in the AuNPs colour, size, or shape [42]. Alternatively, the pH of the amino acid solution is essential to control the reducing and functionalisation capabilities in AuNPs [43, 44]. This fact prompts the question as to whether pH can be used as an adjustable parameter to control AuNPs geometry.

In addition to experimental characterisation techniques such as transmission electron microscopy (TEM) [104], high-resolution transmission electron microscopy (HR-TEM) [105], ultraviolet-visible spectroscopy (UV-vis spectroscopy) [106], and Raman Spectroscopy [107], computational studies of AuNPs in chemical environments have been performed to resolve the intricate interaction mechanisms occurring at the metal-environment interface. These studies include ab initio density functional theory [108–110] and classical molecular dynamics simulations [111–116]. The typical AuNPs size (ranging from 2 to 10 nm), and the presence of solvent and surfactants, prevent the simulation of systems of realistic size. In this context, the study of simplified models of these systems provides valuable information on the metal surface, usually hidden by the surfactant. Moreover, it helps to predict equilibrium structures based on simple energetic arguments [109, 114, 115].

Here, we rely on a combined simulation-experimental approach to investigate the role of acidic (pH 6) and basic (pH 9) pH conditions in the AuNPs synthesis using Asn as both capping and reducing agent. This choice is motivated by the fact that the acidic (basic) environment is the result of a high concentration of the zwitterionic (anionic) Asn state. We expect that the two distinct chemical forms exhibit different interactions with gold surfaces thus impacting the AuNPs obtained at these pH conditions. In our experiments, we adjust the pH adding small volumes of a stock solution of 100 mM sodium hydroxide. The explicitly treatment of pH in molecular dynamics (MD) simulations, however, is not obvious and is the subject of intense investigations [117]. Here, we do not attempt to adjust the pH of the environment/solution in the simulations explicitly. Instead, we consider zwitterionic and anionic states of Asn, whose excess in solution is related to acidic and basic pH conditions, respectively. We thus compare the adsorption of both Asn states

on (111), (100), (110) and (311) gold surfaces, prevalent in the obtained AuNPs, focusing on the details of the interaction at the interface. Our molecular dynamics simulations reveal that the adsorption of zwitterionic Asn on gold surfaces results from a competing effect between the attraction to the amide group, in agreement with ab initio simulations [108], and the slight repulsion of the ammonium group. By contrast, in the anionic state, the ammonium group is replaced by an amine group, and therefore Asn displays higher gold affinity. Raman spectra for Asn on gold at pH 6 and pH 9 confirm this picture with the respective rise of -NH_3^+ and decrease of -NH_2 intensities for these groups at their characteristic frequencies.

Our MD simulations also provide qualitatively different pictures for the adsorption on the considered gold orientations (crystalline planes). Asn lies essentially flat on (111) and is free to diffuse, with adsorption dominated by the amide group. For the remaining surfaces, the water molecules display a significant structuring, consistent with the underlying fcc structure, close to the gold surface (between 3 and 6 Å). This structure creates energetically favourable locations for Asn on open gold surfaces that prevent it from diffusing.

The chapter is organised as follows: In Section 5.3 we describe the synthesis procedure, characterisation techniques and the computational approach. We present our experimental and theoretical results in Section 5.4. Finally, we conclude in Section 5.5.

5.3 Materials and Methods

All chemicals were of analytical grade and were used without further purification. Gold(III) Chloride acid trihydrate ($HAuCl_4 \cdot 3H_2O$) (99.9%) and Asn (L-Asparagine) (98.0%) were purchased from Sigma-Aldrich. Sodium Hydroxide (NaOH, pastilles,

from Molar) was used to adjust the pH. The water used in all experiments was prepared using a Milli-Q Integral water purification system (EMD Millipore Direct -Q® 3UV-R) and had a resistivity of 18.2.

Sample Preparation

100 of 100 Asn solution was prepared and separated into two vials of 6 solution. Different ratios R = [NaOH]/[Asn] of 0.05 and 0.5, with an interval step of 0.05 were created to obtain a pH variation on each sample. The NaOH/Asn mixtures (pH-adjusted Asn solution) were left, in closed vials, under constant stirring for 3 hours at room temperature and under ambient conditions to reach pH equilibrium, as shown Figure 5.1. Then, 6 of the pH-adjusted Asn solution was added to 5 of a 1 fresh Gold(III) Chloride acid trihydrate ($HAuCl_4 \cdot 3H_2O$) solution at room temperature. The mixtures were immediately mixed and incubated at 80 for 40 using a hotplate. The samples were left to cool down at room temperature and without external cooling source. Subsequently, the set of samples were centrifuged at 1000 rpm, and the supernatant was extracted as the final product. Finally, we chose two pH, one more acid (pH 6) and one more basic (pH 9), for our studies.

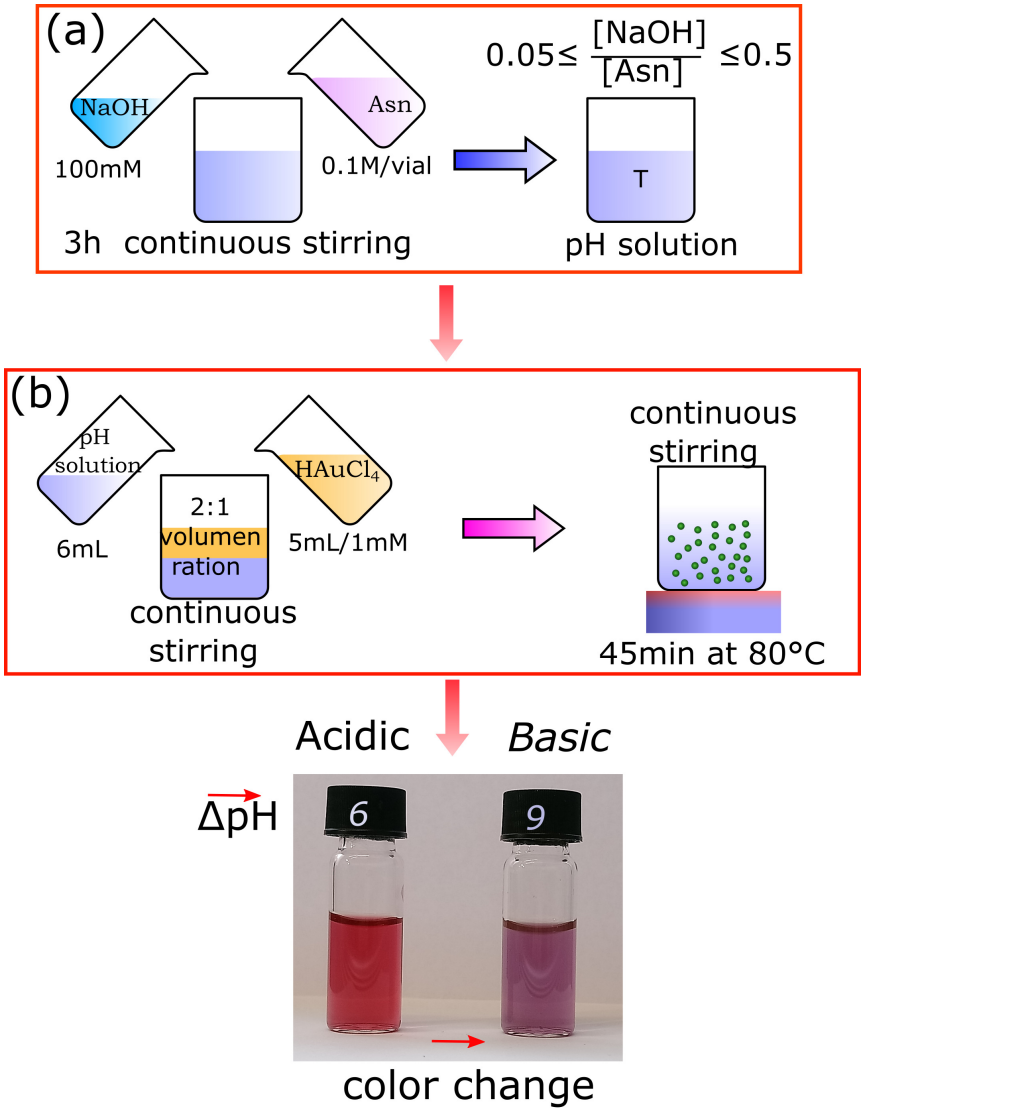

Figure 5.1: Schematic representation of AuNPs synthesized by Asn as a reducing agent. (a) In the first synthesis part, The Asn is first dissolved in water, and the Asn pH is controlled by a molar ratio of NaOH vs. Asn. (b) In the second synthesis part, Asn solutions are then mixed with $HAuCl_4$ in varying ratios. The photograph indicates the color difference between AuNP products synthesized at different pH. The acidic solution at pH 6 appears red to the eye while the more basic solution at pH 9 appears purple.

Characterization

Particle size, morphologies, and interplanar spacing in AuNPs were studied using a transmission electron microscope (TEM, JEOL JEM-2010) and high-resolution (HR)-TEM (Tecnai F20 microscope with FEI, acceleration voltage 200) respectively. Gatan Digital Micrograph software was used to analyse the HR-TEM micrographs. Particle distribution and population were determined by ImageJ software with standard plugins, included for ∼100 particles per sample. The polydispersity (P) was estimated as

$$P = \frac{\sigma}{s} 100\% \,, \tag{5.1}$$

with σ the standard deviation, σ = FWHM/2, FWHM the full width at half maximum of the total distribution, and s is the mean particle diameter (in nm).
The Crystallographic Toolbox (CrysTBox) software was used to interpret diffraction patterns obtained from HR-TEM micrographs [118]. The vibrational mode of Asn was characterised by Raman scattering. Raman spectra were acquired on a modular multi-channel Raman spectrograph Jobin Yvon–Spex 270M in 90 scattering geometry using a 532.15 line of a continuous-wave solid-state Nd-YAG laser for excitation, as described in Refs [119, 120]. The power at the sample was 240(Supplementary Figure 3 in the SI). Raman measurements were performed at room temperature-controlled hermetical quartz cell (2). Spectra were acquired with 5 accumulation time, 12 accumulations and 15 spectra per sample. Wavenumber scales were precisely calibrated (±0.1) using the emission spectra of a neon glow lamp taken before and after each Raman measurement. The Raman contribution from the water was subtracted, and the spectra were corrected for the non-Raman background.

5.3.1 Simulations

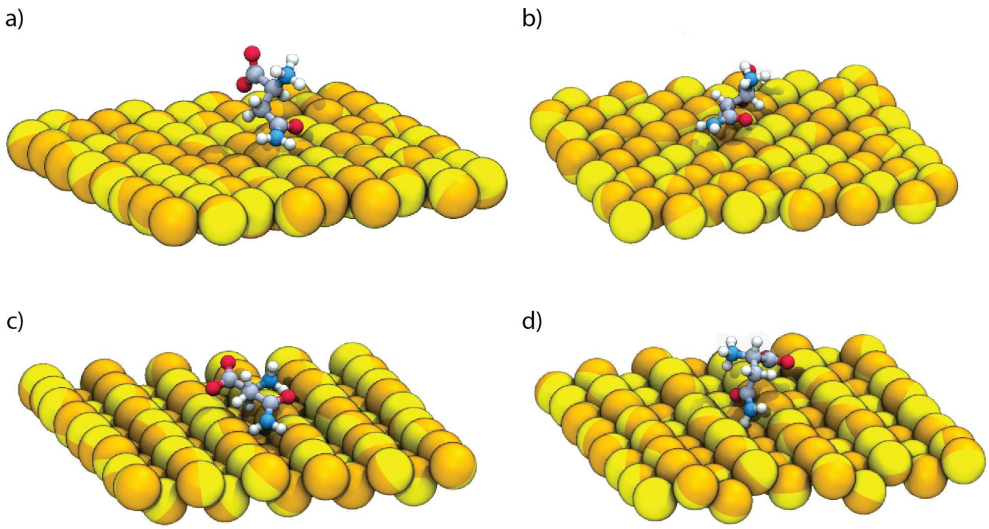

Figure 5.2: Simulation snapshots showing Asn on a) (111), b) (100) , c) (110), and d) (311) gold surfaces. For the sake of clarity, water molecules are not shown.

We investigate the adsorption of Asn on (111), (100), (110) and (311) gold surfaces (Figure 5.2) by first calculating the potential of mean force (PMF) resulting from pulling the amino acid away from the surface and towards the bulk water. Gold surfaces are oriented with normal vector parallel to the z-axis. Initially, we place the Asn as close as possible to the gold surface, at a distance of ∼0.3 nm. The simulation boxes were filled with TIP3P water molecules [121]. The centre of mass (COM) of Asn molecule was pulled out in the z direction and snapshots were collected each 0.1 nm in order to generate the starting configurations for the umbrella sampling calculation. For each window, 9 ns of molecular dynamics simulation were performed with the Asn centre of mass constrained using a harmonic potential with spring constant of 1000 kJ mol^{-1} nm^{-2}.

The PMF for each system was reconstructed using the weighted histogram analysis method (WHAM) [122]. All simulations were carried out with GROMACS 5.1.2 [123, 124], using CHARMM General Force Field for organic molecules [125, 126], for both Asn states, and a polarisable force field for gold [127] .

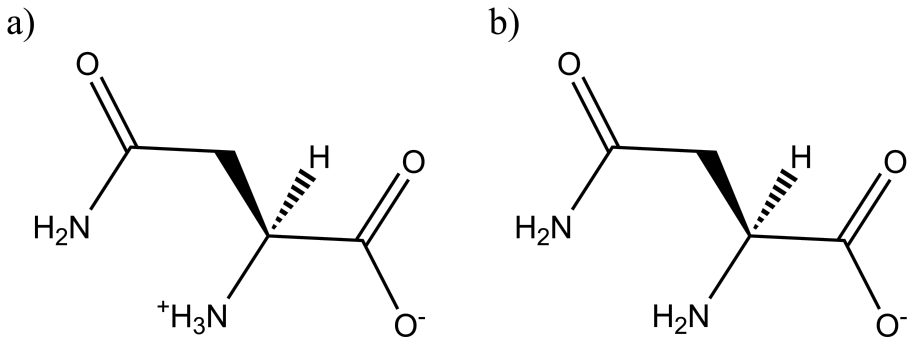

Figure 5.3: Schematic representation of Asn in the zwitterionic (major species at pH 6) (a) and anionic (major species at pH 9) (b) states.

In the experiment, different values of pH are associated to an excess in the concentration of zwitterionic (acidic, pH 6) or anionic (basic, pH 9) states of Asn. We use a major approximation to mimic these pH conditions by studying the adsorption of a single Asn molecule in two states: zwitterionic and anionic (Figure 5.3). To evaluate the adequacy of our approximation, we perform density functional theory simulations for a single Asn molecule in the two charge states and compute their corresponding Raman spectra (Supplementary Figure 4(a) in the SI). As expected, the spectrum of the anionic state exhibits suppressed resonances related to vibrations of the -NH_3^+ group. To a lesser degree, this effect is also apparent in the experimental Raman spectra of Asn in bulk solution at both pH conditions (Figure 5.5(a)). This correspondence suggests that the simplification of identifying molecular states with pH conditions might be useful to approximate and investigate the complex

experimental conditions, which are inaccessible to computer simulations that explicitly include all the chemical species present in the system.

5.4 Results and Discussion

5.4.1 Experiments

Morphological characterisation

TEM images (Figure 5.4) show AuNPs (at 200 nm resolution) obtained by reacting gold(III) ($HAuCl_4 \cdot 3H_2O$) with Asn at acidic (pH 6, Figure 5.4(a)) and basic (pH 9, Figure 5.4(b)) conditions. These images show that both reaction conditions yield non-spherical particles with increasingly amorphous shapes apparent at pH 9 (See also Figures 3 and 4 in the SI). The average particle size was determined by analyzing twenty TEM micrographs and a minimum of 56 particles per sample (Supplementary Figures S1 and S2 show a gallery of TEM micrographs used in the calculation of the particle size distribution), and using standard imaging protocols with the ImageJ software package. The results from the particle size analysis are given in the histograms depicted in Figure 5.4(c) (pH 6) and Figure 5.4(d) (pH 9). A Gaussian fit to the size distribution shows that the pH 6 reaction conditions yield particles of 18 $\pm$ 12 nm diameter, while the pH 9 reaction condition resulted in larger particles of 43 $\pm$ 27 nm diameter. The polydispersities for each sample set were similar, calculated as 67% for pH 6 and 64% for pH 9. These results indicate that, on average, the pH 6 particles are approximately 25 nm smaller in diameter than the pH 9 particles.

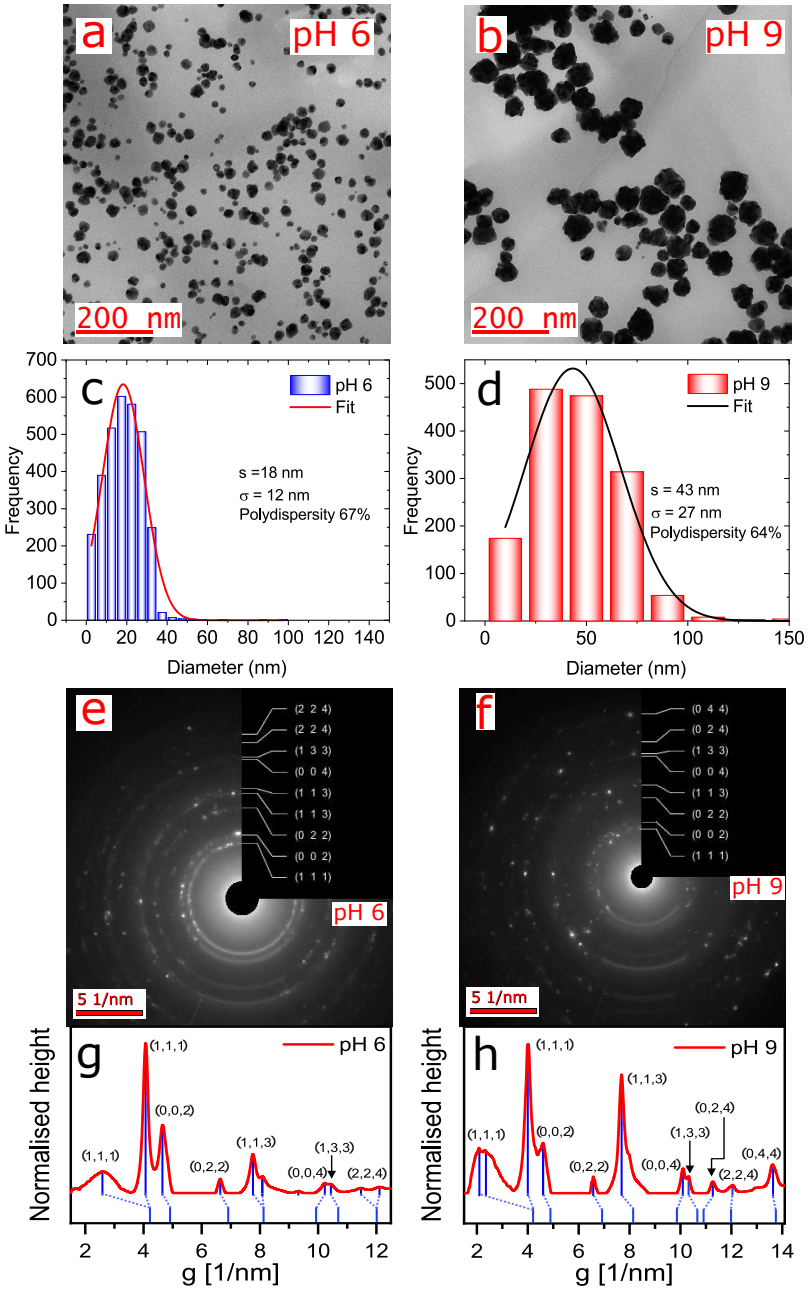

Figure 5.4: Morphological characterization with electron microscopy shows different size and shape distributions emerge when AuNPs are synthesized with Asn at pH 6 vs pH 9. (a) Electron microscopy image at 200nm of AuNPs at pH 6. (b) Electron microscopy image 200nm of AuNPs at pH 9. (c) Histogram of the gold nanoparticle size distribution at pH 6 with a frequency over 600 counts. (d) Histogram of the gold nanoparticle size distribution at pH 9 with a frequency over 550 counts. (e) electron diffraction pattern of AuNPs at pH 6. (f) electron diffraction pattern of AuNPs at pH 9.(g) electron diffraction profile of image (e) at pH 6. (h) electron diffraction profile of image (f) at pH 9. In both cases, the electron diffraction pattern showed the (111), (200), (220), and (311) reflections of gold in a typical fcc structure.

The electron diffraction pattern from the TEM measurements are shown in Figure 5.4(e-f), and the corresponding electron diffraction profiles of Figure 5.4(e-f) are shown in Figure 5.4(g-h) for pH 6 and 9 respectively. The primary diffraction peaks correspond to (111), (200), (220), and (311) reflections, which are characteristic of the gold fcc structure [128].The relative intensities of the diffraction peaks vary between the two sample sets, suggesting a difference in the particle shape.

The surface structure of the particles were further analyzed using high-resolution TEM (Supplementary Figure 4 and 5). For the pH 6 samples, two well-resolved (222)-type crystallographic planes were detected (measured D-spacing of about 1.16 Å and 1.14 Å, as shown in Supplementary Figure 3c), which run perpendicular to the sidewalls of the structure. The same process was used in the sample at pH 9, but in this case, was not apparent to identify crystalline orientations on the particle surface. Only one vertex selected shows (111)-type crystallographic planes (measured D-spacing of about 2.35 Å, as shown in Supplementary Figure 4c), which like the previous case run perpendicular to the sidewalls of the structure. The high-resolution TEM images at 10 nm showed differences in particle surface geometry between the two cases (Supplementary Figure 3(b) and Figure 4(b)). In the case of pH 6, it was possible to identify four triangular partitions on the particle surface with angles of 114.5, 87.3, 63.1, and 28.2 (Supplementary Figure 3(b)). In comparison, with the particles at pH 9, it was not possible to identify partitions on the particle surface. The pH 9 sample could not be similarly fit further indicating highly homogeneous surface structure.

The morphological characterization indicates that the pH 6 samples are on average smaller and more homogeneous in surface geometry than the pH 9 samples.

Earlier work in the literature has shown that when Asn is used as a reducing

agent to produce AuNPs, the size, color, and shape do not depend on the reactant concentrations [42]. Our results here demonstrate that when the reaction pH is used as a tuning parameter, it is possible to modify the critical properties of size, color, and shape.

Vibrational spectroscopic characterisation

Figure 5.5 shows the measured Raman spectra of the AuNPs, along with two solutions of Asn in water, at pH 6 and 9, for reference. Figure 5.5(a) shows the normalised Raman spectra of the reference solutions in the frequency region of 3001750, along with mode assignments. The mode $\nu(CO_2^-)$ shows the highest intensity for both solutions. In the frequency region of 7001000, the Asn solution at pH 9 shows a decrease in the intensity of the modes compared to the Asn solution at pH 6 (Figure 5.5(a)). Relevant shifts of the peaks in the spectra were not detected. Figure 5.5(b) shows a comparison of the normalised Raman spectra for the Asn solution in water at pH 6 and the AuNps/Asn sample at pH 6. The sample AuNps/Asn at pH 6 presents a peak at 400, which is associated to a torsion of -NH_3^+ group ($\tau(NH_3^+)$). The mode $\tau(NH_3^+)$ was not detected on the solution of Asn in water. In the region of 987 the stretching mode of ν(CC) underwent an increase in intensity compared to the spectrum of the solution of Asn in water. Figure 5.5(c) shows the comparison of the solution of Asn in water at pH 9 and the sample of AuNPs/Asn at pH 9. In this case, the spectrum of the AuNPs/Asn sample at pH 9 lacks the peak corresponding to the torsion mode of the -NH_2 group at 522. Figure 5.5(d) compares the Raman spectra of the samples AuNps/Asn at pH 6 and AuNps/Asn at pH 9. The main differences are the presence of the modes $\tau(NH_3^+)$ and ν(CC) in the sample AuNPs/Asn at pH 6 compared to the sample at pH 9, and a peak shift

towards higher energies in the region of 1125, associated with out-of-plane bending mode of $\gamma(NH_2)$ group for the sample with lower pH.

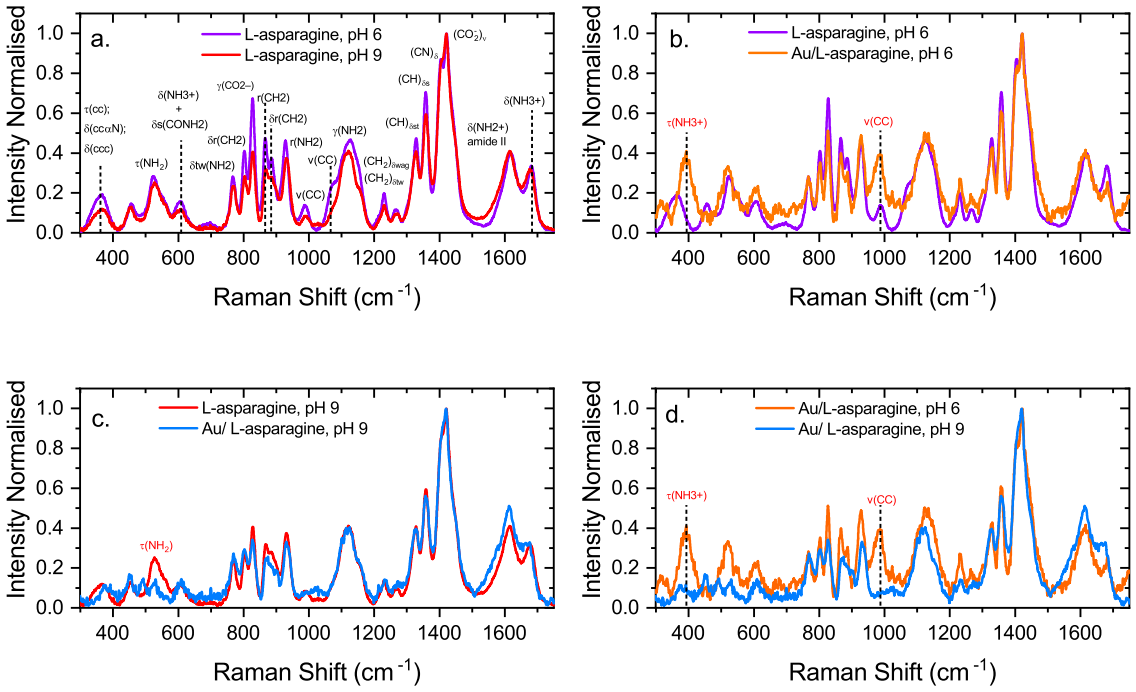

Figure 5.5: Experimental Raman spectra at pH 6 and 9 for the samples of AuNPs/Asn. (a) Raman spectrum of Asn at pH 6 and 9. (b) Raman spectra of Asn at pH 6AuNps/Asn at pH 6. (c) Raman spectra of Asn at pH 9 and AuNps/Asn at pH 9. (d) Raman spectra of AuNps/Asn at pH 6 and pH 9.

A summary of the assignment of the Raman peaks for Asn in the frequency region of 3001750 is shown in Table 5.1.

Table 5.1: Frequency modes of Asn and assignments in the region of [range-phrase=–,range-units=single]3001750. Abbreviations indicate: s = strong, m = medium, w = weak, v = very, sh = shoulder, sc = scissoring,r = rocking, wag = wagging, tw = twisting, ν = stretching, δ = bending, γ = out-of-plane bending, τ = torsion, s = symmetric, a = antisymmetric

Frequency ()	Assignments	Reference
364	δ(CCC);δ(CC$^{\alpha}$ N);τ(CC)	[129]
400	$\tau(NH_3^+)$	[130]
455		
522	$\tau(NH_2)$	[131]
608	$\delta(NH_3^+)$ + $\delta_s(CONH_2)$	[129]
700		
776		
802	$\delta_r(CH_2)$/ $\delta_{tw}(NH_2)$	[132–134]
825	$\gamma(CO_2^-)$	[129]
836	$\gamma(NH_2)$	[131]
865	$r(CH_2)$	[130]
884	$\delta_r(CH_2)$	[133]
928	$r(NH_2)$	[134]
987	ν(CC)	[132]
1077	ν(CN)	[129]
1125	$\gamma(NH_2)$	[129]
1231	$\delta_{tw}(CH_2)/\delta_{wag}(CH_2)$	[130]
1266	$w(CH_2)$	[130]
1329	δ(CH)	[134]
1357	δ(CH) δ_s(CH)	[132]
1404	δ(CN) AIII	[134]
1420	$\delta_s(CO_2^-)$/ $\delta_{sc}(CH_2)$	[130]
1617	$\delta(NH_2^+)$ amide II	[132]
1680	$\delta(NH_3^+)$	[134]
2129		
2940	$\nu u_s(CH_2)$	[131]
3195		
3233	water	[129]
3428	water	[129]

5.4.2 Simulations

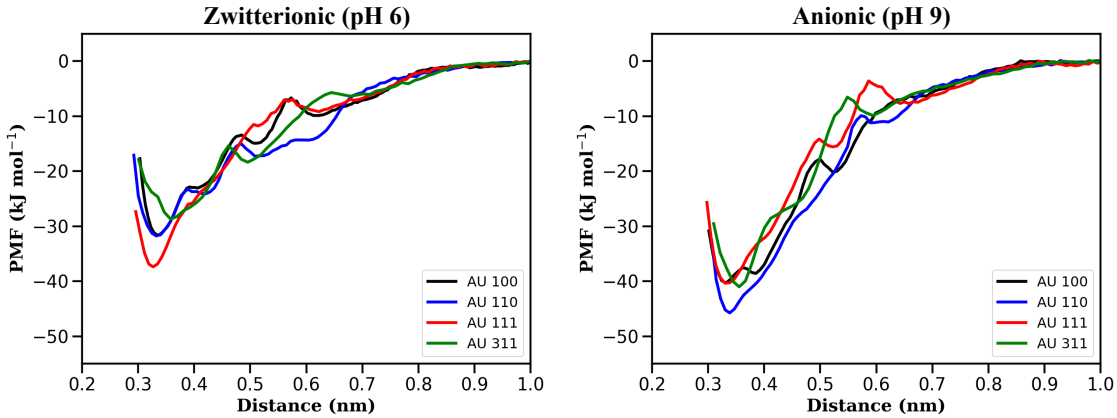

Figure 5.6: Potential of mean force obtained by pulling the centre of mass of Asn in zwitterionic (left) and anionic (right) states from (100)-, (110)-, (111)- and (311)-oriented gold surfaces. We identify the zwitterionic and anionic states with pH 6 and pH 9, respectively.

We investigate the adsorption mechanism of Asn on gold surfaces with orientations corresponding to the planes (111), (100), (110) and (311), which are those that most commonly appear in the experimental TEM spectra. We compute the potential of mean force to quantify the affinity of the Asn with these surfaces. In Figure 5.6 we present free energy profiles resulting from pulling Asn in the zwitterionic and anionic states which we associate to the two experimental conditions, namely pH 6 and pH 9, respectively. For all the considered surfaces, it is apparent that the anionic Asn tends to bind more strongly to the gold surfaces. It is also clear that close to the surface ($\sim$0.35 nm) the binding strength follows the trend (311) $<$ (110) $\sim$ (100) $<$ (111) for the zwitterionic Asn. For the anionic state, the trend changes to (111) $\sim$ (100) $\leq$ (311) $<$ (110), where the PMF for (111) gains 2.9 kJ mol^{-}1 upon increasing pH.

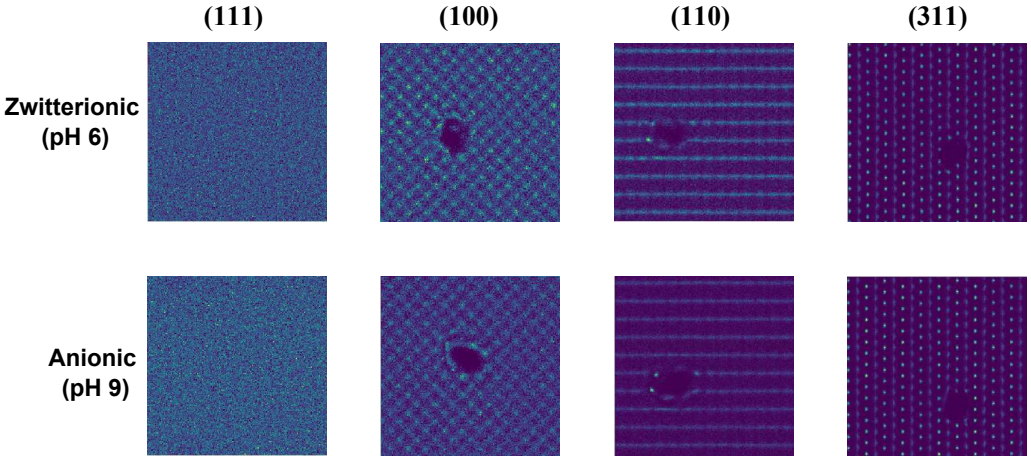

Figure 5.7: Projection, parallel to the surface, of the density of the oxygen atoms in water at a distance from the surface between 0.30;0.60. In all cases, the Asn is in the equilibrium position corresponding to the given surface (between 0.3;0.4).

To shed light on the specifics of the adsorption process, we first focus on the minimum distance between the Asn centre of mass and the surface. These distances are distributed between 0.3;0.4. In Figure 5.7 we show a projection of the density of the water oxygens, parallel to the surface, taken over a production run of 9, and at a distance between 0.30;0.60. The Asn centre of mass is constrained along the z-direction and is free to move on the surface. From Figure 5.7, the voids present for the two Asn states and the (100)-, (110)- and (311)-oriented surfaces indicate that the Asn remains pinned on the surface and it does not diffuse during the simulated timescale. By contrast, the amino acid freely diffuses on the (111)-oriented surface. As presented in Figure 5.8, this effect is the result of the water ordering occurring in close proximity to the gold surface, in close registry with the fcc lattice. For the (111) case, this ordering is only observed for the first water layer (at ~ 0.3). For the remaining surfaces, the effect is apparent up to distances between 0.6;0.9. Given the polar character of the Asn, it is not surprising that it forms a rather stable hydrogen

network with water molecules close to the gold surface. Furthermore, for (100), (110) and (311) surfaces where the water structuring grows into the bulk, the hydrogen network creates a pocket for the amino acid that hinders its surface diffusion. This picture remains essentially the same for the two Asn states considered here.

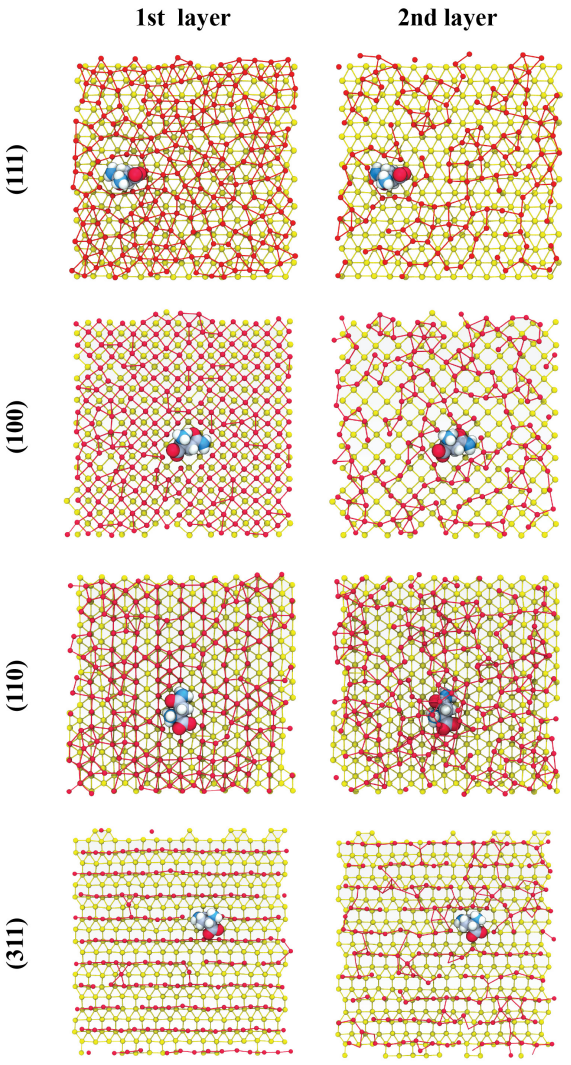

Figure 5.8: Simulation snapshot showing the top view of first and second layers of water oxygen and the zwitterionic Asn on a) (111), b) (100) , c) (110), and d) (311) gold surfaces. Key: Water oxygen atoms in red, gold atoms in yellow. Bonds were designated with a cutoff of 3.7.

The rather uniform (111) surface facilitates the adsorption of Asn as can be seen in the PMF results. The amino acid lies essentially flat thus maximising its contact area with the surface. Upon pulling away the amino acid, we observe that the resulting PMF is somewhat barrierless, indicating that Asn is uniformly detaching from the (111) surface. For the other surfaces, the various minima in the PMF are associated to tilting angles between the amino acid and the surface, formed during the detaching process.

When going from the zwitterionic to the anionic state, the -NH_3^+ group is replaced with a -NH_2 group. This change does not significantly modify the adsorption on the uniform (111) surface, as evidenced by the PMF (Figure 5.6). For the open surfaces, this change in the charge of the amino acid results in an increase in the amino acid/surface attraction due to the presence of two -NH_2 groups which bind more favourably to gold. Figure 5.9 shows the distribution of distances of the amide group (black line) and the ammonium/amine (blue line) for the surface orientations considered and when the centre of mass of the Asn is at $\sim$ 0.4 from the surface. The wide distribution without a clear preferential binding between the two groups is apparent for the (111) case. For the remaining surface orientations at acidic pH, it is clear that the amide group has the tendency to stay closer to the surface. At basic pH, both amine and amide groups are equally spaced from the surface. The complex distributions observed for the (110) case are the result of the tendency for Asn to align with the rows present on the surface.

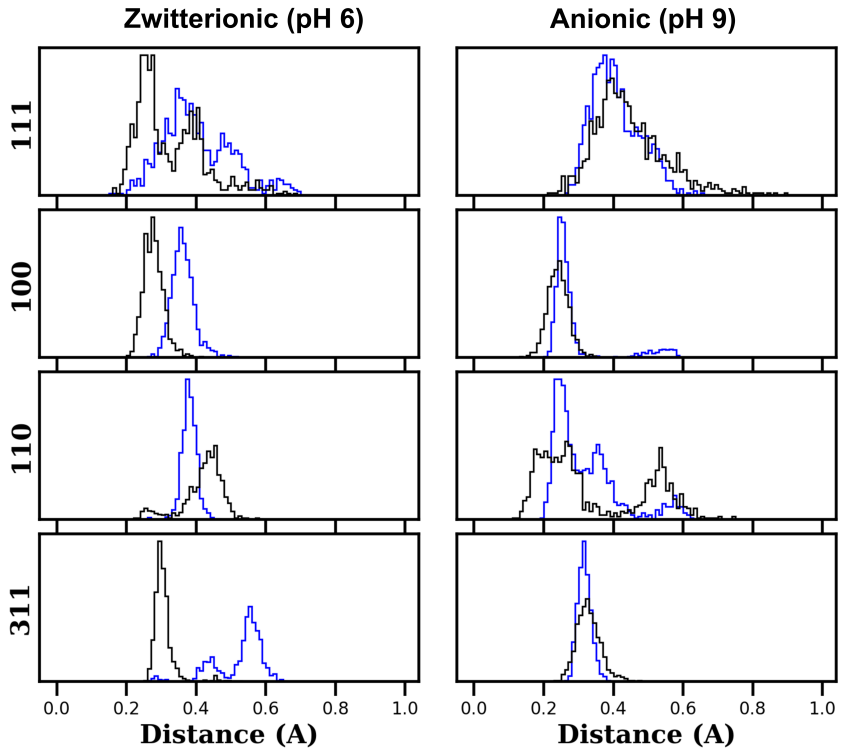

Figure 5.9: Distribution of distances of the ammonium/amine groups (blue lines) and amide group (black line) when the COM is constrained at ~ 0.4 from the surface

These observations allows the interpretation of the Raman spectra presented in Figure 5.5. At pH 6, panel (b), we observe that a peak at approximately 400 develops in the presence of AuNPs. This frequency corresponds to the $\tau(NH_3^+)$ mode. Upon adsorption, the amine group, -NH_2, binds to the surface while the ammonium group, -NH_3^+, is free to move and vibrates at its characteristic frequency, thus generating the peak in the spectra. At pH 9, panel (c), the amino acid is mostly present in its anionic form with the ammonium replaced by an amine group. As shown in the figure, the adsorption of these two -NH_2 groups on the gold surface suppress the corresponding $\tau(NH_2)$ mode at approximately 550.

The molecular orientation also provides a possible interpretation of the diffraction pattern and TEM measurements. The equilibrium shape of a metal NP corresponds to the minimum surface area configuration that minimises the surface Gibbs free energy. By combining extended Wulff construction [135] approaches with known values of surface energies, it is possible to determine the NP final equilibrium shape [136]. In the case of Au surfaces in vacuum, there is an approximately linear relation between surface energy, σ, and number of broken bonds per unit area [114]

$$\sigma \approx \gamma \frac{\sum_i^{N_s} n_i}{S}\,, \tag{5.2}$$

where γ is a constant in units of energy-per-atom, N_s the number of undercoordinated atoms per unit cell, n_i the number of Au broken bonds and S the area of the unit cell. Ab initio calculations predict that the product σS gives energies per atom equal to 55.6, 81.3 and 120.3 kJ mol^{-1} for (111), (100) and (110) Au surfaces, respectively [137]. Hence, the resulting AuNP equilibrium shape corresponds to a truncated octahedron exhibiting mostly (111) and (100) facets. The effect of including the interaction with a complex chemical environment is rationalised by considering a net overall decrease in Au surface energy and a deviation from the linear behaviour presented in Eq. (5.2) (with $\gamma \to 0$) [114]. This combined effect leads to the stabilisation of multi-faceted NPs [115].

The results in Figure 5.6 indicate that the adsorption of a single Asn helps reducing the energetic cost necessary for surface stabilisation by an amount between 28.7 and 45.8 kJ mol^{-1} (See Table 5.4.2). In the zwitterionic state (Figure 5.6 left panel), Asn interacts preferentially with the (111) surface with a free energy gain of 5.6 with respect to the (110) surface.

Table 5.2: Minimum energy values, and corresponding surface-Asn distances, of the PMF curves presented in Figure 5.6.

	Zwitterionic (pH 6)		Anionic (pH 9)	
Surface	E (kJ mol^{-1})	d (nm)	E (kJ mol^{-1})	d (nm)
111	-37.4	0.327	-40.3	0.330
100	-31.6	0.338	-40.3	0.332
110	-31.8	0.332	-45.8	0.339
311	-28.7	0.358	-41.0	0.355

This suggests that, upon Asn adsorption, the Au(111) facet is further stabilised with respect to the other facets, leading to rather isotropic AuNPs whose shape resembles the truncated octahedrons extensively discussed in the literature [138]. This prediction is consistent with HR-TEM and electron diffraction measurements shown in Figure 5.4(e-f).

For the anionic state (Figure 5.6 right panel), the main difference with the previous case is a general increase in Asn adsorption energy showing a reversal in the stabilisation sequence (See Table 5.4.2). In this case the amino acid is more strongly bound to the (110) surface (5.5 with respect to (111)). In the context of Eq. (5.2), these conditions correspond to an overall stabilisation of Au surfaces, with an additional decrease in surface energy differences between closed and open facets. As a result, open facets are more likely to appear, which agrees with scattering data showing higher population of (311) facets for basic than for acidic pH conditions (Figure 5.4(g-h)). This could also qualitatively explain the HR-TEM micrographs at pH 9 showing relatively amorphous AuNPs (Figure 5.4(b) and Figure 2 in the SI). We emphasise here that the interaction with anionic Asn induces global stability and near degeneracy of Au surfaces leading to changes in morphology and size of the resulting NPs. Indeed, stabilisation of more open surfaces could also be the reason

why we observe larger NPs at pH 9 (Figure 5.4(d)). Stable open surfaces occupy larger surface areas that grow with the radius (square) of the NP.

5.5 Conclusions

The use of biomolecules to synthesise AuNPs combines functionality with maximum biocompatibility. The complexity of the system and the large number of experimental degrees of freedom requires the combination of simplified yet relevant computational models and controlled experimental conditions. With this aim, we use a single amino acid, Asn, to synthesise AuNPs in aqueous solution with controlled pH. We show that the resulting size, and to some extent the morphology of the AuNPs, depends on pH.

A combination of Raman scattering and molecular dynamics simulations of the adsorption of zwitterionic and anionic Asn on (111)-, (100)-, (110)- and (311)-oriented gold surfaces unveils a unique adsorption mechanism. Asn mainly binds to gold surfaces via its amide group. Thus, the anionic state, the most probable state at higher pH (9 in the experiments), exhibits stronger binding to gold surfaces than the zwitterionic states, typical at acidic pH. In the latter, Asn preferentially adsorbs on (111) whereas, in the former, Asn preferentially adsorbs on the more open (110) and (311) surfaces. We use an argument based on surface energy considerations to suggest that this difference in Asn adsorption qualitatively explains why the AuNPs obtained at pH 9 are larger and somewhat amorphous when compared to the ones obtained at pH 6.

Our simulation results also highlight the role of water monolayers, close to the gold surface, in the adsorption of Asn. Water molecules on open gold surfaces order following the gold fcc template. The water structuring creates traps for Asn that

prevent it from diffusing on the surface. The underlying mechanism deserves further examination; in particular, more simulations using amino acids with different water affinities would be beneficial to understand this caging effect.

Chapter 6

Tuning optical coupling and electron cooling in amino-acid functionalized gold nanoparticles

Title manuscript:

Tuning optical coupling and electron cooling in amino-acid functionalized gold nanoparticles

R Báez-Cruz, Charusheela Ramanan , Robinson Cortes-Huerto and Paul Blom.

Author Contribution.

Ricardo Báez-Cruz and **Charusheela Ramanan** designed the research. **Ricardo Báez-Cruz** synthesized the complex AuNP-Asn, performed all experiments, and analyzed the data under the direction of Charusheela Ramanan. **Charusheela Ramanan** conducted the Time-Resolved Absorption measurements. **Robinson Cortes** designed the modeling and carried out the modeling. **Ricardo Báez-Cruz** wrote the manuscript. **Paul Blom** and **Charusheela Ramanan** supervised the project.

6.1 Abstract

The use of amino acids as capping and reducing agents in the synthesis of metallic nanoparticles constitutes a promising framework to achieve desired functional properties with minimal toxicity. In this work, we use L-Asparagine (Asn) to synthesize gold nanoparticles (AuNPs) in an aqueous solution at controlled pH. Our results indicate that size, shape, and localized surface plasmon resonance (LSPR) characteristics strongly depend on the Asn pH values of pH 6 and 8. The particle size obtained for pH 6 is 18±9 nm, while the particle size for pH 8 is 86±25 nm. The electron cooling dynamics of the LSPR was examined by transient absorption spectroscopy (fs-TA), and the results show that the pH 8 sample exhibits slightly slower electron cooling. We discuss these results in the context of our earlier findings regarding the pH dependent amino acid binding at the Au surface. The LSPR stability and the high reproducibility of AuNPs-Asn structure suggest that AuNPs obtained can be a potential candidate for biocompatible applications with plasmonic structures, such as bioimaging.

6.2 Introduction

Since Faraday, who for the first time had shown a synthesis method to obtained aqueous dispersions of colloidal metal particles [10], gold nanoparticles (AuNPs) have frequently been synthesized via chemical reduction [139]. The interest in AuNPs synthesis has been largely due to the exceptional optical properties of AuNPs, such as the localized surface plasmon resonance (LSPR) effect [11], which is generated by collective excitations of the conduction electrons into AuNPs [140]. The LSPR conditions, as plasmon distribution [141], absorption [142], or extinction coefficient

[143] have a dependency over the chemical surface around AuNPs [144] and the shape-size properties of AuNPs [145]. Additionally, the LSPR can capture far-field radiation and concentrate it into subwavelength volume below the diffraction limit [65,146]. This has become the LSPR effect in a fundamental parameter in novel applications such as biosensing [147], photothermal cancer detection-therapy [148], drug delivery [149], or improved photovoltaic devices [150]. Although the LSPR can produce the strong effects explained above, such as near-fields that result in extreme-field enhancements [151], the LSPR effect has a finite lifetime [152]. In a sequential process, an external photon excites the LSPR into AuNPs, which subsequently decays to yield excited electron-hole pairs [146]. This effect is known as a nonradiative process [153] and the decay can be studied via fs-Transient Absorption (fs-TA) or two-photon photoemission spectroscopies [154]. Likewise, the LSPR can decay via a radiative process by emitting a photon [65, 155–157].

The nonradiative decay channel is being researched because of the large plasmon-induced field enhancement and, therefore, the capability to enhance light-harvesting of the collective plasmon excitations [156]. However, the applications related to nonradiative decay channels have been explored more due to the ease of generating hot carriers [65]. For example, the hot carriers created via the plasmon effect apply to efficient photodetectors with spectra responses higher than bandgap limitations. This is because hot carriers provide an efficient mechanism to convert light into electric current or even use alternative solar-energy harvesting devices [157]. Additionally, another importance of the nonradiative decay channel is that plasmon-induced hot carriers [65] can inject into graphene to enable plasmon-induced phase transitions

[158].

The LSPR lifetime decay is partitioned, as an effect of energy conservation, into consecutive dynamics processes, such as dephasing (10 fs time scale), electron-electron scattering (100 fs), electron-phonon coupling (1-5 ps), and heat dissipation processes (10-100 ps) [5]. Although the dynamics time scales are not exact, it is a useful starting point for discussing how size, shape, and the environment affect electron AuNPs dynamics [61].

These are the most critical parameters that must be controlled through synthesis via chemical reduction, which is sometimes turning a difficult goal. Therefore, this is why it is necessary to define a synthesis method that leads a controlled chemical surface, shape, and size particles easily.

In general, the chemical reduction protocols are based on using a gold source, e.g., Chloroauric Acid ($HAuCl_4 \cdot 3H_2O$), in the presence of reducing agents and suitable stabilizer agents [159]. In some cases, the stabilizer agent is an important parameter to define AuNPs shape [160], e.g., Cetyltrimethylammonium-bromide (CTAB) has been primarily used to obtained anisotropic AuNPs [99]. By contrast, organic molecules [161], serum albumin protein [162], or natural extract solutions [163] as both reducing and capping agents have been implemented to avoid the significant chemical release generated by the CTAB on the particle surface [164, 165]. Here, we have explored a chemical reduction method based on the amino acid L-Asparagine (Asn) as both a reducing and stabilizer agent by modulating its pH by adding small volumes of a stock solution of 100 mM sodium hydroxide (NaOH). This choice

is motivated by the acidic (pH 6) and basic (pH 8) environment resulting from a high zwitterionic and anionic Asn state concentration, respectively. The Asn-AuNP hybrid systems behave optically reproducibly like other AuNP systems and across different pHs. This offers exciting possibilities for applications in developing biohybrid systems or use for imaging biologically sensitive samples.

We investigate optical interactions and electronic transition processes of the ground and excited states into AuNPs over these two chemical forms when they are photoexcited by 400 nm pumping at different delay times (0 ps -100ps) via fs-TA.

The chapter is organized as follows: In Section 6.3 we describe the synthesis procedure, and characterization techniques. We present the experimental results in Section 6.4. In Section 6.5 we present the discussion related to Section 6.4. Finally, we conclude in Section 6.6.

6.3 Materials and Methods

All chemicals were analytical grade and used without further purification. Gold(III) Chloride acid trihydrate ($HAuCl_4 \cdot 3H_2O$) (99.9%) and L-Asn (L-Asparagine) (98%) were purchased from Sigma-Aldrich and sodium hydroxide (NaOH, pastilles) from Molar. The water used in all experiments was prepared using a Milli-Q Integral water purification system (EMD Millipore Direct -Q® 3UV-R) and had a resistivity of 18.2 MΩ cm.

6.3.1 Synthesis of L-Asn/AuNPs

A stock solution of 100 mM L-Asn solution was prepared and separated into four vials of 6 mL solution. The pH of each sample was turned by adding different ratios R=[NaOH]/[L-Asn] of values equal to 0, 0.05, and 0.1, yielding pH values of 3, 6, and

8, respectively. These L-Asn/NaOH mixtures (pH-adjusted L-Asn solution) were left stirring for three hours at room temperature to reach pH equilibrium (Figure 6.1). Afterward, 6 mL of the pH-adjusted L-Asn solution was added to 5 mL of a 1 mM fresh gold (III) chloride acid trihydrate ($HAuCl_4 \cdot 3H_2O$) (99.9%) solution at room temperature. The mixtures were heated to $80°C$ for 45 minutes with stirring. Color change in the reaction mixture indicated successful synthesis of AuNPs at all three pH values. The mixtures were removed from the hotplate and left to cool to room temperature slowly. After cooling, the mixtures were centrifuged at 1000 rpm for 10 min, and the resulting supernatant was extracted as the final product (photograph Figure 6.1).

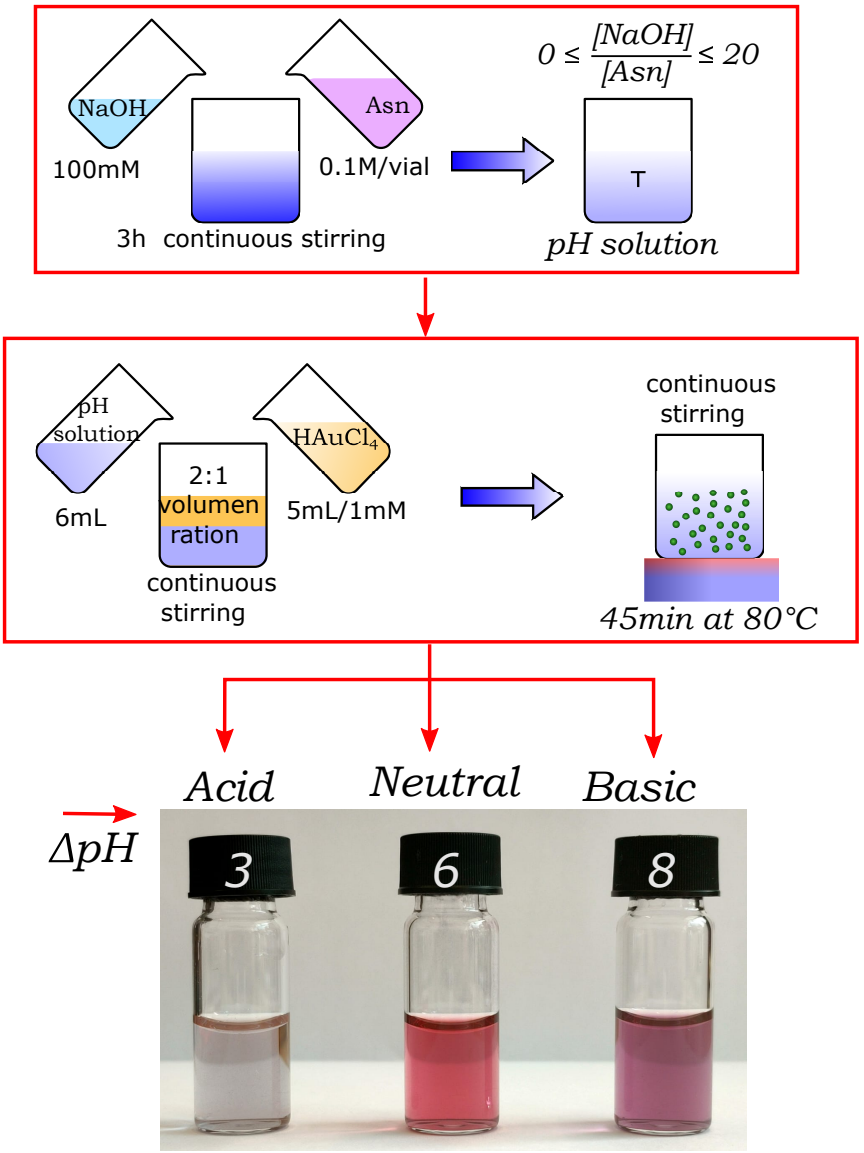

Figure 6.1: Schematic representation of AuNPs synthesized by Asn as both reducing and stabilizing agent. In the first part of the synthesis, the Asn is dissolved in water, and sequentially pH Asn solution is controlled by adding NaOH solution to create a different molar ratio of NaOH vs. Asn. In the second part of the synthesis, the Asn solution is mixed with a solution of $HAuCl_4$. Finally, in the lower panel, the photograph shows the AuNPs obtained at pH 3, 6, and 8.

6.3.2 Structural Characterization

Particle size, morphologies, and interplanar spacing in AuNPs were studied using a transmission electron microscope (TEM, JEOL JEM-2010) and high-resolution (HR)-TEM (Tecnai F20 with FEI, acceleration voltage 200kV). Gatan Digital-Micrograph software was used to analyze the HR-TEM micrographs. Particle distribution and population were determined by ImageJ software with standard plugins, included for 100 particles per sample. CrysTBox software was used for studying diffraction patterns obtained from the HR-TEM micrographs [118].

6.3.3 Spectroscopic Characterization

Steady-state absorption was measured on a Perkin-Elmer Lambda400 spectrophotometer. The fs-Transient absorption (fs-TA) measurement was carried out on a Helios Fire pump-probe setup from Ultrafast Systems, paired with a regeneratively amplified 1030 nm laser (Light conversion, Pharos, 200 fs). An optical parametric amplifier (Orpheus-F, Light Conversion) was used to generate the pump pulse. The effective laser repetition rate of 1 kHz was set with an internal pulse picker. The photoexcitation (pump) wavelength was 400 nm, with energy fluence on the sample of 32 μJcm^{-2}. The broadband probe light ($320650nm$) was generated by focusing a portion of the 1030 nm fundamental on a rotating CaF_2 plate. Surface Xplorer Software (Ultrafast Systems) was used to analyze the raw data. Global analysis of the transient absorption data was performed using the R-package TIMP software 2.0 with the graphical interface Glotaran [166, 167].

6.4 Results

6.4.1 Shape and size properties of AuNPs

TEM images (Figure 6.2) show AuNPs obtained by reacting gold(III) (HAuCl4) with Asn at acidic (pH 3-Figure 6.2a), neutral (pH 6-Figure 6.2b), and basic (pH 8-Figure2c) conditions. The average particle size was determined by analyzing twenty TEM micrographs and a minimum of 56 particles per sample using standard imaging protocols with the ImageJ software package. The results from the particle size analysis are given in the histograms depicted in Figure 6.2d (pH 3), Figure 6.2e (pH 6), and Figure 6.2f (pH 8), along with Gaussian fits to quantify the size distribution. The average particle size and polydispersity vary with the reaction pH. The pH 3 reaction conditions yield particles of $67 \pm 18nm$ diameter (PDI = 27%), the pH 6 reaction yields smaller particles of $18 \pm 9nm$ diameter (PDI = 48%), and the pH 8 reaction resulted in larger particles of $86 \pm 25nm$ diameter (PDI = 29%). These results indicate that, on average, the pH 6 reaction yields the smallest diameter particles, the pH 3 reaction gives intermediate size, and the pH 8 reaction gives the largest diameter particles. TEM images of the synthesized particles at 50 nm resolution show that the varying pH also yield particles of different shapes (Figure 6.2g-i).

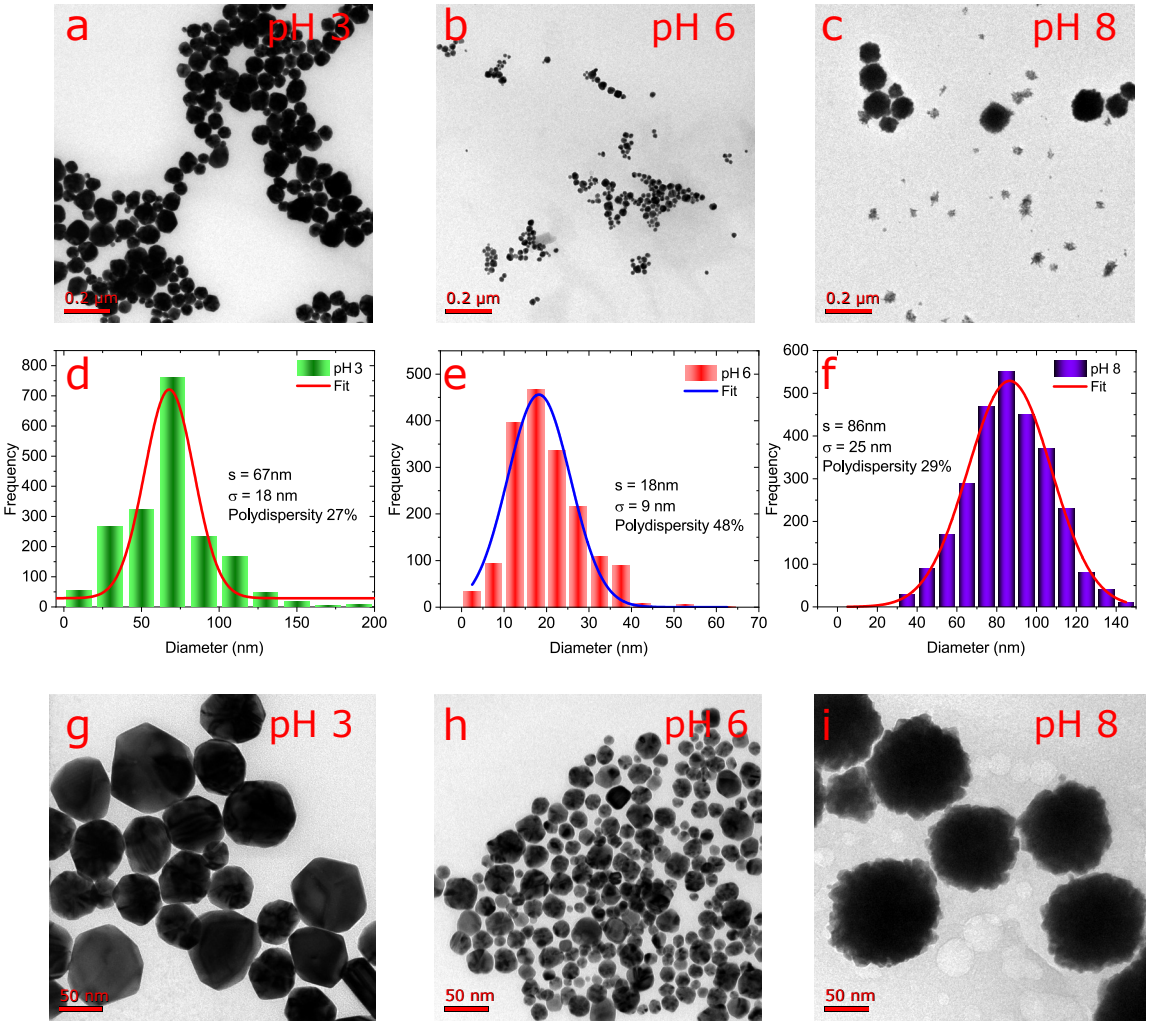

Figure 6.2: Morphological characterization using electron microscopy shows different size and shape distributions emerge when Asn synthesizes AuNPs at pH 3, pH 6, and pH 8. (a-b-c) Electron microscopy image at 0.2 um of AuNPs at pH 3, pH 6, and pH 8, respectively. (d-e-f) Histogram of the AuNPs size distribution at pH 3, pH 6, and pH 8. The frequency is set over 800, 500, and 600 counts, respectively. (g-h-i) Electron microscopy image at 50 nm of AuNPs at pH 3, pH 6, and pH 8, respectively. In this case, the varying particle shape and surface morphology for each pH value can be seen.

6.4.2 Plasmonic absorption band from steady-state absorption

The transmission absorption spectra of the AuNP mixtures in water are shown in Figure 6.3. All three samples show a pronounced absorption peak between 500-600 nm. This agrees with literature reports for the localized surface plasmon resonance (LSPR) band in AuNPs of this size range [11, 168]. The AuNPs at pH 3 shows an absorption feature centered at 555 nm. The absorption peak for the sample at pH 6 is localized at 526 nm. This relative 29 nm blueshift and also peak narrowing is consistent with the smaller size distribution of the pH 6 sample. The absorption feature at pH 8 is centered at 581 nm. The 26 nm redshift of the pH 8 sample relative to pH 3 is also consistent with the larger average particle size.

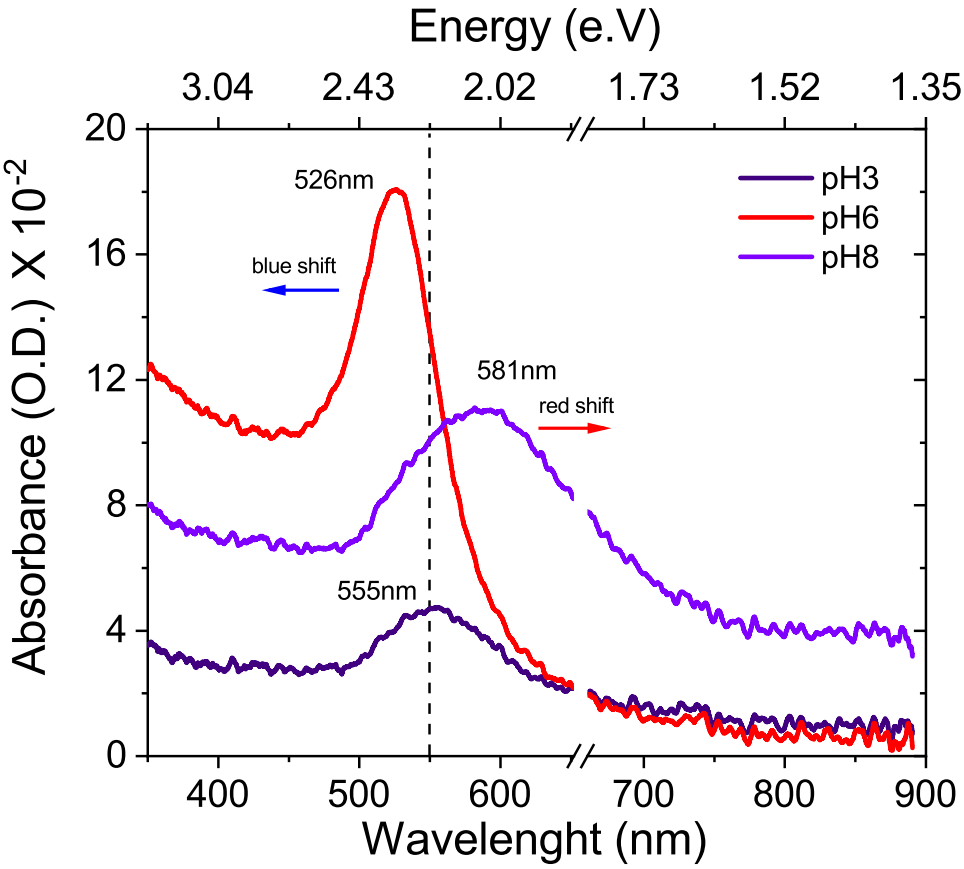

Figure 6.3: Transmission absorption spectra of AuNPs synthesized at pH 3, 6, and 8. The sample at pH 6 shows an optical absorption feature at 526 nm, and the absorption feature at pH 8 is localized at 581nm. Sample at pH 6 yields a blueshift over 29 nm concerning the pH 3 sample, and pH 8 yields a redshift over 26 nm relative to the pH 3 sample.

6.4.3 pH-dependent electron cooling dynamics

Figure 6.4 shows the fs-transient absorption (TA) spectra of the pH 6 and pH 8 sample, photoexcited at $\lambda_{ex} = 400nm$. The color scale variation represents a series of time delays after photoexcitation of -511 fs to 94 ps. Three features are present in the TA spectral profile. Immediately after the excitation, a negative feature around

525 nm is observed for pH 6, and 530 nm for pH 8 is seen. This is attributed to the "bleaching" of the plasmon band [6, 7].

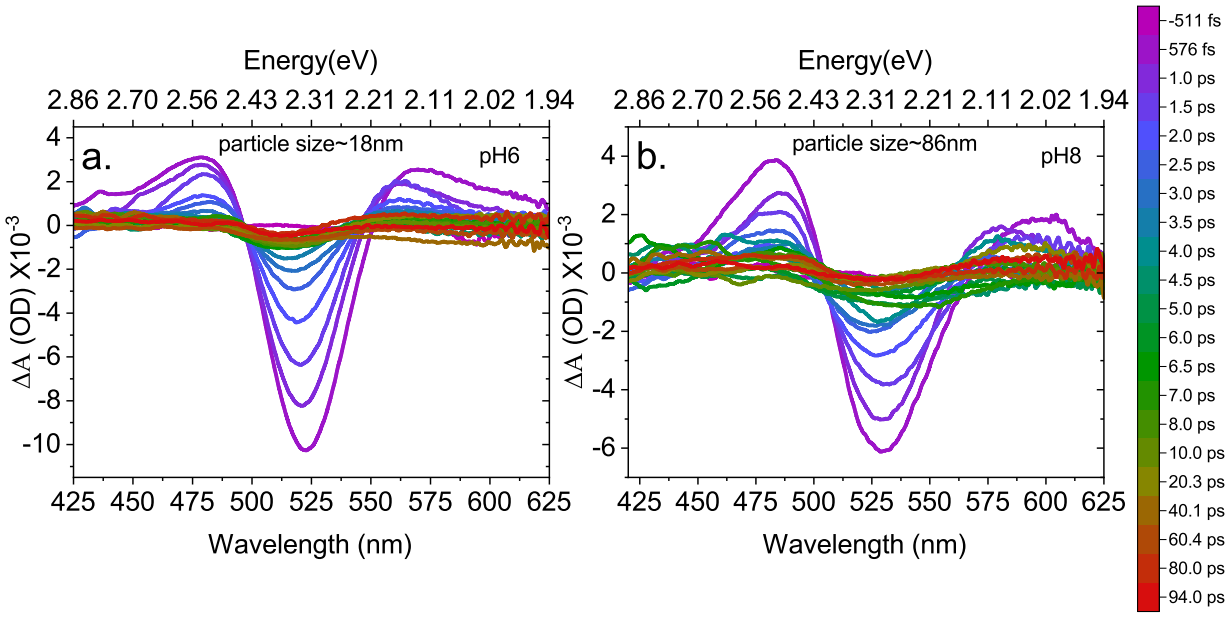

Figure 6.4: fs-Transient Absorption (TA) spectra of the pH 6 and 8 samples, photoexcited at $\lambda_{ex} = 400nm$. The color scale variation represents a series of time delays after photoexcitation of -511 fs to 94 ps.

Additionally, two positive features are present in the TA spectra on either side of the bleaching band. These are associated with broadening the LSPR at higher electronic temperatures (transient absorption plasmon bands). [169] These give rise to interband transitions, from the d band to above the Fermi level, where the threshold energy in AuNPs to generate interband transitions is 2.4 eV [6, 170, 171]. Photoexcitation above 2.4 eV induces a heating process in the electron gas [172].

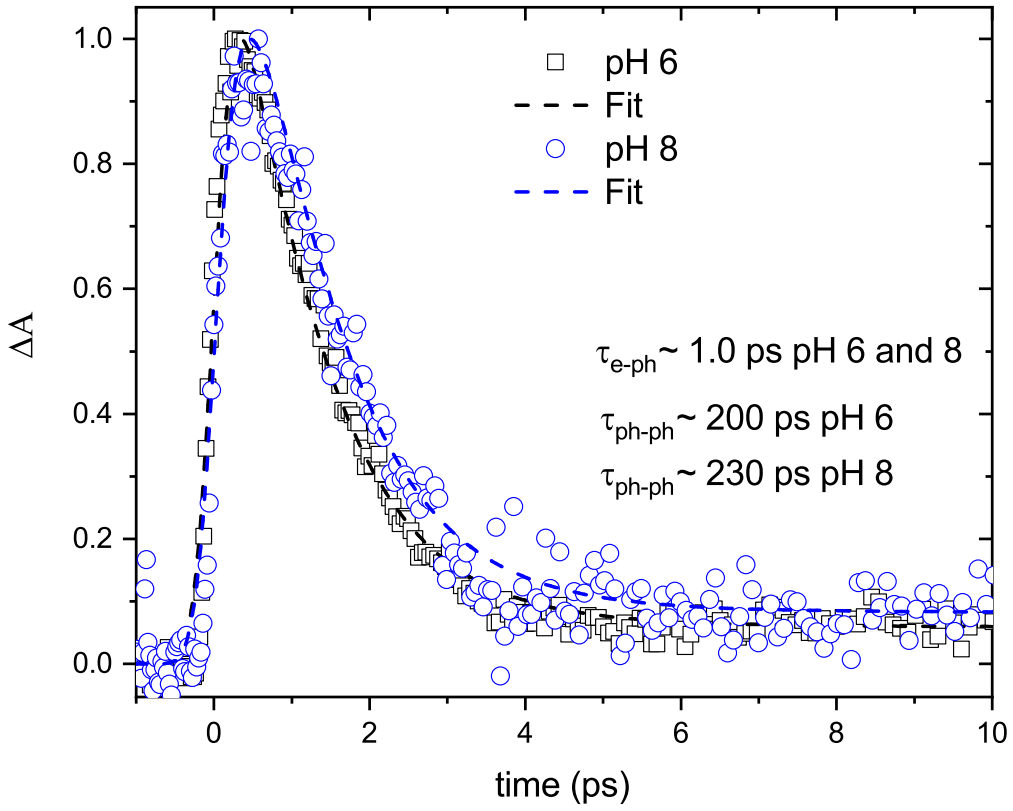

Figure 6.5: A Compares kinetic decay profiles for pH 6 and pH 8 conditions at 525 nm. The dashed lines represent the fit. The electron-phonon coupling process (τ_{e-ph}) occurs between at 1.0 ps, and the phonon-phonon coupling process (τ_{ph-ph}) occurs between 200 ps.

Figure 6.5 shows a comparison of kinetic decay of the bleaching for pH 6 and 8. The bleaching decay is faster for pH 6 than pH 8.

6.5 Discussion

Upon photoexcitation of the AuNPs, the plasmon lifetime is divided into three processes, which decay due to sequenced effects of energy dissipation [61]. After the photon absorption, the particle undergoes the following process:

1. The creation of coherence and thermalization plasmons. In this stage, the hot electrons lose coherence and energy by scattering with other electrons (electron-electron scattering) [5]. This occurs on a timescale of hundreds of femtoseconds.

2. The hot electrons, at the Fermi level, have equilibrated and created a hot electron bath at the same temperature. In this case, the hot electrons cool by mutual inelastic interaction with the phonons and vibrational modes, which heat the gold lattice (electron-phonon scattering) [152]. This process occurs around 1-10 picoseconds.

3. The gold lattice reaches a hot lattice condition and the resulting hot phonons thermally equilibrate with the solvent. The lifetime of this interaction occurs on the order of hundreds of picoseconds [60].

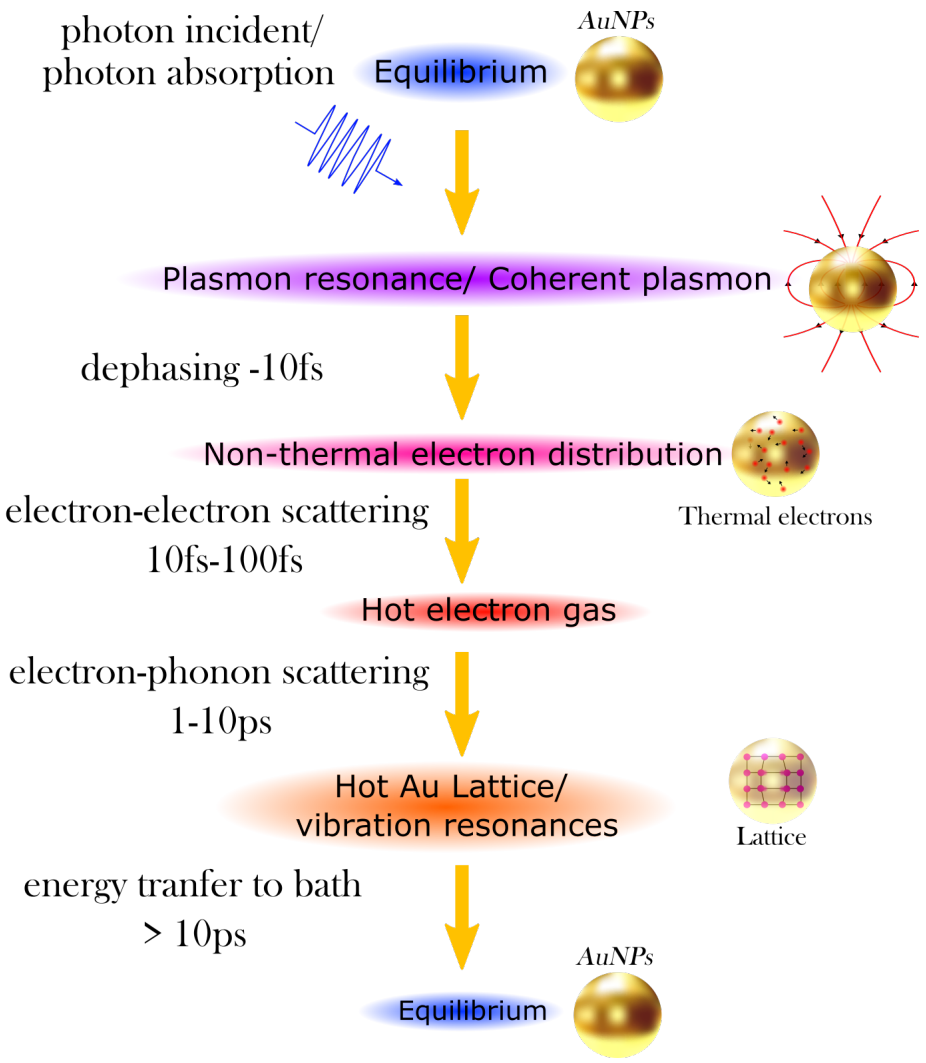

Figure 6.6: Diagram of lifetime plasmon. A sequence of lifetime plasmon and approximate time scales. Graphic inspired by [5]

Figure 6.4 shows TA spectra features at pH 6 and 8 obtained after a delay of about 0.6 ps photoexcited at 400 nm. The positive spectra feature of about 480 nm (pH 6 and 8) represents the modulation of interband transitions around the threshold point in the energy region where the excitation from the d-band to the sp-conduction band produced electron-hole pairs [173]. The negative spectral feature (Figure 6.4

a-b) resulted from the bleaching of the optical extinction by AuNPs intrinsic plasmon (IP) [6,7,173]. A second positive feature is shown in Figure 6.4 a-b, named interband-excitation-induced plasmon (EIP). With increasing time delay, there is a blue shift of the EIP feature, creating a shift in the crossing point of the spectrum through the zero TA line. This mechanism shows that the EIP feature can be established as a localized surface plasmon resonance (LSPR) spectrum feature [6,173] (578 nm by pH 6 and 530 nm by pH 8). Additionally, the EIP feature's blueshift coincides with an apparent redshift in the IP-band [173,174] (Figure 6.4).

After 10 ps, the EIP-relaxation band is a little larger in amplitude for both pHs. This is associated with the diffusion of the excess energies of the interband-excitation induced holes in the d-band and the hot electrons to the lattices, enhancing the electron-phonon interaction process, as suggested by [173]. Additionally, The excess energy produced by the interband-transitions is transferred to the lattice [173].

The electron-phonon coupling process (τ_{e-ph}) takes place between 1.0 to 10 ps and is related to the hot electron cooling [152,175]. For the majority of cases, the electron-phonon coupling is estimated as constant strength interaction [176]. The kinetic profile for 525 nm shows bleaching band decay rate is about 1.0 ps (Figure 6.5), consistent with the decay values expected for an electron-phonon coupling process [61,177].

The phonon-phonon coupling process (τ_{ph-ph}) takes place between 10 to 200 ps [60]. The bleaching band decay shows a τ_{ph-ph} of about 200 ps for pH 6 and 230 ps or pH 8 (Figure 6.5), consistent with the long-lived thermal effect on the gold lattices by phonon-phonon interaction process (τ_{ph-ph}) [6, 173, 175]. Therefore, the time variation for electron-phonon and phonon-phonon coupling, showed above, could suggest a resonant coupling at higher electronic temperature [169,178].

The bleaching decay is faster for pH 6 than for pH 8 (Figure 6.5). The relaxation dynamics delay between pH 6 and 8, in this case, could be associated with two variables. First, the electron-phonon coupling depends on the particle size, and the scattering grain boundaries induce a plasmon damping accelerated for monocrystalline and polycrystalline AuNPs, respectively [179]. And second, the chemical nature of the Au surface causes a difference in the electron oscillation relaxation dynamics in the particle [180,181]. Previous work has shown that changes in ligand chemistry can impact electron cooling dynamics [60], which could also be occurring in our system. In this case, our own previous Raman spectroscopy experiments showed that Asn amino acid binds to gold surfaces via its amide group [182]. The anionic state exhibits stronger binding to gold surfaces than the zwitterionic state, i.e., at pH 6 the Asn binds via only one amide group, whereas at pH 8, both amide group coordinate. The change in the Asn coupling to the Au surface relative to the pH state could therefore influence the electron cooling in the AuNP-Asn complexes (Figure 6.5).

The excitation energy required to create an interband transition above the threshold is 2.4 eV for AuNPs [170], e.g., an electronic transition from 5d-band to 6sp-band, making interband transitions considerably more unlikely than intraband transitions [170,171]. The absorption and bleaching process shown in Figure 6.4 can be associated with the expansion of hot particles, hence the decrease in the plasmon frequency [183]. That condition can cause a redshift of the plasmon band [6], as shown in the TA spectra (Figure 6.4). As the hot electrons cool, the bleaching band blue-shifts due to reduced broadening [6, 184].

6.6 Conclusions

We use the amino acid (Asn) to synthesize AuNPs in an aqueous solution with controlled pH, following our previous synthesic route [182]. The TEM results showed that the resulting size, and to some extent the morphology of the AuNPs, depends on pH. Additionally, this indicates that this synthetic route is a stable mechanism to synthesize AuNPs using Asn as a reduction and stabilization agent to conjugate particles exclusively with Asn. The AuNPs optical activity showed that the steady-state absorption coupling for AuNPs has localized into the optical region (530-600 nm) as we expected. According to the pH value and the resulting change in particle size, the LSPR absorption shifts. The AuNPs with pH 6 and pH 8 showed blueshift and redshift, respectively.

The fs-TA spectra shows two positive features. The positive spectra feature of about 480 nm represents the modulation of interband transitions where the excitations from the d-band to the sp-conduction-band produced electron-hole pairs. The positive feature over 578 nm is the interband-excitation-induced plasmon (EIP), and the negative feature (525 nm) is associated with the bleaching of the optical extinction by AuNP intrinsic plasmon (IP). The kinetic profiles are fit with biexponential decays. Both samples showed a fast decay of 1 ps for both pH values, which is associated with the electron-electron interaction (τ_{e-ph}). The slower decays are 200 ps for pH 6 and 230 ps for pH 8, and are related to electron-phonon coupling (τ_{e-ph}). While these fit values are very close, the comparison of kinetic decay profiles (Figure 6.5) indicates that there is a slower decay process in pH 8. This leads us to consider that the pH condition could influence the electron cooling process, which could originate from a change in vibrational coupling to the Asn ligands [182].

The results indicate that the Asn-AuNPs are stable nanomaterials at various physologically relevant pH values, and their properties can further be tuned by pH. We have found that our Asn-AuNP hybrid systems behave optically reproducibly like other AuNP systems and across different pHs. This offers exciting possibilities for applications in developing biohybrid systems or use for imaging biologically sensitive samples.

Bibliography

[1] E. González, J. Arbiol, and V. F. Puntes, "Carving at the nanoscale: sequential galvanic exchange and kirkendall growth at room temperature," *Science*, vol. 334, no. 6061, pp. 1377–1380, 2011.

[2] E. González and V. Puntes, *Un viaje al interior de la materia: arquitectura del nanocosmos : diseño y construcción del tamaño, la composición y la forma*. Centro de Ciencias y Tecnología Nanoescalar, 2013.

[3] J. Turkevich, P. C. Stevenson, and J. Hillier, "A study of the nucleation and growth processes in the synthesis of colloidal gold," *Discussions of the Faraday Society*, vol. 11, pp. 55–75, 1951.

[4] M. A. García, "Surface plasmons in metallic nanoparticles: fundamentals and applications," *Journal of Physics D: Applied Physics*, vol. 44, no. 28, p. 283001, 2011.

[5] K. O. Aruda, M. Tagliazucchi, C. M. Sweeney, D. C. Hannah, and E. A. Weiss, "The role of interfacial charge transfer-type interactions in the decay of plasmon excitations in metal nanoparticles," *Physical Chemistry Chemical Physics*, vol. 15, no. 20, pp. 7441–7449, 2013.

[6] S. Link and M. A. El-Sayed, "Shape and size dependence of radiative, non-radiative and photothermal properties of gold nanocrystals," *International reviews in physical chemistry*, vol. 19, no. 3, pp. 409–453, 2000.

[7] A. Crut, P. Maioli, N. Del Fatti, and F. Vallée, "Optical absorption and scattering spectroscopies of single nano-objects," *Chemical Society Reviews*, vol. 43, no. 11, pp. 3921–3956, 2014.

[8] M. Pålsson, "Raman spectroscopy and confocal raman imaging," *Lund Reports in Atomic Physics*, 2003.

[9] R. Pérez Pueyo, *Procesado y optimización de espectros Raman mediante técnicas de lógica difusa: aplicación a la identificación de materiales pictóricos.* Universitat Politècnica de Catalunya, 2005.

[10] M. Faraday, "X. the bakerian lecture.—experimental relations of gold (and other metals) to light," *Philosophical Transactions of the Royal Society of London*, no. 147, pp. 145–181, 1857.

[11] V. Amendola, R. Pilot, M. Frasconi, O. M. Marago, and M. A. Iatì, "Surface plasmon resonance in gold nanoparticles: a review," *Journal of Physics: Condensed Matter*, vol. 29, no. 20, p. 203002, 2017.

[12] S. M. Bhagyaraj and O. S. Oluwafemi, "Nanotechnology: the science of the invisible," in *Synthesis of inorganic nanomaterials*, pp. 1–18, Elsevier, 2018.

[13] M. Loos, *Carbon nanotube reinforced composites: CNT Polymer Science and Technology.* Elsevier, 2014.

[14] D. J. Barber and I. C. Freestone, "An investigation of the origin of the colour of the lycurgus cup by analytical transmission electron microscopy," *Archaeometry*, vol. 32, no. 1, pp. 33–45, 1990.

[15] F. Wagner, S. Haslbeck, L. Stievano, S. Calogero, Q. Pankhurst, and K.-P. Martinek, "Before striking gold in gold-ruby glass," *Nature*, vol. 407, no. 6805, pp. 691–692, 2000.

[16] B. H. Kim, J. Heo, S. Kim, C. F. Reboul, H. Chun, D. Kang, H. Bae, H. Hyun, J. Lim, H. Lee, *et al.*, "Critical differences in 3d atomic structure of individual ligand-protected nanocrystals in solution," *Science*, vol. 368, no. 6486, pp. 60–67, 2020.

[17] J.-K. Qin, P.-Y. Liao, M. Si, S. Gao, G. Qiu, J. Jian, Q. Wang, S.-Q. Zhang, S. Huang, A. Charnas, *et al.*, "Raman response and transport properties of tellurium atomic chains encapsulated in nanotubes," *Nature Electronics*, vol. 3, no. 3, pp. 141–147, 2020.

[18] J.-F. Li, Y.-J. Zhang, S.-Y. Ding, R. Panneerselvam, and Z.-Q. Tian, "Core–shell nanoparticle-enhanced raman spectroscopy," *Chemical reviews*, vol. 117, no. 7, pp. 5002–5069, 2017.

[19] S. Khatua and M. Orrit, "Probing, sensing, and fluorescence enhancement with single gold nanorods," *The journal of physical chemistry letters*, vol. 5, no. 17, pp. 3000–3006, 2014.

[20] K. Abstiens, D. Fleischmann, M. Gregoritza, and A. M. Goepferich, "Gold-tagged polymeric nanoparticles with spatially controlled composition

for enhanced detectability in biological environments," *ACS Applied Nano Materials*, vol. 2, no. 2, pp. 917–926, 2019.

[21] T. Ishida, T. Murayama, A. Taketoshi, and M. Haruta, "Importance of size and contact structure of gold nanoparticles for the genesis of unique catalytic processes," *Chemical Reviews*, vol. 120, no. 2, pp. 464–525, 2019.

[22] R. de Waele, S. Burgos, H. Atwater, and A. Polman, "Plasmonic metamaterials," in *2009 IEEE LEOS Annual Meeting Conference Proceedings*, pp. 559–560, IEEE, 2009.

[23] J. Aizpurua, P. Hanarp, D. Sutherland, M. Käll, G. W. Bryant, and F. G. De Abajo, "Optical properties of gold nanorings," *Physical review letters*, vol. 90, no. 5, p. 057401, 2003.

[24] P. Capper, *Bulk Crystal Growth of Electronic, Optical and Optoelectronic Materials*, vol. 14. John Wiley & Sons, 2005.

[25] C. Louis and O. Pluchery, *Gold nanoparticles for physics, chemistry and biology*. World Scientific, 2017.

[26] M. Das, K. H. Shim, S. S. A. An, and D. K. Yi, "Review on gold nanoparticles and their applications," *Toxicology and Environmental Health Sciences*, vol. 3, no. 4, pp. 193–205, 2011.

[27] K. Nejati, M. Dadashpour, T. Gharibi, H. Mellatyar, and A. Akbarzadeh, "Biomedical applications of functionalized gold nanoparticles: A review," *Journal of Cluster Science*, pp. 1–16, 2021.

[28] A. Gupta, D. F. Moyano, A. Parnsubsakul, A. Papadopoulos, L.-S. Wang, R. F. Landis, R. Das, and V. M. Rotello, "Ultrastable and biofunctionalizable gold nanoparticles," *ACS applied materials & interfaces*, vol. 8, no. 22, pp. 14096–14101, 2016.

[29] V. Ogarev, V. Rudoi, and O. Dement'eva, "Gold nanoparticles: synthesis, optical properties, and application," *Inorganic Materials: Applied Research*, vol. 9, no. 1, pp. 134–140, 2018.

[30] V. S. Marangoni, J. Cancino-Bernardi, and V. Zucolotto, "Synthesis, physico-chemical properties, and biomedical applications of gold nanorods—a review," *Journal of biomedical nanotechnology*, vol. 12, no. 6, pp. 1136–1158, 2016.

[31] V. Sharma, K. Park, and M. Srinivasarao, "Colloidal dispersion of gold nanorods: Historical background, optical properties, seed-mediated synthesis, shape separation and self-assembly," *Materials Science and Engineering: R: Reports*, vol. 65, no. 1-3, pp. 1–38, 2009.

[32] L. Gou and C. J. Murphy, "Fine-tuning the shape of gold nanorods," *Chemistry of materials*, vol. 17, no. 14, pp. 3668–3672, 2005.

[33] S. Eustis and M. A. El-Sayed, "Why gold nanoparticles are more precious than pretty gold: noble metal surface plasmon resonance and its enhancement of the radiative and nonradiative properties of nanocrystals of different shapes," *Chemical society reviews*, vol. 35, no. 3, pp. 209–217, 2006.

[34] K. A. Willets and R. P. Van Duyne, "Localized surface plasmon resonance spectroscopy and sensing," *Annu. Rev. Phys. Chem.*, vol. 58, pp. 267–297, 2007.

[35] A. Chakraborty, J. C. Boer, C. Selomulya, and M. Plebanski, "Amino acid functionalized inorganic nanoparticles as cutting-edge therapeutic and diagnostic agents," *Bioconjugate chemistry*, vol. 29, no. 3, pp. 657–671, 2017.

[36] L. Freitas de Freitas, G. H. C. Varca, J. G. dos Santos Batista, and A. Benévolo Lugão, "An overview of the synthesis of gold nanoparticles using radiation technologies," *Nanomaterials*, vol. 8, no. 11, p. 939, 2018.

[37] Y. Wang and Y. Xia, "Bottom-up and top-down approaches to the synthesis of monodispersed spherical colloids of low melting-point metals," *Nano letters*, vol. 4, no. 10, pp. 2047–2050, 2004.

[38] J. Kimling, M. Maier, B. Okenve, V. Kotaidis, H. Ballot, and A. Plech, "Turkevich method for gold nanoparticle synthesis revisited," *The Journal of Physical Chemistry B*, vol. 110, no. 32, pp. 15700–15707, 2006.

[39] P. Zhao, N. Li, and D. Astruc, "State of the art in gold nanoparticle synthesis," *Coordination Chemistry Reviews*, vol. 257, no. 3-4, pp. 638–665, 2013.

[40] T. Maruyama, Y. Fujimoto, and T. Maekawa, "Synthesis of gold nanoparticles using various amino acids," *Journal of colloid and interface science*, vol. 447, pp. 254–257, 2015.

[41] A. B. Hughes, *Amino acids, peptides and proteins in organic chemistry, analysis and function of amino acids and peptides*, vol. 5. John Wiley & Sons, 2013.

[42] G. Ghodake, V. S. Vassiliadis, J.-H. Choi, J. Jang, and D. S. Lee, "Facile synthesis of gold nanoparticles by amino acid asparagine: selective sensing of

arsenic," *Journal of nanoscience and nanotechnology*, vol. 15, no. 9, pp. 7235–7239, 2015.

[43] H. Joshi, P. S. Shirude, V. Bansal, K. Ganesh, and M. Sastry, "Isothermal titration calorimetry studies on the binding of amino acids to gold nanoparticles," *The Journal of Physical Chemistry B*, vol. 108, no. 31, pp. 11535–11540, 2004.

[44] E. Csapó, D. Ungor, Z. Kele, P. Baranyai, A. Deák, Á. Juhász, L. Janovák, and I. Dékány, "Influence of ph and aurate/amino acid ratios on the tuneable optical features of gold nanoparticles and nanoclusters," *Colloids and Surfaces A: Physicochemical and Engineering Aspects*, vol. 532, pp. 601–608, 2017.

[45] B. A. CARTER, D. B. Williams, C. B. Carter, and D. B. Williams, *Transmission Electron Microscopy: A Textbook for Materials Science. Diffraction. II*, vol. 2. Springer Science & Business Media, 1996.

[46] G. Dehm, J. M. Howe, and J. Zweck, *In-situ electron microscopy: Applications in physics, chemistry and materials science*. John Wiley & Sons, 2012.

[47] A. Ponce, S. Mejía-Rosales, and M. José-Yacamán, "Scanning transmission electron microscopy methods for the analysis of nanoparticles," in *Nanoparticles in Biology and Medicine*, pp. 453–471, Springer, 2012.

[48] B. M. Tissue, "Ultraviolet and visible absorption spectroscopy," *Characterization of Materials*, pp. 1–13, 2002.

[49] G. Gauglitz and D. S. Moore, *Handbook of spectroscopy*. Wiley-VCH Weinheim, Germany, 2014.

[50] J. Spadavecchia, A. Barras, J. Lyskawa, P. Woisel, W. Laure, C.-M. Pradier, R. Boukherroub, and S. Szunerits, "Approach for plasmonic based dna sensing: amplification of the wavelength shift and simultaneous detection of the plasmon modes of gold nanostructures," *Analytical chemistry*, vol. 85, no. 6, pp. 3288–3296, 2013.

[51] N. R. Tiwari, M. Y. Liu, S. Kulkarni, and Y. Fang, "Study of adsorption behavior of aminothiophenols on gold nanorods using surface-enhanced raman spectroscopy," *Journal of Nanophotonics*, vol. 5, no. 1, p. 053513, 2011.

[52] A. Lübcke, F. Buchner, N. Heine, I. V. Hertel, and T. Schultz, "Time-resolved photoelectron spectroscopy of solvated electrons in aqueous nai solution," *Physical Chemistry Chemical Physics*, vol. 12, no. 43, pp. 14629–14634, 2010.

[53] C. N. Fleming, K. A. Maxwell, J. M. DeSimone, T. J. Meyer, and J. M. Papanikolas, "Ultrafast excited-state energy migration dynamics in an efficient light-harvesting antenna polymer based on ru (ii) and os (ii) polypyridyl complexes," *Journal of the American Chemical Society*, vol. 123, no. 42, pp. 10336–10347, 2001.

[54] E. A. McArthur, A. J. Morris-Cohen, K. E. Knowles, and E. A. Weiss, "Charge carrier resolved relaxation of the first excitonic state in cdse quantum dots probed with near-infrared transient absorption spectroscopy," *The Journal of Physical Chemistry B*, vol. 114, no. 45, pp. 14514–14520, 2010.

[55] J. B. Asbury, E. Hao, Y. Wang, H. N. Ghosh, and T. Lian, "Ultrafast electron transfer dynamics from molecular adsorbates to semiconductor nanocrystalline thin films," 2001.

[56] J. Herbst, K. Heyne, and R. Diller, "Femtosecond infrared spectroscopy of bacteriorhodopsin chromophore isomerization," *Science*, vol. 297, no. 5582, pp. 822–825, 2002.

[57] A. Bhattacherjee, C. D. Pemmaraju, K. Schnorr, A. R. Attar, and S. R. Leone, "Ultrafast intersystem crossing in acetylacetone via femtosecond x-ray transient absorption at the carbon k-edge," *Journal of the American Chemical Society*, vol. 139, no. 46, pp. 16576–16583, 2017.

[58] R. Berera, R. van Grondelle, and J. T. Kennis, "Ultrafast transient absorption spectroscopy: principles and application to photosynthetic systems," *Photosynthesis research*, vol. 101, no. 2-3, pp. 105–118, 2009.

[59] B. M. Ross, S. Tasoglu, and L. P. Lee, "Plasmon resonance differences between the near-and far-field and implications for molecular detection," in *Plasmonics: Metallic Nanostructures and Their Optical Properties VII*, vol. 7394, p. 739422, International Society for Optics and Photonics, 2009. https://www-spiedigitallibrary-org.ejp.mpip-mainz.mpg.de/conference-proceedings-of-spie/7394/739422/Plasmon-resonance-differences-between-the-near--and-far-field/10.1117/12.826804.full.

[60] K. O. Aruda, M. Tagliazucchi, C. M. Sweeney, D. C. Hannah, G. C. Schatz, and E. A. Weiss, "Identification of parameters through which surface chemistry determines the lifetimes of hot electrons in small au nanoparticles," *Proceedings of the National Academy of Sciences*, vol. 110, no. 11, pp. 4212–4217, 2013.

[61] G. V. Hartland, "Optical studies of dynamics in noble metal nanostructures," *Chemical reviews*, vol. 111, no. 6, pp. 3858–3887, 2011.

[62] M. Hu and G. V. Hartland, "Heat dissipation for au particles in aqueous solution: relaxation time versus size," *The Journal of Physical Chemistry B*, vol. 106, no. 28, pp. 7029–7033, 2002. https://pubs-acs-org.ejp.mpip-mainz.mpg.de/doi/abs/10.1021/jp020581+.

[63] Y. S. Ju, "Impact of nonequilibrium between electrons and phonons on heat transfer in metallic nanoparticles suspended in dielectric media," 2005. https://asmedigitalcollection.asme.org/heattransfer/article-abstract/127/12/1400/467425.

[64] N. Ashcroft and N. Mermin, "D.,(1976): Solid state physics," *Saunders College, Philadelphia*.

[65] A. Manjavacas, J. G. Liu, V. Kulkarni, and P. Nordlander, "Plasmon-induced hot carriers in metallic nanoparticles," *ACS nano*, vol. 8, no. 8, pp. 7630–7638, 2014.

[66] C. Clavero, "Plasmon-induced hot-electron generation at nanoparticle/metal-oxide interfaces for photovoltaic and photocatalytic devices," *Nature Photonics*, vol. 8, no. 2, pp. 95–103, 2014. https://www-nature-com.ejp.mpip-mainz.mpg.de/articles/nphoton.2013.238.

[67] E. J. Sie, *Coherent light-matter interactions in monolayer transition-metal dichalcogenides*. Springer, 2017. https://www.springer.com/de/book/9783319695532.

[68] D. A. Long, "Raman spectroscopy," *New York*, vol. 1, 1977.

[69] J. R. Ferraro, *Introductory raman spectroscopy*. Elsevier, 2003.

[70] N. Colthup, *Introduction to infrared and Raman spectroscopy*. Elsevier, 2012.

[71] R. L. McCreery, *Raman spectroscopy for chemical analysis*, vol. 225. John Wiley & Sons, 2005.

[72] Y. Ozaki, C. Huck, S. Tsuchikawa, and S. B. Engelsen, *Near-Infrared Spectroscopy: Theory, Spectral Analysis, Instrumentation, and Applications*. Springer, 2021.

[73] G. Faggio, R. Grillo, and G. Messina, "Raman and micro-raman spectroscopy," *Spectroscopy for Materials Characterization*, pp. 169–200, 2021.

[74] T. Basiev, A. Sobol, P. Zverev, L. Ivleva, V. Osiko, and R. Powell, "Raman spectroscopy of crystals for stimulated raman scattering," *Optical materials*, vol. 11, no. 4, pp. 307–314, 1999.

[75] C. Penney, L. Goldman, and M. Lapp, "Raman scattering cross sections," *Nature Physical Science*, vol. 235, no. 58, pp. 110–112, 1972.

[76] B. B. Johnson and W. L. Peticolas, "The resonant raman effect," *Annual Review of Physical Chemistry*, vol. 27, no. 1, pp. 465–521, 1976.

[77] J. A. Koningstein, *Introduction to the Theory of the Raman Effect*. Springer Science & Business Media, 2012.

[78] D. A. Long, *The Raman effect: a unified treatment of the theory of Raman scattering by molecules*. Wiley, 2002.

[79] G. Wu, *Raman spectroscopy: an intensity approach*. World Scientific, 2016.

[80] A. T. Young, "Rayleigh scattering," *Applied optics*, vol. 20, no. 4, pp. 533–535, 1981.

[81] D. F. Walls, "Quantum theory of the raman effect," *Zeitschrift für Physik A Hadrons and nuclei*, vol. 237, no. 3, pp. 224–233, 1970.

[82] R. Singh, "Cv raman and the discovery of the raman effect," *Physics in Perspective*, vol. 4, no. 4, pp. 399–420, 2002.

[83] S. K. Meena, *Understanding shape control in gold nanoparticles from molecular dynamics simulations*. PhD thesis, Mainz, 2016.

[84] S. K. Meena and M. Sulpizi, "Understanding the microscopic origin of gold nanoparticle anisotropic growth from molecular dynamics simulations," *Langmuir*, vol. 29, no. 48, pp. 14954–14961, 2013.

[85] S. K. Meena, *Understanding shape control in gold nanoparticles from molecular dynamics simulations*. PhD thesis, Universitätsbibliothek Mainz, 2016. https://openscience.ub.uni-mainz.de/handle/20.500.12030/4558.

[86] D. Frenkel, "In understanding molecular simulation, ; frenkel d., smit b., eds," 2002.

[87] L. Verlet, "Computer" experiments" on classical fluids. i. thermodynamical properties of lennard-jones molecules," *Physical review*, vol. 159, no. 1, p. 98, 1967. https://journals.aps.org/pr/abstract/10.1103/PhysRev.159.98.

[88] J. Šponer and N. Špačková, "Molecular dynamics simulations and their application to four-stranded dna," *Methods*, vol. 43, no. 4, pp. 278–290, 2007. https://www.sciencedirect.com/science/article/pii/S1046202307000333.

[89] K. Vanommeslaeghe, E. Hatcher, C. Acharya, S. Kundu, S. Zhong, J. Shim, E. Darian, O. Guvench, P. Lopes, I. Vorobyov, *et al.*, "Charmm general force field: A force field for drug-like molecules compatible with the charmm all-atom additive biological force fields," *Journal of computational chemistry*, vol. 31, no. 4, pp. 671–690, 2010. https://onlinelibrary.wiley.com/doi/abs/10.1002/jcc.21367.

[90] A. Nussbaum, *Applied Group Theory for Chemists, Physicists and Engineers*. Prentice-Hall electrical engineering series, Prentice-Hall, 1971.

[91] J. S. Hub, B. L. De Groot, and D. Van Der Spoel, "g_wham a free weighted histogram analysis implementation including robust error and autocorrelation estimates," *Journal of chemical theory and computation*, vol. 6, no. 12, pp. 3713–3720, 2010.

[92] S. Kumar, J. M. Rosenberg, D. Bouzida, R. H. Swendsen, and P. A. Kollman, "The weighted histogram analysis method for free-energy calculations on biomolecules. i. the method," *Journal of computational chemistry*, vol. 13, no. 8, pp. 1011–1021, 1992.

[93] R. Parthasarathi, V. Subramanian, and N. Sathyamurthy, "Electron density topography, nmr, and nbo analysis of water clusters," *Synthesis and Reactivity in Inorganic, Metal-Organic, and Nano-Metal Chemistry*, vol. 38, no. 1, pp. 18–27, 2008.

[94] E. Engel, "Orbital-dependent functionals for the exchange-correlation energy: A third generation of density functionals," in *A primer in density functional theory*, pp. 56–122, Springer, 2003.

[95] W. Kohn and L. J. Sham, "Self-consistent equations including exchange and correlation effects," *Physical review*, vol. 140, no. 4A, p. A1133, 1965.

[96] K. Mahato, S. Nagpal, M. A. Shah, A. Srivastava, P. K. Maurya, S. Roy, A. Jaiswal, R. Singh, and P. Chandra, "Gold nanoparticle surface engineering strategies and their applications in biomedicine and diagnostics," *3 Biotech*, vol. 9, no. 2, p. 57, 2019.

[97] K. I. Requejo, A. V. Liopo, and E. R. Zubarev, "Gold nanorod synthesis with small thiolated molecules," *Langmuir*, vol. 36, no. 14, pp. 3758–3769, 2020. PMID: 32216357.

[98] C. L. Nehl and J. H. Hafner, "Shape-dependent plasmon resonances of gold nanoparticles," *Journal of Materials Chemistry*, vol. 18, no. 21, pp. 2415–2419, 2008.

[99] C. J. Murphy, T. K. Sau, A. M. Gole, C. J. Orendorff, J. Gao, L. Gou, S. E. Hunyadi, and T. Li, "Anisotropic metal nanoparticles: synthesis, assembly, and optical applications," 2005.

[100] I. P. Lau, H. Chen, J. Wang, H. C. Ong, K. C.-F. Leung, H. P. Ho, and S. K. Kong, "In vitro effect of ctab-and peg-coated gold nanorods on the induction of eryptosis/erythroptosis in human erythrocytes," *Nanotoxicology*, vol. 6, no. 8, pp. 847–856, 2012.

[101] S. Asiya, K. Pal, S. Kralj, G. El-Sayyad, F. de Souza, and T. Narayanan, "Sustainable preparation of gold nanoparticles via green chemistry approach for biogenic applications," *Materials Today Chemistry*, vol. 17, p. 100327, 2020.

[102] I. Chakraborty, N. Feliu, S. Roy, K. Dawson, and W. J. Parak, "Protein-mediated shape control of silver nanoparticles," *Bioconjugate chemistry*, vol. 29, no. 4, pp. 1261–1265, 2018.

[103] L. C. Courrol and R. A. de Matos, "Synthesis of gold nanoparticles using amino acids by light irradiation," *Catalytic Application of Nano-Gold Catalysts; Mishra, NK, Ed.; IntechOpen: London, UK*, pp. 83–99, 2016.

[104] M. E. Hayat, *Basic techniques for transmission electron microscopy*. Elsevier, 2012.

[105] P. Buseck, J. Cowley, and L. Eyring, *High-Resolution Transmission Electron Microscopy: And Associated Techniques*. Oxford University Press, 1989.

[106] C. S. Kumar, *UV-VIS and photoluminescence spectroscopy for nanomaterials characterization*. Springer, 2013.

[107] C. S. Kumar, *Raman spectroscopy for nanomaterials characterization*. Springer Science & Business Media, 2012.

[108] A. H. Pakiari and Z. Jamshidi, "Interaction of amino acids with gold and silver clusters," *The Journal of Physical Chemistry A*, vol. 111, no. 20, pp. 4391–4396, 2007. PMID: 17447742.

[109] G. D. Barmparis, Z. Lodziana, N. Lopez, and I. N. Remediakis, "Nanoparticle shapes by using wulff constructions and first-principles calculations," *Beilstein Journal of Nanotechnology*, vol. 6, pp. 361–368, 2015.

[110] M. H. Abdalmoneam, K. Waters, N. Saikia, and R. Pandey, "Amino-acid-conjugated gold clusters: Interaction of alanine and tryptophan with au8 and au20," *The Journal of Physical Chemistry C*, vol. 121, no. 45, pp. 25585–25593, 2017.

[111] S. K. Meena and M. Sulpizi, "Understanding the microscopic origin of gold nanoparticle anisotropic growth from molecular dynamics simulations," *Langmuir*, vol. 29, no. 48, pp. 14954–14961, 2013. PMID: 24224887.

[112] S. K. Meena and M. Sulpizi, "From gold nanoseeds to nanorods: The microscopic origin of the anisotropic growth," *Angewandte Chemie International Edition*, vol. 55, no. 39, pp. 11960–11964, 2016.

[113] S. K. Meena, S. Celiksoy, P. Schäfer, A. Henkel, C. Sönnichsen, and M. Sulpizi, "The role of halide ions in the anisotropic growth of gold nanoparticles: a microscopic, atomistic perspective," *Phys. Chem. Chem. Phys.*, vol. 18, pp. 13246–13254, 2016.

[114] R. Cortes-Huerto, J. Goniakowski, and C. Noguera, "An efficient many-body potential for the interaction of transition and noble metal nano-objects with an environment," *Journal of Chemical Physics*, vol. 138, p. 244706, JUN 28 2013.

[115] R. Cortes-Huerto, J. Goniakowski, and C. Noguera, "Role of the environment in the stability of anisotropic gold particles," *Physical Chemistry Chemical Physics*, vol. 17, no. 9, pp. 6305–6313, 2015.

[116] Q. Shao and C. K. Hall, "Binding preferences of amino acids for gold nanoparticles: A molecular simulation study," *Langmuir*, vol. 32, no. 31, pp. 7888–7896, 2016. PMID: 27420555.

[117] P. Dobrev, S. P. B. Vemulapalli, N. Nath, C. Griesinger, and H. Grubmüller, "Probing the accuracy of explicit solvent constant ph molecular dynamics simulations for peptides," *Journal of Chemical Theory and Computation*, vol. 16, no. 4, pp. 2561–2569, 2020. PMID: 32192342.

[118] M. Klinger and A. Jäger, "Crystallographic tool box (crystbox): automated tools for transmission electron microscopists and crystallographers," *Journal of applied crystallography*, vol. 48, no. 6, pp. 2012–2018, 2015.

[119] S. Espinoza and J. Stepanek, "Raman study of magnesium induced conversion of polyu-polya duplexes to polyu-polya-polyu triplexes," *Jspec*, vol. 24 (3-4), no. 3-4, pp. 445–448, 2010.

[120] P. Ottova, S. Espinoza, and J. Stepanek, "Magnesium effect on premelting transitions in nucleic acids: Dna duplex and rna hairpin models," *J. Mol. Struct.*, vol. 993 (1-3), no. 1-3, pp. 324–327, 2011.

[121] A. D. MacKerell, D. Bashford, M. Bellott, R. L. Dunbrack, J. D. Evanseck, M. J. Field, S. Fischer, J. Gao, H. Guo, S. Ha, D. Joseph-McCarthy, L. Kuchnir, K. Kuczera, F. T. K. Lau, C. Mattos, S. Michnick, T. Ngo, D. T. Nguyen, B. Prodhom, W. E. Reiher, B. Roux, M. Schlenkrich, J. C. Smith, R. Stote,

J. Straub, M. Watanabe, J. Wiórkiewicz-Kuczera, D. Yin, and M. Karplus, "All-atom empirical potential for molecular modeling and dynamics studies of proteins," *The Journal of Physical Chemistry B*, vol. 102, no. 18, pp. 3586–3616, 1998. PMID: 24889800.

[122] S. Kumar, D. Bouzida, R. H. Swendsen, P. A. Kollman, and J. M. Rosenberg, "The weighted histogram analysis method for free-energy calculations on biomolecules. i. the method," *1011-1021*, vol. 13, no. 8, pp. 845–854, 1992.

[123] B. Hess, C. Kutzner, D. van der Spoel, and E. Lindahl, "GROMACS 4: Algorithms for highly efficient, load-balanced, and scalable molecular simulation," *J. Chem. Theory Comput.*, vol. 4, no. 3, pp. 435–447, 2008.

[124] S. Pronk, S. Pá'll, R. Schulz, P. Larsson, P. Bjelkmar, R. Apostolov, M. R. Shirts, J. C. Smith, P. M. Kasson, D. van der Spoel, B. Hess, and E. Lindahl, "GROMACS 4.5: A high-throughput and highly parallel open source molecular simulation toolkit," *Bioinformatics*, vol. 29, no. 7, pp. 845–854, 2013.

[125] K. Vanommeslaeghe and J. A. D. MacKerell, "Automation of the CHARMM general force field (CGenFF) I: Bond perception and atom typing," *J. Chem. Inf. Model.*, vol. 52, no. 12, p. 3144–3154, 2012.

[126] E. P. R. K. Vanommeslaeghe and J. A. D. MacKerell, "Automation of the CHARMM general force field (CGenFF) II: Assignment of bonded parameters and partial atomic charges," *J. Chem. Inf. Model.*, vol. 52, no. 12, p. 3155–3168, 2012.

[127] I. Geada, H. Ramezani-Dakhel, T. Jamil, M. Sulpizi, and H. Heinz, "Insight into induced charges at metal surfaces and biointerfaces using a polarizable lennard–jones potential," *Nat. Commun.*, vol. 9, p. 716, 2018.

[128] R. A. Dunlap, *Novel Microstructures for Solids*. Morgan & Claypool Publishers Bristol, 2018.

[129] B. Golichenko, V. Naseka, V. Strelchuk, and O. Kolomys, "Raman study of l-asparagine and l-glutamine molecules adsorbed on aluminum films in a wide frequency range," *Semiconductor physics quantum electronics & optoelectronics*, vol. 20, pp. 297–304, 2017.

[130] A. J. D. Moreno, P. T. C. Freire, F. E. A. Melo, J. Mendes Filho, M. A. M. Nogueira, J. M. A. Almeida, M. A. R. Miranda, C. M. R. Remédios, and J. M. Sasaki, "Low-temperature raman spectra of monohydrated l-asparagine crystals," *Journal of Raman Spectroscopy*, vol. 35, no. 3, pp. 236–241, 2004.

[131] J. Casado, J. López Navarrete, and F. Ramirez, "Infrared and raman spectra of l-asparagine and l-asparagine-d5 in the solid state," *Journal of Raman Spectroscopy*, vol. 26, no. 11, pp. 1003–1008, 1995.

[132] P. Dhamelincourt and F. Ramirez, "Polarized micro-raman and ft-ir spectra of l-glutamine," *Applied spectroscopy*, vol. 47, no. 4, pp. 446–451, 1993.

[133] A. Barth, "The infrared absorption of amino acid side chains," *Progress in biophysics and molecular biology*, vol. 74, no. 3-5, pp. 141–173, 2000.

[134] F. Ramirez, I. Tunon, and E. Silla, "Amino acid chemistry in solution: Structural study and vibrational dynamics of glutamine in solution. an ab

initio reaction field model," *The Journal of Physical Chemistry B*, vol. 102, no. 32, pp. 6290–6298, 1998.

[135] G. Wulff *Z. Kristallogr.*, vol. 34, p. 449, 1901.

[136] C. Mottet, G. Tréglia, and B. Legrand, "New magic numbers in metallic clusters: an unexpected metal dependence," *Surface Science*, vol. 383, no. 1, pp. L719–L727, 1997.

[137] L. Vitos, A. Ruban, H. Skriver, and J. Kollár, "The surface energy of metals," *Surface Science*, vol. 411, no. 1, pp. 186–202, 1998.

[138] J. A. Ascencio, M. Pérez, and M. José-Yacamán, "A truncated icosahedral structure observed in gold nanoparticles," *Surface science*, vol. 447, no. 1-3, pp. 73–80, 2000.

[139] C. D. De Souza, B. R. Nogueira, and M. E. C. Rostelato, "Review of the methodologies used in the synthesis gold nanoparticles by chemical reduction," *Journal of Alloys and Compounds*, vol. 798, pp. 714–740, 2019.

[140] E. Petryayeva and U. J. Krull, "Localized surface plasmon resonance: Nanostructures, bioassays and biosensing—a review," *Analytica chimica acta*, vol. 706, no. 1, pp. 8–24, 2011.

[141] J. M. Zook, V. Rastogi, R. I. MacCuspie, A. M. Keene, and J. Fagan, "Measuring agglomerate size distribution and dependence of localized surface plasmon resonance absorbance on gold nanoparticle agglomerate size using analytical ultracentrifugation," *ACS nano*, vol. 5, no. 10, pp. 8070–8079, 2011.

[142] K. M. Mayer and J. H. Hafner, "Localized surface plasmon resonance sensors," *Chemical reviews*, vol. 111, no. 6, pp. 3828–3857, 2011.

[143] G. A. Rance, D. H. Marsh, and A. N. Khlobystov, "Extinction coefficient analysis of small alkanethiolate-stabilised gold nanoparticles," *Chemical Physics Letters*, vol. 460, no. 1-3, pp. 230–236, 2008.

[144] S. K. Ghosh, S. Nath, S. Kundu, K. Esumi, and T. Pal, "Solvent and ligand effects on the localized surface plasmon resonance (lspr) of gold colloids," *The Journal of Physical Chemistry B*, vol. 108, no. 37, pp. 13963–13971, 2004.

[145] W. Haiss, N. T. Thanh, J. Aveyard, and D. G. Fernig, "Determination of size and concentration of gold nanoparticles from uv- vis spectra," *Analytical chemistry*, vol. 79, no. 11, pp. 4215–4221, 2007.

[146] L. Novotny and B. Hecht, *Principles of nano-optics*. Cambridge university press, 2012.

[147] E. E. Bedford, J. Spadavecchia, C.-M. Pradier, and F. X. Gu, "Surface plasmon resonance biosensors incorporating gold nanoparticles," *Macromolecular bioscience*, vol. 12, no. 6, pp. 724–739, 2012.

[148] X. Luo, X. Liu, Y. Pei, Y. Ling, P. Wu, and C. Cai, "Leakage-free polypyrrole–au nanostructures for combined raman detection and photothermal cancer therapy," *Journal of Materials Chemistry B*, vol. 5, no. 39, pp. 7949–7962, 2017.

[149] J. Song, J. Zhou, and H. Duan, "Self-assembled plasmonic vesicles of sers-encoded amphiphilic gold nanoparticles for cancer cell targeting and traceable

intracellular drug delivery," *Journal of the American Chemical Society*, vol. 134, no. 32, pp. 13458–13469, 2012.

[150] A. M. Balachandra, K. Zhu, S. Ramli, P. Soroushian, F. Matalkah, and N. Abdol, "Development of refined chemistries and processing methods for integration of carbon dioxide into a hydraulic binder for effective heavy metal immobilization," *JOJ Material Sci*, vol. 2, pp. 555–593, 2017.

[151] S. A. Maier, *Plasmonics: fundamentals and applications*. Springer Science & Business Media, 2007.

[152] G. V. Hartland, L. V. Besteiro, P. Johns, and A. O. Govorov, "What's so hot about electrons in metal nanoparticles?," *ACS Energy Letters*, vol. 2, no. 7, pp. 1641–1653, 2017.

[153] C. Galloway, P. Etchegoin, and E. Le Ru, "Ultrafast nonradiative decay rates on metallic surfaces by comparing surface-enhanced raman and fluorescence signals of single molecules," *Physical review letters*, vol. 103, no. 6, p. 063003, 2009.

[154] S. Link, C. Burda, M. Mohamed, B. Nikoobakht, and M. El-Sayed, "Femtosecond transient-absorption dynamics of colloidal gold nanorods: Shape independence of the electron-phonon relaxation time," *Physical Review B*, vol. 61, no. 9, p. 6086, 2000.

[155] V. Giannini, A. I. Fernández-Domínguez, S. C. Heck, and S. A. Maier, "Plasmonic nanoantennas: fundamentals and their use in controlling the radiative properties of nanoemitters," *Chemical reviews*, vol. 111, no. 6, pp. 3888–3912, 2011.

[156] N. J. Halas, S. Lal, W.-S. Chang, S. Link, and P. Nordlander, "Plasmons in strongly coupled metallic nanostructures," *Chemical reviews*, vol. 111, no. 6, pp. 3913–3961, 2011.

[157] F. B. Atar, E. Battal, L. E. Aygun, B. Daglar, M. Bayindir, and A. K. Okyay, "Plasmonically enhanced hot electron based photovoltaic device: erratum," *Optics Express*, vol. 21, no. 20, pp. 23324–23324, 2013.

[158] Z. Fang, Y. Wang, Z. Liu, A. Schlather, P. M. Ajayan, F. H. Koppens, P. Nordlander, and N. J. Halas, "Plasmon-induced doping of graphene," *ACS nano*, vol. 6, no. 11, pp. 10222–10228, 2012.

[159] C. Gutiérrez-Wing, J. J. Velázquez-Salazar, and M. José-Yacamán, "Procedures for the synthesis and capping of metal nanoparticles," in *Nanoparticles in Biology and Medicine*, pp. 3–19, Springer, 2012.

[160] H. Kang, J. T. Buchman, R. S. Rodriguez, H. L. Ring, J. He, K. C. Bantz, and C. L. Haynes, "Stabilization of silver and gold nanoparticles: preservation and improvement of plasmonic functionalities," *Chemical reviews*, vol. 119, no. 1, pp. 664–699, 2018.

[161] R. McCaffrey, H. Long, Y. Jin, A. Sanders, W. Park, and W. Zhang, "Template synthesis of gold nanoparticles with an organic molecular cage," *Journal of the American Chemical Society*, vol. 136, no. 5, pp. 1782–1785, 2014.

[162] P. Khullar, V. Singh, A. Mahal, P. N. Dave, S. Thakur, G. Kaur, J. Singh, S. Singh Kamboj, and M. Singh Bakshi, "Bovine serum albumin bioconjugated gold nanoparticles: synthesis, hemolysis, and cytotoxicity toward cancer cell

lines," *The Journal of Physical Chemistry C*, vol. 116, no. 15, pp. 8834–8843, 2012.

[163] G. Zhan, J. Huang, L. Lin, W. Lin, K. Emmanuel, and Q. Li, "Synthesis of gold nanoparticles by cacumen platycladi leaf extract and its simulated solution: toward the plant-mediated biosynthetic mechanism," *Journal of Nanoparticle Research*, vol. 13, no. 10, pp. 4957–4968, 2011.

[164] A. M. Alkilany, P. K. Nagaria, C. R. Hexel, T. J. Shaw, C. J. Murphy, and M. D. Wyatt, "Cellular uptake and cytotoxicity of gold nanorods: molecular origin of cytotoxicity and surface effects," *small*, vol. 5, no. 6, pp. 701–708, 2009.

[165] A. M. Alkilany and C. J. Murphy, "Toxicity and cellular uptake of gold nanoparticles: what we have learned so far?," *Journal of nanoparticle research*, vol. 12, no. 7, pp. 2313–2333, 2010.

[166] J. J. Snellenburg, S. P. Laptenok, R. Seger, K. M. Mullen, and I. H. van Stokkum, "Glotaran: A java-based graphical user interface for the r package timp," 2012.

[167] K. M. Mullen, I. H. Van Stokkum, *et al.*, "Timp: an r package for modeling multi-way spectroscopic measurements," *Journal of Statistical Software*, vol. 18, no. 3, pp. 1–46, 2007.

[168] A. Trügler, *Optical properties of metallic nanoparticles: basic principles and simulation*, vol. 232. Springer, 2016.

[169] M. Perner, P. Bost, U. Lemmer, G. Von Plessen, J. Feldmann, U. Becker, M. Mennig, M. Schmitt, and H. Schmidt, "Optically induced damping of the

surface plasmon resonance in gold colloids," *Physical Review Letters*, vol. 78, no. 11, p. 2192, 1997.

[170] M. Cardona, "Modulation spectroscopy," *Solid State Phys.*, vol. 11, 1969.

[171] T. P. White and K. R. Catchpole, "Plasmon-enhanced internal photoemission for photovoltaics: theoretical efficiency limits," *Applied Physics Letters*, vol. 101, no. 7, p. 073905, 2012.

[172] S. Link, C. Burda, Z. L. Wang, and M. A. El-Sayed, "Electron dynamics in gold and gold–silver alloy nanoparticles: The influence of a nonequilibrium electron distribution and the size dependence of the electron–phonon relaxation," *The Journal of chemical physics*, vol. 111, no. 3, pp. 1255–1264, 1999.

[173] X. Zhang, C. Huang, M. Wang, P. Huang, X. He, and Z. Wei, "Transient localized surface plasmon induced by femtosecond interband excitation in gold nanoparticles," *Scientific reports*, vol. 8, no. 1, pp. 1–7, 2018.

[174] J. Z. Zhang, "Ultrafast studies of electron dynamics in semiconductor and metal colloidal nanoparticles: effects of size and surface," *Accounts of chemical research*, vol. 30, no. 10, pp. 423–429, 1997.

[175] A. M. Brown, R. Sundararaman, P. Narang, A. M. Schwartzberg, W. A. Goddard III, and H. A. Atwater, "Experimental and ab initio ultrafast carrier dynamics in plasmonic nanoparticles," *Physical review letters*, vol. 118, no. 8, p. 087401, 2017.

[176] D. Hoeing, F. Schulz, N. S. Mueller, S. Reich, and H. Lange, "Dark plasmon modes for efficient hot electron generation in multilayers of gold nanoparticles," *The Journal of chemical physics*, vol. 152, no. 6, p. 064710, 2020.

[177] J. H. Hodak, A. Henglein, and G. V. Hartland, "Electron-phonon coupling dynamics in very small (between 2 and 8 nm diameter) au nanoparticles," *The Journal of Chemical Physics*, vol. 112, no. 13, pp. 5942–5947, 2000.

[178] P.-A. Hervieux and J.-Y. Bigot, "Surface plasmon dynamics of simple metal clusters excited with femtosecond optical pulses," *Physical review letters*, vol. 92, no. 19, p. 197402, 2004.

[179] Y. U. Staechelin, D. Hoeing, F. Schulz, and H. Lange, "Size-dependent electron–phonon coupling in monocrystalline gold nanoparticles," *ACS Photonics*, vol. 8, no. 3, pp. 752–757, 2021.

[180] H. Gogoi, B. G. Maddala, F. Ali, and A. Datta, "Role of solvent in electron-phonon relaxation dynamics in core-shell au-sio2 nanoparticles," *ChemPhysChem*, 2021.

[181] P. K. Jain, W. Qian, and M. A. El-Sayed, "Ultrafast cooling of photoexcited electrons in gold nanoparticle- thiolated dna conjugates involves the dissociation of the gold- thiol bond," *Journal of the American Chemical Society*, vol. 128, no. 7, pp. 2426–2433, 2006.

[182] R. Báez-Cruz, L. A. Baptista, S. Ntim, P. Manidurai, S. Espinoza, C. Ramanan, R. Cortes-Huerto, and M. Sulpizi, "Role of ph in the synthesis and growth of gold nanoparticles using l-asparagine: a combined experimental and simulation study," *Journal of Physics: Condensed Matter*, vol. 33, no. 25, p. 254005, 2021.

[183] J. H. Hodak, I. Martini, and G. V. Hartland, "Spectroscopy and dynamics of nanometer-sized noble metal particles," *The Journal of Physical Chemistry B*, vol. 102, no. 36, pp. 6958–6967, 1998.

[184] J. Saavedra, A. Asenjo-Garcia, and F. J. Garcia de Abajo, "Hot-electron dynamics and thermalization in small metallic nanoparticles," *Acs Photonics*, vol. 3, no. 9, pp. 1637–1646, 2016.